Electrical Tuning of Integrated III-V Quantum Dots in Quantum Nano-Photonic Circuits

Dominic Hallett

Submitted for the degree of Doctor of Philosophy

Department of Physics and Astronomy

University of Sheffield

May 2019

Abstract

This thesis describes optical measurements on nanophotonic devices with integrated electrically tuneable quantum dots. The quantum dots enable a range of non-linear behaviour, including single photon generation and the generation of entangled photonic states on-chip. Device behaviour can be controlled by applying electric fields to the devices, enabling fast switching and tuning of device behaviour.

A waveguide-coupled electrically-driven single-photon source is demonstrated. Electroluminescence from a single quantum dot is coupled to a single-mode suspended nanobeam waveguide. The number of quantum dots coupled to the waveguide is limited in order to isolate emission from a single source. The single-photon nature of the emission is confirmed using correlation measurements.

The non-linear behaviour of a quantum dot in a single mode photonic crystal waveguide is investigated. In this work three charge states of the same quantum dot are investigated using resonance fluorescence and resonant waveguide transmission. A strong non-linear effect is generated by the single quantum dot, enabling interactions between pairs of photons and the generation of a two-photon bound state. Fast switching of the device is demonstrated by the application of an electric field.

A waveguide-coupled quantum optical filter is presented. This device utilises Fano interference in a QD-waveguide system to modulate a coherent photonic input, generating a bunched or antibunched output. The photon statistics of the output can be tuned by changing the bias applied to the device.

Acknowledgments

I had the pleasure of undertaking a PhD at the Low Dimensional Structures and Devices group and the University of Sheffield. I would like to thank all the people who work in and around the group. Without their contributions this work would not have been possible.

In particular, I would like to thank my supervisor Luke Wilson and my second supervisor Maurice Skolnick, as well as Andrew Foster and Igor Itskevich, for offering their guidance and knowledge over the last few years.

I would also like to thank other people who have made theoretical, material or practical contributions to the work in this thesis. These include Chris Bentham, David Hurst, Ben Royall, Rikki Coles and Deivis Vaitiekus.

Finally, I thank my family and my friends. In particular my friends Sam, Jack, Ross and Ellie, and Charlotte, who have made these years the best of my life.

Publications

Work in this thesis has appeared previously in the following articles.

- C. Bentham, **D. Hallett**, N. Prtljaga, B. Royall, D. Vaitiekus, R. J. Coles, E. Clarke, A. M. Fox, M. S. Skolnick, I. E. Itskevich and L. R. Wilson, "Single-photon electroluminescence for on-chip quantum networks", Applied Physics Letters **109**, 161101 (2016).

- **D. Hallett**, A. P. Foster, D. L. Hurst, B. Royall, P. Kok, E. Clarke, I. E. Itskevich, A. M. Fox, M. S. Skolnick, and L. R. Wilson, "Electrical control of nonlinear quantum optics in a nano-photonic waveguide". Optica **5**, 5, 644–650 (2018).

- A.P. Foster, **D. Hallett**, I.V. Iorsh, S.J. Sheldon, M.R. Godsland, B. Royall, E. Clarke, I.A. Shelykh, A.M. Fox, M.S. Skolnick, I.E. Itskevich, and L.R. Wilson, "Tunable photon statistics exploiting the Fano effect in a waveguide", Phys. Rev. Lett. **122** 173603 (2019).

CONTENTS

x

1 — INTRODUCTION

1.1 Quantum Information Processing

The field of quantum information processing uses quantum states to enhance the transfer and manipulation of information. It is based on the manipulation of quantum bits, or 'qubits', two-state quantum mechanical systems capable of carrying quantum information. Currently, three main areas of interest in quantum information processing are quantum cryptography [1], quantum metrology [2,3] and quantum computing [4–6].

In quantum computing, qubits are used to perform computation. Qubits allow several improvements on classical computing due to the phenomena of quantum superposition and entanglement [7,8]. Platforms for quantum computation need to meet the DiVinchenzo criteria [9], which outline the necessary requirements on the physical system. It has been shown that quantum computing will allow several classes of problem to be performed exponentially faster [8,10–12], reducing them from non-polynomial to polynomial complexity.

In quantum cryptography, single photons are used to send information between two parties. It relies on the principles of quantum measurement on single particles to detect the presence of eavesdroppers, providing a secure method for sharing information across public channels [1].

In quantum metrology, quantum states are used to improve the sensitivity of measurements of physical parameters [2]. One important example is the use of N00N states to improve the sensitivity of phase measurements in an interferometer [13,14]. One implementation of a quantum computer is based on quantum optical logic gates. These perform quantum operations on photons. A universal basis for quantum com-

putation can be achieved with just two different types of gate [7,15]. One single qubit gate – e.g. a $\pi/2$ phase shift or a Hadamard gate [16] – and one two-qubit gate – e.g. a CNOT [17] or controlled-phase [18–20] gate – is required to create a universal set of logic [7]. Implementation of single qubit gates is possible with linear optics only, and it has been shown that linear optics can be used as a basis for quantum computing [21–24]. However, efficient two-qubit gates require non-linear optical behaviour at the single-photon level [18,25].

1.2 Integrated photonics as a platform for quantum information processing

There are many different systems which can be used as qubits, these include: single electron spins [26], single photons [22,27–31], and anharmonic oscillators - for example atomic energy levels [32] or Josephson junctions [33]. Therefore of great interest is the ability to create single photons [22,34] and isolate single electrons [26] or atoms [32]. In addition, the interactions between these different qubits are powerful tools in quantum information processing.

In this work we investigate the potential of integrated photonics; a platform which offers the possibility of a scalable quantum system with an extremely high component density [27,35,36]. In photonics, photons are used as flying qubits; photons are ideal qubits as they only interact weakly with the environment, isolating them from dephasing effects [36]. Quantum information is encoded into either the path or the polarisation of the photon. Integrated photonics has been used to implement boson sampling [11,37], one implementation of linear optical quantum computing. In integrated photonics the generation and manipulation of single photons can be aided by embedded two-level systems (TLS). A single TLS can act as a source of single-photons [38,39] or as a light-matter interface [40]. In addition, the light-matter interactions of a two-level system can enable strong interactions between photons [41], which do not naturally interact [22]. Currently there are many competing candidate systems, including quantum dots in III-V materials [42,43], colour centres in dia-

mond [44], and trapped ions [32, 45–48] or molecules [49].

We investigate the potential of InAs self-assembled quantum dots in GaAs. QDs are solid-state systems, allowing them to be integrated into photonic structures [42]. Non solid-state systems such as trapped ions require complicated techniques such as optical tweezers [50] to efficiently couple light into the system. QDs have favourable optical properties in comparison to similar solid-state atom systems due to the direct band gap of III-V semiconductors. For example, colour centres in diamond have large phonon sidebands [44], which reduces the coherence of emission from these structures. However there are difficulties in using QDs; the size, and consequently the emission wavelength, of each QD is different, and QD coherence is reduced by interactions with the environment [51, 52]. Despite these difficulties, QDs have shown their potential in recent years as single-photon sources with extremely favourable properties [14, 53], in particular the high collection efficiencies enabled by photonic nanostructures [30].

1.3   Outline of this work

In this work, progress is made towards scalable integrated quantum light sources and photonic logic gates. In chapter 4 an on-chip electrically driven single-photon source is demonstrated; electrical driving and integration of a single-photon source allows scaling to devices which require multiple single-photon sources. In chapter 5 a 1D atom system consisting of a single QD efficiently coupled to a single-mode nanophotonic waveguide is investigated. Electrical tuning and modulation of a single-photon non-linearity is demonstrated, this non-linearity enables light-matter interactions and photon-photon interactions. The non-linearity is stronger than observed in recent work on similar systems; this strong interaction is enabled by the slow light effect of a photonic crystal waveguide. In chapter 6 an integrated quantum optical filter is demonstrated. This filter uses Fano interference in the 1D atom system to modulate a coherent input, producing quantum states of light. The state of the output can be tuned using an electric field, allowing local tuning of the device and tuning of photon statistics without tuning the wavelength of the input/output light.

This page intentionally left blank

2 — Background

This chapter introduces the physical systems studied in this thesis. First the statistical properties of different quantum states of light are introduced. The energy levels, optical properties and coherence properties of quantum dots are discussed. Then field of nanophotonics is introduced and the photonic structures used in this work are described. The chapter ends with brief explanations of the 1D atom model and Fano interference.

2.1 Quantum Photonics

2.1.1 Photon statistics

In quantum photonics, a beam of light is considered as a stream of photons rather than a classical wave [54]. In this section we introduce the statistics of the photon stream. We discuss the different statistical possibilities; and how the photon statistics of a beam are characterised.

Coherent light

The first case to consider is coherent emission. In coherent light there are no time-dependent intensity fluctuations. This case describes most classical light sources, most importantly laser sources. A coherent beam of photons is represented in Figure 2-1a, photons in the stream are randomly distributed. It is important to note that attenuating the source does not change the photon statistics.
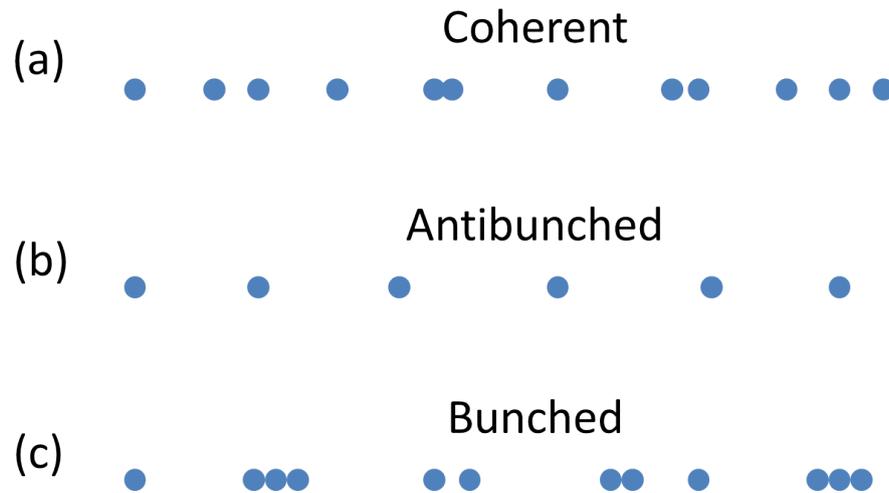
Figure 2-1: Representation of the three types of photon statistics. (a) Coherent light, the photons are randomly distributed in time. (b) Antibunched light, the photons are separated by some minimum time interval. (c) Bunched light, most photons are bunched together in groups.

Antibunched light

Antibunched light is the most commonly considered state in quantum photonics. An antibunched beam of photons is shown in Figure 2-1b. Antibunched light constists of single photons separated by some time interval; the time interval does not need to be regular. Antibunched light is also called single-photon emission. Sources of antibunched emission are generally single light emitting particles, such as individual atoms [55] quantum dots [14, 30, 34, 53, 56–59] or colour centres [44, 60].

Bunched light

The third statistical state is called bunched light. An example of bunched photons is shown in Figure 2-1c. In bunched emission, photons are more likely to be in groups than isolated. Sources of bunched light include 'chaotic' light sources (i.e. classical light sources in which light intensity fluctuates over time) and quantum optical filters [61–68]. In quantum optical filters, single photons are removed from a coherent stream to create a bunched output.

6

2.1.2 Measurement of photon statistics

In order to analyse the photon statistics of a stream of light, the second order correlation function needs to be introduced. The second-order correlation is defined by:

$$g^{(2)}(\tau) = \frac{\langle n_1(t)n_2(t+\tau)\rangle}{\langle n_1(t)\rangle\langle n_2(t+\tau)\rangle}, \qquad (2.1)$$

where $n_i(t)$ is the number of counts registered on detector i at time t. The angled brackets $\langle...\rangle$ represent integrals over a large range of t. An important case of this equation is $g^{(2)}(0)$, which describes the probability of two-photons arriving at the detector at the same time, compared to two-photons arriving separated by a large time difference.

For coherent light, there is no time correlation in the intensity. Photons are separated by random time intervals, therefore the probability of two-photons being detected at the same time is equal to the probability of two-photons being separated by a large time; $g^{(2)}(\tau) = 1$. In antibunched light photons are separated by some minimum time difference, therefore the probability of detecting two photons at the same time is low; $g^{(2)}(\tau) < 1$. In bunched light photons are grouped together, therefore photons are more likely to arrive at the same time; $g^{(2)}(\tau) > 1$.

2.2 III-V Quantum Dots

The quantum emitters studied in this thesis are InAs/GaAs self-assembled quantum dots (QDs). These nanostructures are small islands of strained InAs in a bulk GaAs matrix [69,70]. The difference in band gap of InAs and GaAs creates a 3-D potential well, confining charge carriers within the QD. This nanometer-scale 3-D confinement of carriers leads to discrete quantised energy levels within the QD [71]. As a result, the energy levels of a single QD form an anharmonic oscillator, and can be used as a two-level system (TLS) [42]. QDs are powerful elements in quantum photonics, acting as high-quality single-photon sources [29,30,56,57] and optical non-linearities [35,43].

2.2.1   Energy levels

The three-dimensional confinement of carriers in QDs creates discrete energy levels. These energy levels are analogous to atomic energy levels. In this work we consider only the lowest energy levels, the s-shell for electrons in the conduction band and heavy-holes in the valence band. Higher energy states are not considered as the available thermal energy, $k_B T$, is much smaller than the energy of the intraband transitions. When excited, carriers in these states quickly relax to the lowest available energy state by the emission of phonons. These higher energy states include the $d-$ and $f-$shell energy levels, and the light-hole energy levels. The lowest energy levels are isolated from these higher transitions, allowing the QD to be considered as a much simpler system of few energy levels.

Each lowest energy level can contain up to two electrons or holes. Due to the Coulomb interaction electrons and holes in the QD form excitonic states. There is a ladder of exciton states available from the ground state (0) to the biexciton ($2X$) state. The simplest exciton which is formed is the neutral exciton (X_0), consisting of one electron (e^-) and one hole (h^+). The electron has an s-type wavefunction, with total angular momentum $J_{e,z} = \pm 1/2$; the heavy hole has a p-type wavefunction, with total angular momentum $J_{h,z} = \pm 3/2$ [72]. The neutral exciton exhibits four spin states, which are superpositions of the individual e^- and h^+ spin states. The four energy states are:

$$X_B = \frac{1}{\sqrt{2}}(|\Uparrow\downarrow\rangle + |\Downarrow\uparrow\rangle) \tag{2.2a}$$

$$Y_B = \frac{1}{\sqrt{2}}(|\Uparrow\downarrow\rangle - |\Downarrow\uparrow\rangle) \tag{2.2b}$$

$$X_D = \frac{1}{\sqrt{2}}(|\Uparrow\uparrow\rangle + |\Downarrow\downarrow\rangle) \tag{2.2c}$$

$$Y_D = \frac{1}{\sqrt{2}}(|\Uparrow\uparrow\rangle - |\Downarrow\downarrow\rangle) \tag{2.2d}$$

The X_B and Y_B states have a total angular momentum $m_j = \pm 1$, these are known as bright states because the exciton can relax from these states to the ground state by emitting a photon. The X_D and Y_D states have total angular momentum $m_j = \pm 2$, they are known as dark states because the transition to the ground state is optically

forbidden due to the difference in angular momentum [73].

In the absence of a magnetic field or spin interaction these four states would be degenerate. The degeneracy of the bright and dark states is lifted by the short range electron-hole spin interaction. If the QD is asymmetric, the degeneracy of the bright exciton states (X_B and Y_B) is lifted, this is known as fine structure splitting [72]. The X_B and Y_B states emit linearly polarised photons with orthogonal polarisations.

In addition to the neutral exciton to ground state transition ($X_0 \rightarrow 0$), there are three other radiative exciton transitions of interest. These are the positive exciton ($X^+ \rightarrow h^+$), negative exciton ($X^- \rightarrow e^-$) and biexciton ($2X \rightarrow X_0$) transitions. None of these excitons have non-degenerate spin states unless under a magnetic field [74,75]. The four exciton transitions have different transition energies due to the Coulomb interaction between the charge carriers. The charge state of the exciton is determined by the charge environment around the QD. In diode structures the charge state can be controlled [76,77] by controlling the tunnelling rates of carriers into and out of the QDs.

2.2.2 Quantum confined Stark effect

The emission energy of light from a QD transition depends on the energy difference between the electron and hole states. Applying an electric field to the QD modifies the shape of the conduction and valence bands. The effect of an electric field applied in the growth direction is shown in Figure 2-2; the electron and hole wavefunctions are shifted by the electric field to lower energy states. This results in a reduction in the energy difference of the electron and hole states, and a subsequent redshift in the light created by this transition. This field dependence of the emission energy is called the Quantum Confined Stark Effect (QCSE).

The energy shift as a function of electric field is given by Equation 2.3.

$$\Delta E(F) = pF + \beta F^2, \tag{2.3}$$

where p is the electric dipole moment of the QD, and β is the polarisability.

The QCSE can be used to fine tune the photon energy in quantum optical exper-
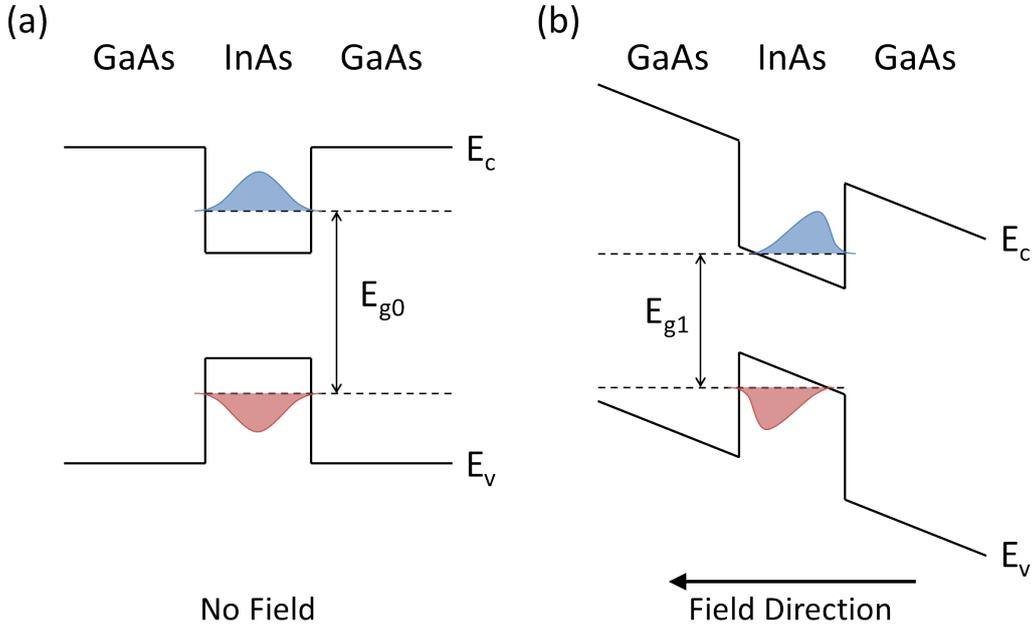
Figure 2-2: Effect of an external electric field in the z-direction on QD transition energy. (a) The band structure and transition energy of an exciton in a quantum dot under no electric field (i.e. flat band conditions). (b) The band structure of the same quantum dot under an electric field. The electron and hole wavefunctions are shifted by the electric field. This redshifts the transition energy of the exciton due to the quantum-confined Stark effect.

iments, or to adjust the detuning of a QD transition relative to the energy of an incoming photon. The electric field is a particularly powerful control mechanism in nanophotonics as it can be used to address individual QDs [78], and it allows fast modulation of the QD energy [79].

At large electric fields, the electron and hole will tunnel out of the QD. This limits the tuning range which can be achieved using the QCSE. The maximum tuning range is determined by the potential barrier between the QDs and the doped layers. The effective barrier height can be increased by using QDs with lower energy states, or by surrounding the QDs with a large band-gap material, for example AlGaAs.

For the QDs studied in this thesis - InAs QDs in bulk GaAs emitting at 900 nm - the maximum tuning range is ~0.15 meV. When a larger field is applied carriers tunnel out of the QD and emission is quenched. Tuning ranges of 4 meV have been observed in InAs QDs emitting at 1.5 μm [80], and tuning ranges of 25 meV have been achieved in QDs emitting at 900 nm by using large AlGaAs barriers [81].

2.2.3   Coherence in Quantum Dots

The energy distribution of photons emitted by a TLS depends on the coherence time of the emitter. This distribution is a Lorentzian line, with a full-width half-maximum defined by Equation 2.4 [82]

$$FWHM = \frac{h}{\pi \cdot T_2},$$ (2.4)

where T_2 is the coherence time.

In the ideal case, the coherence of light emitted from a TLS transition is determined by the lifetime of the emitter (with $T_2 = 2T_1$). In this case the emission line from the TLS transition has an energy distribution known as the radiative linewidth. It is important for many quantum photonics applications for the emission linewidth to be at the radiative limit. However, there are several mechanisms which affect the coherence of the emission. In the following section we consider the dephasing mechanisms relevant to this work, pure dephasing and spectral wandering, and the associated coherence of resonance fluorescence from a QD.

2.2.3.1   Pure dephasing

Pure dephasing is a term encompassing a range of dephasing mechanisms, most notably acoustic phonon interactions [83–85], which reduce the coherence of the excitonic state. Pure dephasing effects have no effect on the exciton population in the QD. The coherence time of emission including pure dephasing effects is given by Equation 2.5 [42].

$$\frac{1}{T_2} = \frac{1}{2T_1} + \frac{1}{T_2^*},$$ (2.5)

where T_2 is the coherence time of the emitted light, T_1 is the lifetime of the QD and T_2^* is the pure dephasing time.

2.2.3.2 Spectral wandering

QDs also experience spectral wandering, a dephasing process arising from interactions with the local charge environment. Fluctuations in the charge environment around the QD cause the QD energy to fluctuate over time due to the QCSE. These fluctuations in QD energy reduce the coherence of single-photon emission from the QD. The radiative linewidth can be recovered by measuring the QD on a very short timescale [34], or by using resonant excitation [86]. When exciting resonantly a photon is only absorbed when the QD is resonant with the laser. This property is favourable when measuring resonant emission, however it has a deleterious effect when measuring resonant absorption. This has a severe effect on the measurements in chapter 5, which require a deterministic interaction with the QD.

It is important in many areas of QD research to minimise the effects of spectral wandering. This is done by limiting the number of charge traps in the GaAs crystal and by keeping the charge traps saturated with carriers. Spectral wandering can also be mitigated by reducing the QD lifetime; this makes the radiative linewidth of the QD broader and the effect of spectral wandering less significant [43]. It has been shown that charge traps are particularly prevalent at dry-etched surfaces, therefore thin membrane structures can cause additional spectral wandering [51]. The effect of surfaces can be mitigated using a $p-i-n$ diode to control the electric field across the QD, screening the QD from the field caused by surface charge fluctuations [77]. The charge traps are kept full by limiting the available escape mechanisms of carriers in the charge traps, by working at low temperature [87] and using low power laser excitation [52]. Typically the random fluctuations of charge environment change the shape of the emission line from Lorentzian to Gaussian. However if the charge states are saturated the wandering can be in the 'motional narrowing regime' in which a Lorentzian broadening is observed [88].

2.2.3.3 Resonance Fluorescence

When a QD transition is excited resonantly, there are two contributions to the coherence of the output [89]. These are resonant Rayleigh scattering (RRS) and resonant photoluminescence (RPL). The output signal is a superposition of these two contributions. The RRS component inherits the coherence of the excitation laser; the RPL has coherence determined by the coherence time of the QD, T_2, and the excitation power used. The relative intensity of the two components in the low power limit is determined by Equation 2.6 [89], it depends on the lifetime, T_1, and coherence time, T_2, of the QD,

$$\frac{I_{RRS}}{I_{Total}} = \frac{T_2}{2T_1},\tag{2.6}$$

where I_{RRS} is the intensity of resonant Rayleigh scattering from the QD and I_{Total} is the total intensity scattered from the QD.

2.3 Integrated Nano-photonics

In order to couple light efficiently to quantum dots, they are embedded in nano-photonic devices. The small scale of the devices enables high coupling efficiencies between embedded emitters and the photonic devices [35]. III-V semiconductors leverage the direct band gap of the material to create efficient light-matter interfaces. The high refractive index of GaAs minimises optical loss between devices.

Nano photonic devices have been developed that function effectively as important photonic components. These include single-photon sources [90, 91], cavities [29, 92], beam splitters [93–96], phase shifters [95, 96, 96], on-chip single-photon detectors [97] and spectral filters [98, 99]. These different devices can be connected together on-chip using optical waveguides [42]. Integrated nano-photonics offers a scalable approach to quantum photonics, as multiple devices can be connected together on a single chip with minimal losses. This method creates a photonic chip with a high component density [42].

2.3.1 Nanophotonic Devices

2.3.1.1 Nanobeam Waveguides

Critical to nano-photonics is the ability to confine light in nano-photonic structures and to guide light around a circuit. This can be achieved using an air-clad suspended nanobeam waveguide, which confines light in two directions by total internal reflection, leaving one allowed propagation direction. This nanobeam is a horizontal GaAs nanowire; the surrounding material has been etched away. SEM images of typical suspended nanobeams used in this work are shown in Figure 2-3.

The dimensions of the nanobeam are carefully chosen to allow only a single TE mode to propagate. The cross-sections of these nanobeams are 280x170 nm^2. The high refractive index of GaAs in comparison to air allows efficient confinement of the mode, minimising waveguide loss. In Figure 2-3 roughness can be seen on top of the nanostructure; this is material that has deposited on the surface which is removed in a subsequent cleaning step.

2.3.1.2 Photonic crystal waveguides

Another method of controlling the propagation of light is to use a photonic crystal. Photonic crystals are periodic structures, alternating between two materials of different refractive index. A photonic band gap is created by this periodic structure, analogous to the electronic band gap created by the periodic lattice of a semiconductor. Light in this band gap cannot propagate through the photonic crystal. The distance between holes in the photonic crystal determines the energy of the band gap, related by the equation $a = \lambda/2n$, where a is the lattice period of the photonic crystal. In this work we use we use photonic crystal devices with a period of roughly 250 nm, these photonic crystals block the propagation of light in the range 900-950 nm. By removing the holes in one row of the photonic crystal, as shown in Figure 2-4, we can create a path along which light can propagate.

The photonic crystals used in this work are 2D triangular photonic crystals. They consist of an array of air holes in a GaAs slab. The photonic crystal confines light

14
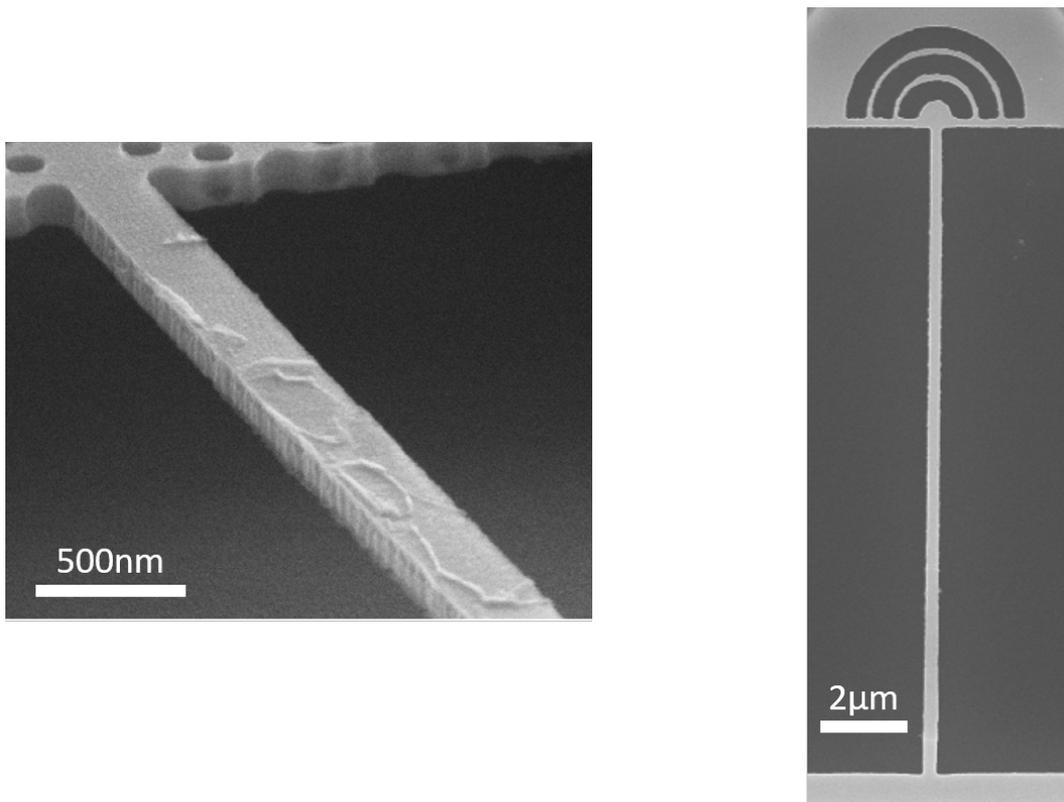
Figure 2-3: Nanobeam waveguides. (a) Angled SEM image of a free-standing nanobeam waveguide, the top surface and side wall of the beam are visible. (b) Top-down SEM image of a nanobeam waveguide; the top end is terminated by a Bragg grating outcoupler, the bottom end is connected to a GaAs slab.

in the plane of the slab. Light is confined vertically by total internal reflection, as in the nanobeam.

Photonic crystal devices are created by introducing defects into a photonic crystal. In the photonic crystal devices studied in this work, the defects are a row of missing holes in the lattice; a structure known as a W1 waveguide. SEM images of a PhC waveguide device are shown in Figure 2-4. In this device a single 'gap-guided' mode allows light to propagate along the row of defects. The group velocity of this guided mode is highly frequency dependent; it is reduced at frequencies close to the band edge [100–102]. This is called the slow light effect; the reduction in group velocity increases the interaction strength of QDs coupling to this mode [102], enabling high coupling efficiencies [103, 104] and increasing the radiative decay rate of the QD [43, 100, 101]. This increase is described by the Purcell factor (F_P) [100], given

by

$$F_P(r) = \frac{3\pi c^3 a |\mathbf{e}_k(r) \cdot \hat{\mathbf{n}}|^2}{\omega^2 \sqrt{\epsilon} v_g} \qquad (2.7)$$

where ω is the angular frequency of the QD, v_g is the group velocity of the propagating mode, ϵ is the dielectric constant of the waveguide, a is the period of the photonic crystal, $\mathbf{e}_k(r)$ is the electric field of the propagating mode at the position of the QD, and $\hat{\mathbf{n}}$ is the unit vector along the orientation of the dipole of the QD transition.
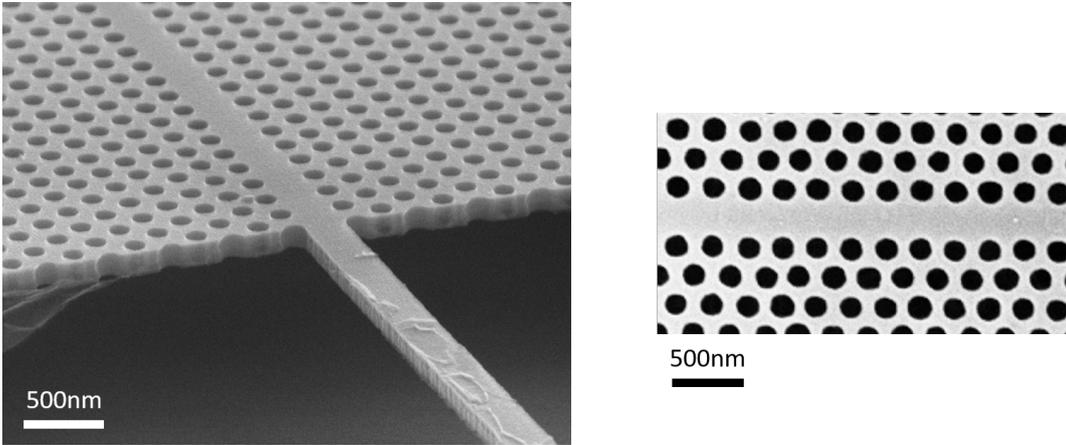
Figure 2-4: W1 Photonic Crystal waveguides. (a) Angled SEM image of a W1 photonic crystal (PhC) waveguide connected to a suspended nanobeam. The PhC region is a suspended slab with a lattice of holes etched through it. (b) Top-down SEM image of the W1 waveguide; one row of holes has been removed from the photonic crystal design to create the waveguide.

2.3.1.3 Grating couplers

One important goal of integrated quantum photonics is to be able to detect single-photons on chip. For measuring single components and devices however, it is more practical to detect the light off chip. This is achieved by scattering light vertically using Bragg gratings; the light can then be collected by confocal microscope.

Bragg grating outcouplers (BGOs) are used in this thesis to terminate nanobeam waveguides, scattering incident light out of plane [105]. Each grating consists of three semi-circular lines around the end of the nanobeam. The grating period is chosen to be $\lambda/2n$, which maximises out of plane scattering and minimises reflections. An SEM image of a typical grating coupler used in this work is shown in Figure 2-5

The light scattered out of plane is collected into a single-mode fibre. It is predicted that collection efficiencies as high as 40% [104] can be achieved using this design, however in practical devices lower coupling efficiencies are measured [106]. These circular gratings also have strong back-reflections [104,107]. Recently, improved coupling efficiency and reduced reflectivity has been achieved using shallow etched gratings [106].
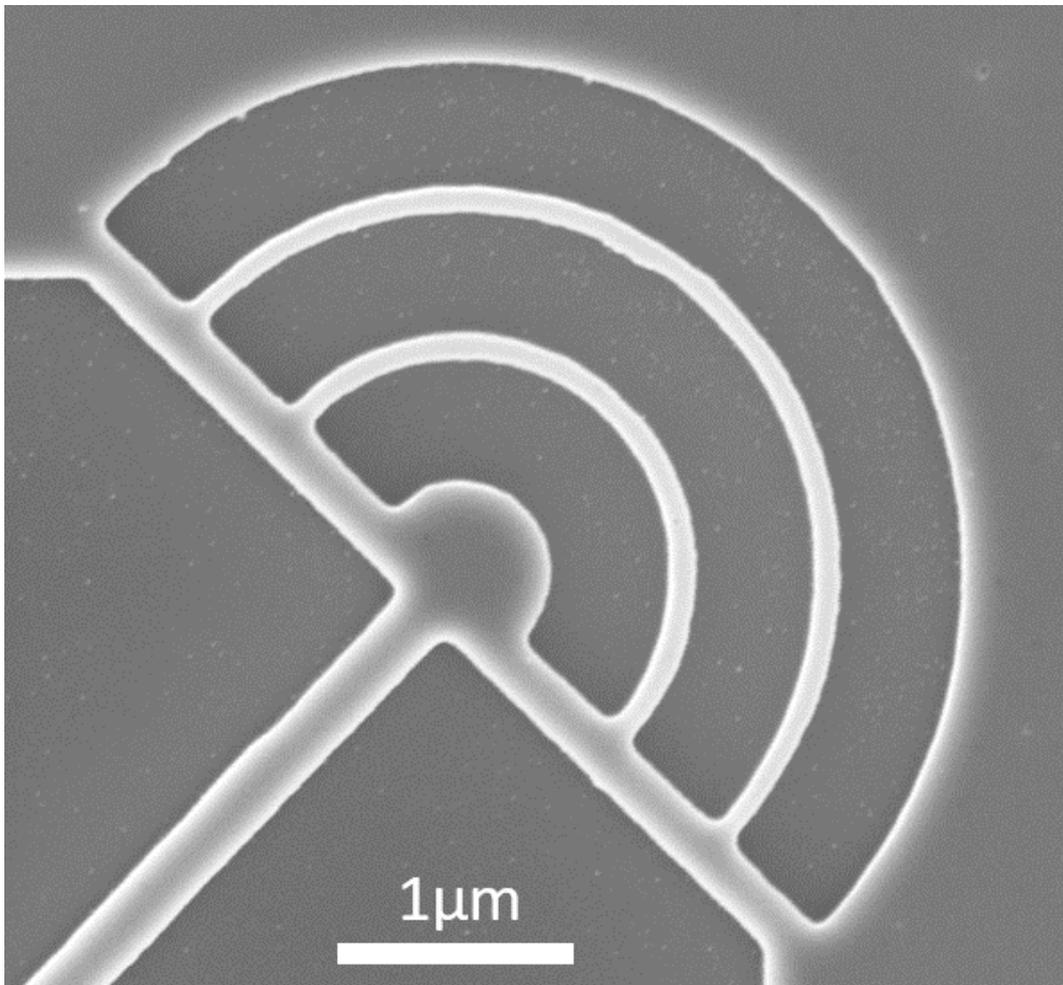

Figure 2-5: Top-down SEM image of a BGO coupled to a nanobeam waveguide. The bright areas are GaAs, the darker sections have been etched away. The repeating pattern of the structure scatters incoming light at an angle of ~90°, scattering of light out of the plane of the device. BGOs allow efficient injection and collection of light into and out of photonic devices.

2.3.2 Coupling efficiency

One of the major benefits of III-V nanophotonics is the high coupling efficiencies that are achievable between QDs and devices. High coupling efficiencies enable efficient collection of single photons [29, 29, 30], and near deterministic light-matter interfaces [108, 109]. The high coupling efficiencies are enabled by the small scale of the devices, which result in high electric field densities, and the direct band gap of III-V materials, which results in a high QD radiative emission rate. As a result, a QD positioned at the field maxima of a single mode device will couple very efficiently to that mode. The coupling efficiency is characterised by the β factor, which gives the probability for an exciton in the QD to recombine by emitting a photon into a particular waveguide mode. The β factor also describes the probability of a photon in the waveguide mode to excite the QD. The β factor is defined as:

$$\beta = \frac{\Gamma_{wg}}{\Gamma_{wg} + \Gamma_{rad} + \Gamma_{nr}}, \tag{2.8}$$

where Γ_{wg} is the coupling rate into the desired waveguide mode, Γ_{rad} is the decay rate into other optical modes and Γ_{wg} is the non-radiative decay rate of the QD. Coupling efficiencies as high as 98.4% have been measured in photonic crystal waveguide devices [104].

Photonic devices can be designed which support circularly polarised modes [110–112]. In this case it is possible to design a unidirectional waveguide, in which light from a QD transition will only couple to one propagating mode in the waveguide [86, 107, 110]. This has been used to couple the QD spin state to the photon emission path [107], enabling a method of initialising a single QD spin state [77, 113].

2.3.2.1 The Purcell effect

The emission rate of the QD can be enhanced or supressed by its photonic environment [114–116]. Enhancing the emission rate of a QD is extremely desirable, increasing the coupling efficiency of the device [100] and enabling higher repetition rates in single-

photon sources [31]. In addition, the effects of pure dephasing and spectral wandering of the QD are mitigated, improving the indistinguishability of emitted photons [31] and the strength of non-linearities [43]. The magnitude of enhancement is given by the Purcell factor:

$$F_P = \frac{\Gamma_D}{\Gamma_{FS}} \tag{2.9}$$

where Γ_D is the decay rate of the QD in the photonic device and Γ_{FS} is the decay rate of the QD in free space.

In this work, Purcell enhancements arise from the slow-light effect of a photonic crystal waveguide [100–102]. Purcell factors as large as 30 have been predicted for quantum dots in photonic crystal waveguides [100].

2.4   1D atom model

The potential of quantum dots in nanophotonic structures can be realised in the model of a 1D atom. In the model an 'atom' - modelled as a two-level system - is coupled to a single propagating optical mode, creating an interface between the TLS and photons in the mode [40, 43]. The coupling efficiency of the TLS to the mode is characterised by the beta factor, β. In the ideal case decay to other modes is suppressed, and the coupling efficiency is between the TLS and the mode is 100% ($\beta = 1$). When this condition is met, all photons that scatter from the atom couple to the optical mode and all photons in the mode will interact with the TLS; the system is a deterministic light-matter interface.

The 1D atom enables several opportunities for quantum information processing. The 1D atom is nonlinear at the single photon level, where the response of the system is different for inputs of one-photon and two-photon states. This non-linearity can be used to enable two-qubit logic gates [46] and single-photon transistors [25], or to generate entangled photon states [38, 41, 43, 117]. The deterministic light-matter interface also enables the transfer of information between static and flying qubits [108, 118] and

deterministic single-photon sources [38].

A number of different systems have been proposed as 1D atom systems. These include QDs [43], diamond colour centres [119], or N-V centres [44], in nanophotonic structures; atoms in cavities [32, 46–48]; and surface plasmons [25].

Mathematical description of the 1D atom model

Here we examine the 1D atom model for the case of a single QD in a single mode waveguide. A diagram of the system is shown in Figure 2-6. The important parameters in this model are the coupling efficiency, β, and the detuning between the laser and the QD, δ. The intensities of single and two-photon transmission and reflection are calculated, from which the transmitted intensity and the autocorrelation function of the transmitted field is calculated.

The system is modelled using the input-output formalism similar to that presented
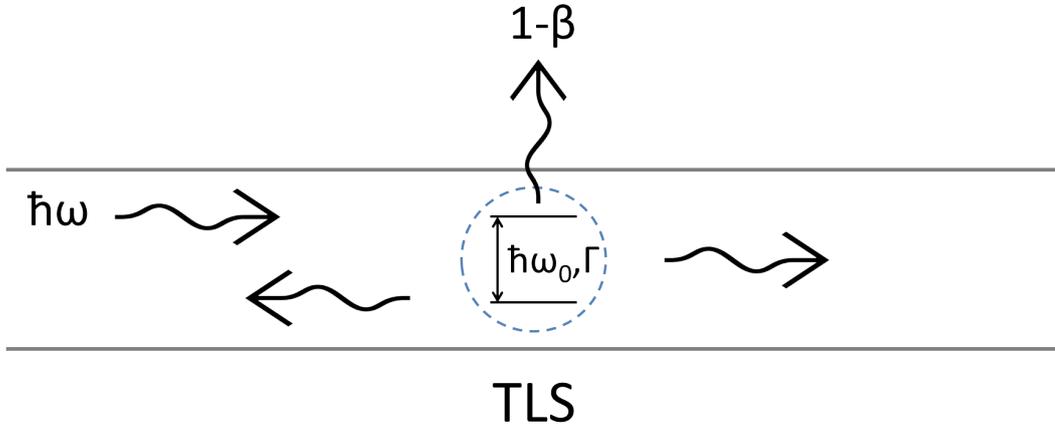
Figure 2-6: Diagram of the 1D atom model. Incoming light of energy $\hbar\omega$ scatters off a QD with a transition energy of $\hbar\omega_0$ and decay rate Γ. The TLS is coupled to the waveguide with coupling efficiency β.

in Xu et al. [120]. In this model, a single QD is coupled to a waveguide which supports modes propagating forwards and backwards. The two modes of the waveguide are treated as individual channels. The QD can be excited exactly once by an input state.

Using this model, the transmission of single photons is given by Equation 2.10.

$$T_1(\omega) = |t_1(\omega)|^2 = \left| 1 - \frac{\beta}{1 - i(\omega - \omega_0/\Gamma)} \right|^2, \tag{2.10}$$

Where β is the waveguide coupling efficiency, ω is the input photon frequency, ω_0 is the QD transition frequency and Γ is the radiative decay rate of the QD. t_1 is the transmission amplitude of the system, where the transmitted intensity $T_1(\omega) = |t_1(\omega)|^2$.

From this point on, the detuning of the QD and the laser is represented by the dimensionless parameter δ.

$$\delta = \frac{\omega - \omega_0}{\Gamma}, \tag{2.11}$$

The transmission of single photons is shown in Figure 2-7. It can clearly be seen that
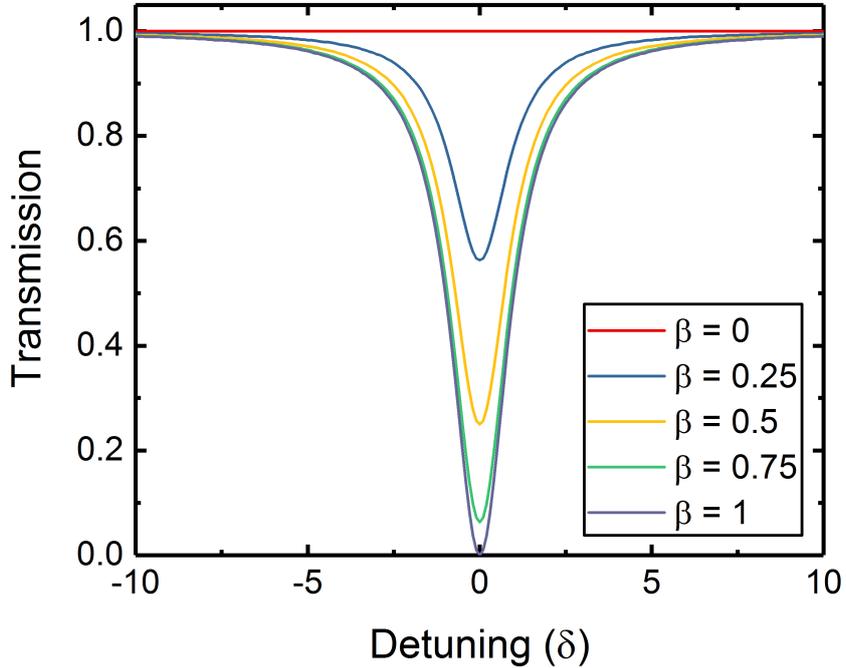
Figure 2-7: Transmission against detuning for different coupling efficiencies. A dip in transmission is seen when the incoming light and the QD are resonant. The minimum of the transmission dip depends on the coupling efficiency.

if the TLS is resonant with the laser then the TLS blocks the transmission of single photons through the waveguide. In the ideal case, $\beta = 1$, the waveguide transmission

is reduced to 0. For non-unity coupling efficiencies the minimum transmission is given by $(1 - \beta)^2$.

The second order autocorrelation function of the transmitted light is readily calculated from the atomic operators. In the limit $\tau = 0$ (zero time difference between the two photons) the autocorrelation function is given by Equation 2.12.

$$G^{(2)}(\tau = 0, \delta) = \left| t_1(\delta)^2 - \frac{\beta^2}{(1 + \delta^2)} \right|^2, \tag{2.12}$$

The normalised autocorrelation function, $g^{(2)}(0, \delta)$, is achieved by normalising the autocorrelation function to the square of the single-photon transmission intensity from Equation 2.10 ($|t_1(\omega)|^4$).

$$g^{(2)}(0, \delta) = \frac{1}{|t_1(\delta)|^4} \left| t_1(\delta)^2 - \frac{\beta^2}{(1 + \delta^2)} \right|^2, \tag{2.13}$$

This equation has two contributing terms. The first, $t_1(\delta)^2$, is the two-photon plane wave state. This state describes two photons interacting with the TLS separately, hence it is the square of the single photon transmission. This state always produces a coherent output, $g^{(2)}(0) = 1$. The other term describes the two-photon bound state, in which two input photons interact with the TLS together. This term produces quantum correlations in the transmitted light. In the ideal case, the two photon bound state is preferentially transmitted, resulting in bunching of the output field.

2.5 Fano interference

In experimental realisations of the 1D atom models, several effects can complicate the picture [43]. Of particular relevance to this work is Fano interference. Fano interference is a general wave phenomenon which occurs when a resonant scattering process interferes with a background continuum [121]. The resonance was first investigated by Ugo Fano in 1961 [122]. Many examples of Fano resonances can be found in different areas of physics. In our case light interacts resonantly with the QD transition, and this interferes with the continuous background arising from the waveguide modes.

The details of this interference are discussed further in chapter 5 and form the basis of the work in chapter 6. Here we will describe the phenomenon in general.

The absorption spectrum of a Fano resonance is given in Equation 2.14 [121].

$$\sigma(E) = D^2 \frac{(q + \Omega)^2}{(1 + \Omega^2)}, \tag{2.14}$$

where $q = \cot\Delta$ is the Fano parameter, which describes the asymmetry of the line. Δ is the phase shift of the continuum. $\Omega = (E - E_0)/\Gamma$ is the normalised detuning of the resonant emitter and the incoming light. $D^2 = 4\sin^2\Delta$ is a normalisation constant. In the limiting cases of this equation, $q = 0, q \to \pm\infty$ ($\Delta = \pi/2, \Delta = 0, \pi, 2\pi$ etc.) the absorption spectrum is Lorentzian. These limiting cases are cases where the input is completely coupled to either the resonant emitter or the continuum; as a result there is no Fano interference.

At other values of q the resonance has a characteristic asymmetric lineshape [121]. The different absorption lineshapes that can be produced by Fano interference are demonstrated in Figure 2-8, which plots Equation 2.14 for different parameters.

For values of $\Delta = \pi/4$ and $\Delta = 3\pi/4$ the spectrum transitions from minimum to maximum absorption over a very small change in energy. This sharp transition is caused by the phase shift of the resonant interaction, which varies dependent on the detuning between incoming light and the resonance. This causes destructive and constructive interference at the minimum and maximum respectively. The sharp transition between minimum and maximum can be utilised to make a fast optical switch [121].

Fano resonance is often seen in QD systems [61, 123, 124]. In these cases the QD is the resonant emitter, the background continuum is either a continuum of electron states [124] or an optical mode [61, 123].
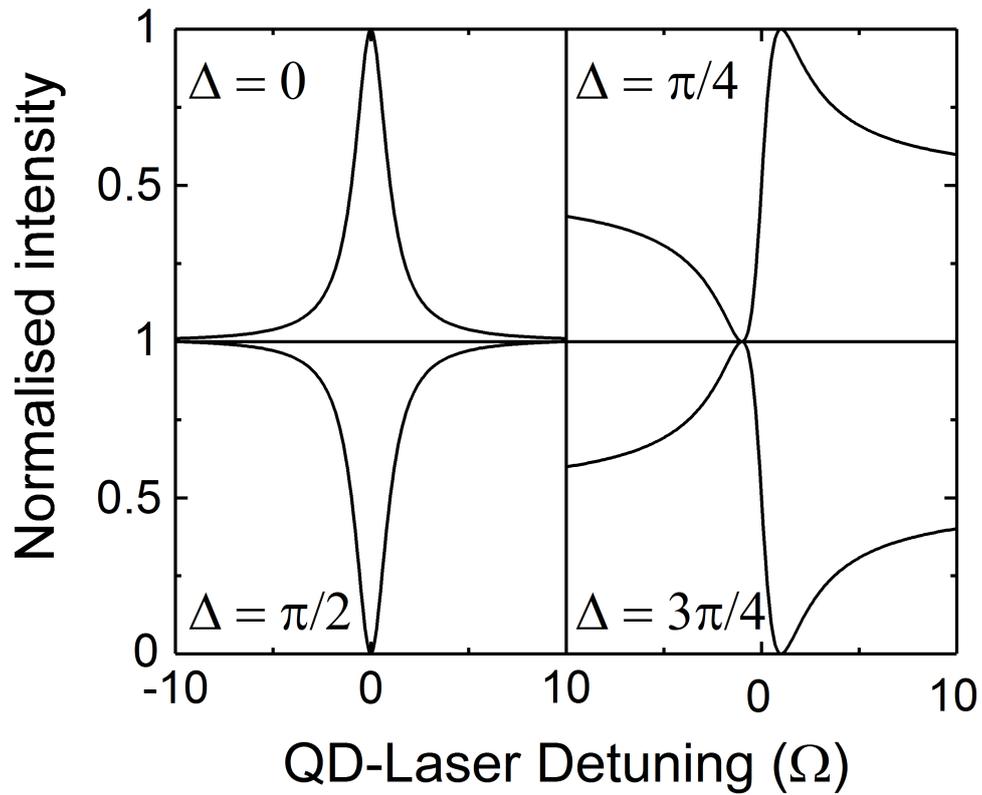
Figure 2-8: Absorption sectra in systems showing Fano interference for different values of Δ. At values of $\Delta = 0, \pi, 2\pi$ etc. the absorption spectrum shows a Lorentzian peak. At $\Delta = \pi/2$, the absorption spectrum is a Lorentzian dip. In both these cases there is no coupling between the QD and the continuum. At intermediate values of Δ the characteristic asymmetric lineshape of a Fano resonance can be seen.

3 — METHODS

This chapter discusses the experimental methods used for this work. First, the methods used to grow high-quality QDs and fabricate nano-photonic devices are introduced. Then the computational methods used to design and analyse the devices are presented. Subsequently, the microscopy methods, experimental measurement techniques, and cryogenic techniques used to characterise the devices are discussed.

3.1 Sample Growth, Fabrication and Characterisation

The following section introduces fabrication techniques used to produce the devices that are studied in this thesis. This includes a discussion of the QD growth techniques used to create high-quality wafer material and the lithographic techniques used to fabricate the nano-photonic devices. In addition, the extra fabrication steps required to allow electrical contact to the devices are discussed.

3.1.1 Quantum Dot Growth

The QDs used in this work are Indium Arsenide (InAs) self-assembled QDs grown in Gallium Arsenide (GaAs) using molecular beam epitaxy (MBE). Self-assembled QDs are grown via the Stranski-Krastnow growth method [70, 125]. This is a powerful growth method as the full wafer including the QDs can be grown in a single MBE session. In this method the QDs are created by the lattice mismatch (approximately 7%) of InAs and GaAs. A low density (~ 10 QDs/μ m^2) distribution of QDs can be consistently grown using this method [126].

A thin layer of InAs is deposited on the GaAs substrate. The lattice mismatch of the two materials causes strain in the InAs layer. After a critical thickness of ~1.6 monolayers, this stress is relieved by the formation of 3D islands. The InAs deposition is then stopped, leaving a random distribution of islands (the QDs) on top of a thin layer of strained InAs (the wetting layer). The formation of the QDs can be monitored using reflection high-energy electron diffraction (RHEED). RHEED is used to analyse the topology of the crystal surface [127,128]; which assists in reliably stopping Indium deposition at the correct time, allowing control of the size and density of the QDs. An Indium flush technique [129,130] can then be used to adjust the size, and consequently the transition energies, of the QDs. For this technique the QDs are partially capped with GaAs, and then an annealing step is used to remove the exposed InAs, truncating the QDs. After this step the QDs are fully capped with GaAs and the rest of the wafer is grown.

The QD materials studied in this work were grown by Edmund Clarke at the EPSRC National Epitaxy Facility at the University of Sheffield.

3.1.2 Heterostructures

One of the major benefits of QDs is that they are embedded in a semiconductor matrix, allowing the fabrication of photonic devices with QDs embedded inside. For fabrication, the QDs need to be grown inside specific membrane heterostructures. All the photonic devices in this thesis are air-clad. This requires a thin waveguide layer, with a sacrificial layer beneath that can be removed. In order to achieve this, a 1 μm layer of $Al_{0.6}Ga_{0.4}As$ is first grown on the substrate. This AlGaAs layer can be selectively removed using hydrofluoric acid (HF), a process which does not affect the GaAs membrane. On top of this layer 85 nm of GaAs is grown, then a single InAs QD layer, then another 85 nm of GaAs. This forms a 170 nm thick GaAs membrane with a layer of randomly distributed QDs at the centre. The thickness of the membrane is chosen to enable the fabrication of single-mode waveguides.

For electrical control a vertical $p-i-n$ diode is defined in the 170 nm waveguide membrane. For this structure the bottom 30 nm of the waveguide is (Silicon) $n-$doped, and the top 30nm of the waveguide is (Beryllium) $p-$doped. The doping

concentration is ypically 10^{18}cm^{-2} for n-doped material and 10^{19}cm^{-2} for p-doped material. An electric field is applied across this diode through contacts attached to the $p-$doped and $n-$doped layers, as shown in Figure 3-2. More complicated diode structures can be grown to adjust the electrical response of the QDs, incorporating more doped layers [77] or AlGaAs tunnelling barriers [81].
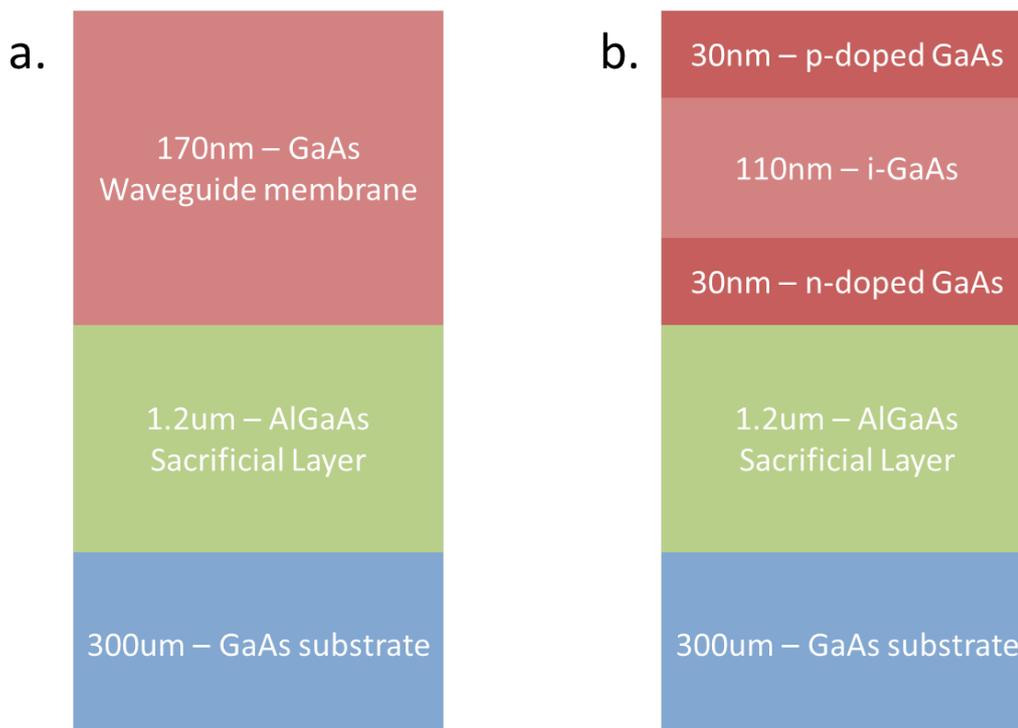
Figure 3-1: Wafer heterostructures for (a) An undoped waveguide membrane sample and (b) a $p-i-n$ waveguide membrane sample. In both cases the QD layer is grown in the centre (85 nm from the surface) of the GaAs membrane. The sacrificial layer can be removed to create a suspended device of 170 nm depth

3.1.3   Diode Fabrication

In order to apply a voltage to the sample, diode mesas need to be defined. This requires metal contacts to be attached to the top $p-$doped layer and bottom $n-$doped layer of the membrane. A layer of photosensitive resist (SPR350) is spin coated onto the wafer. Then a mask is aligned over the wafer and the resist is exposed to UV emission, defining the mesa pattern into the resist. The resist is then developed in MF26a, this removes all areas of resist that have been exposed to the UV emission. The mesa pattern is then etched into the sample. The etch is controlled so as to

expose the $n-$layer of the wafer for contacting (140-170 nm depth).

After the mesa structure has been defined, metal (TiAu) contacts are deposited onto the surface. For this the same resist coating, exposure and developement method is used, and then metal is deposited onto the exposed areas of the wafer only. A Titanium/Gold alloy is used for the contacts to reduce diffusion of gold into the doped layers. The chip is then mounted to a chip-carrier. Finally, a gold wire ball bonder is used to connect the metal contacts on the chip to the metal pins of the chip carrier. A schematic of a suspended device in a diode mesa is shown in Figure 3-2.
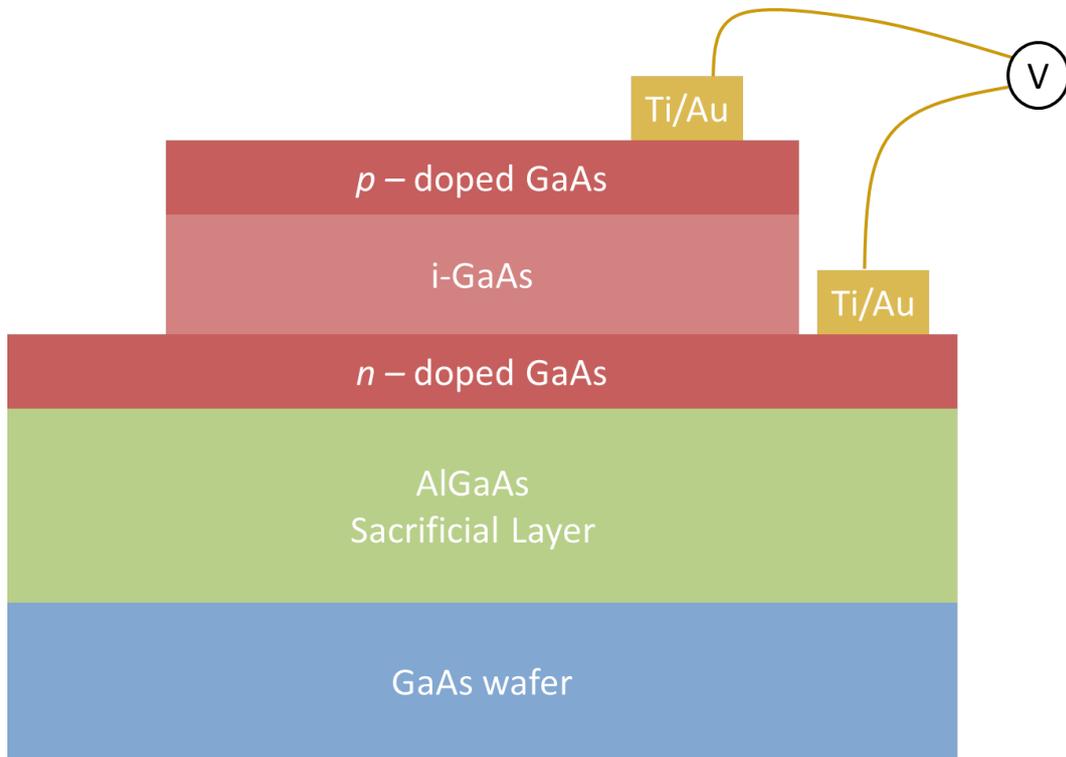
Figure 3-2: Visualisation of an etched diode mesa allowing electrical connections to be made to the $p-$ and $n-$ doped layers. Applying a voltage between these two layers allows a vertical electric field to be applied to the QDs in the mesa region

3.1.4 Structure Fabrication

After diode mesas have been fabricated, nanophotonic devices are made using similar a lithographic method. In this method the 2D pattern of the device, designed using CAD software, is etched into the wafer; the material under the device is then removed to create a free-standing air-clad device. The steps required in this process

are outlined here, diagrams of the different steps are provided in Figure 3-3.

The wafer is first spin coated with an electron sensitive resist (ZEP520A), this covers the full wafer with a material that will resist etching. A pattern of the devices is then produced in the resist using scanning electron beam lithography (EBL). The areas of the resist exposed to the electron beam become soluble in xylene. This lithography method allows a minimum feature size of ~ 20 nm. The resist is then developed in xylene, removing the exposed resist to create a mask for the etching step. The pattern can now be etched into the wafer, using either a dry (Inductively-coupled plasma) or wet (chemical) etch. For photonic structures this step needs to etch through the GaAs membrane, exposing the AlGaAs layer for the underetching step. A shallow etch $(40 - 50$ nm$)$ can also be performed, breaking the top $p-$ doped layer of the device to electrically isolate some areas of the device. The remaining resist is then removed. For devices on which electrical isolation is required multiple fabrication steps are performed; one for the deep etch (to define the devices) and one for the shallow etch (to enable electrical isolation).

To create suspended structures, the devices are then under-etched. This is performed with hydrofluoric acid (HF), which attacks the AlGaAs sacrificial layer but not the GaAs waveguide membrane. The HF is then removed from the sample using critical point drying, if the critical drying step is not used then the surface tension of the acid with cause the device to collapse as it dries. The full process produces free-standing air-clad devices containing embedded QDs at their centre.

The structures studied in this thesis were fabricated by Dr Ben Royall.

3.1.5 Scanning Electron Microscopy

The finished structures are checked using a scanning electron microscope (SEM). This allows precise imaging of the structure, with a resolution of <10 nm. This imaging allows us to confirm that the devices have been successfully fabricated. SEM imaging also allows precise measurement of feature sizes for comparison of the experimental and theoretical device performance.
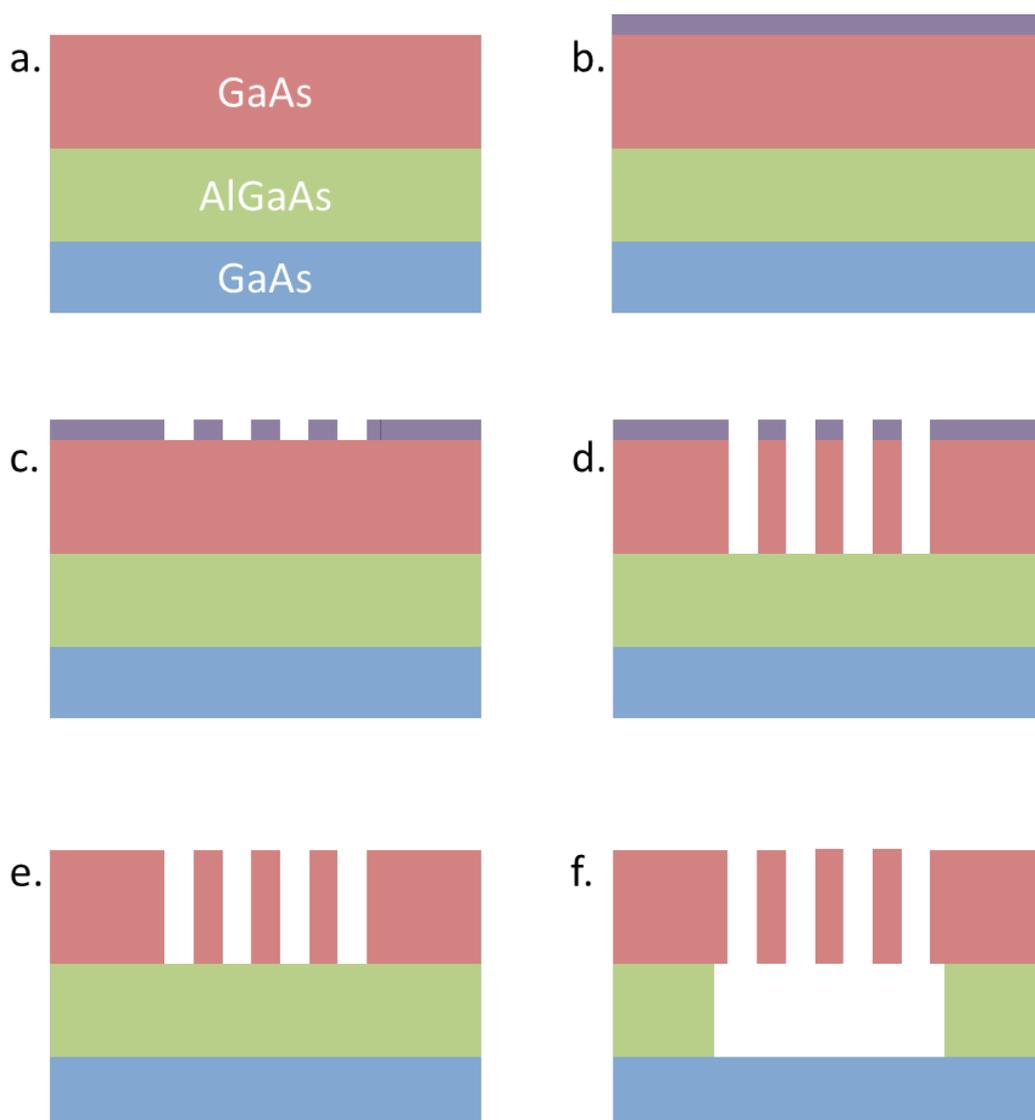
Figure 3-3: The sample at different steps in the etching process. The steps are labelled (a)-(f). (a) The wafer before processing as in 3-1 (not to scale). (b) The wafer is covered with an electron sensitive resist. (c) The device is patterned into the resist using EBL and the resist is developed to create a mask of the device. (d) The shape of the device is etched into the GaAs membrane. (e) The remaining resist is removed. (f) The device is underetched to leave a free-standing device.

3.2 FDTD Simulation

The operation of photonic devices can be studied using computational simulations. This is useful for designing and understanding device operation. Simulations performed for this work use the finite-difference time-domain (FDTD) method for a variety of applications.

The method simulates the propagation of electromagnetic fields through an arbitrary dielectric material using Maxwell's equations. A dipole source or mode source is used as the input. The structure is broken down into a three-dimensional mesh. Then the electric and magnetic fields at each point in the mesh are used to calculate the change in field over a finite time step. A large number of time steps are performed until the simulation reaches some endpoint, defined either by a maximum time limit or a minimum remaining energy in the device. The electric and magnetic fields at any location in the simulation can be monitored, allowing analysis of the photonic properties of the device.

FDTD simulations are used in chapter 4 to calculate the position dependence of the electric field in the device. This is used to estimate the coupling efficiency of QDs at different positions in the device. In chapter 5, simulations are used to model the transmission band gap of a photonic crystal waveguide. This information is used to optimise fabrication parameters for the devices. Simulations are also used to model reflections from different interfaces in the devices.

All FDTD simulations in this work were performed using Lumerical FDTD solutions [131]. The FDTD simulations in chapter 4 were performed by Dr Rikki Coles, the FDTD simulations for the devices used in chapter 5 and chapter 6 I performed myself.

3.3 Cryogenics

All experiments in this thesis are performed at 4.2 K to eliminate the dephasing effects of phonon absorption [87]. To achieve this, samples are placed in liquid helium cooled cryostats. Two types of cryostat were used in this work.

In the continuous flow cryostat liquid helium is continually passed through the cryostat. The helium cools a cold finger, which provides thermal contact to the sample. The sample itself is kept under vacuum. A glass window allows optical access to the sample. The position of the sample is adjusted by moving the whole cryostat relative to the objective lens. This is achieved by mounting the cryostat on translation stages. Fine adjustments to alignment are made by adjusting the confocal optics above the

cryostat.

The continuous flow cryostat is used to rapidly characterise samples, it allows for the quick replacement of samples. However the flow of helium introduces vibrations, which limit the stability of the cryostat. Therefore this cryostat is not suitable for measurements where precise alignment needs to be maintained for a long time.

Some measurements in this work require long integration times. For these measurements, the sample is placed in a helium bath cryostat. The sample is placed in a vacuum tube; this tube is immersed in liquid helium. Thermal contact between the helium and the sample is provided by a low density (50 mbar) of helium gas in the sample tube.

Optical access is provided by a window at the top of the sample tube. The position of the sample is controlled by piezoelectric translation stages. Three stages allow full XYZ movement of the sample relative to the fixed aspheric (NA: 0.55) objective lens.

3.4 Microscopy and Analysis

The photonic devices are studied using confocal microscopy to focus light from above the sample onto a small area on the sample surface. This technique enables optical excitation of specific QDs, the injection of light into a waveguide and the collection of light emitted from a QD or scattered by an outcoupler. The following section discusses the microscopy methods, QD excitation schemes and the spectral analysis techniques used in this thesis.

3.4.1 Confocal Microscopy

Samples are probed using confocal microscopy. This technique allows light to be focused onto, and collected from, specific positions on the sample surface. A diagram of the confocal microscope used in this thesis is shown in Figure 3-4.

A confocal microscope differs from a conventional microscope in that a pinhole is used to limit the image to a small spot on the surface of the sample. In our case the pinhole is defined by the core of a single mode fibre (radius = 4.4 μm). This creates a diffraction limited (radius = $\sim$ 0.5 μm) spot on the sample. If a laser is injected

from the fibre, the light will reach this position on the sample only. If emission from the sample is collected into the fibre, then it is emission from this spot only that is collected.

The confocal technique can be used to excite and collect emission from single QDs [74,75,132]. Multiple spots can be defined by using multiple pinholes, and the position of each spot can be adjusted independently by changing the angles of mirrors between each pinhole and the objective lens. A charge-coupled device (CCD) camera allows conventional optical microscope imaging of large areas of the sample for alignment purposes.

All measurements in this thesis are made from directly above the sample surface, measuring light that is scattered vertically out of the wafer.
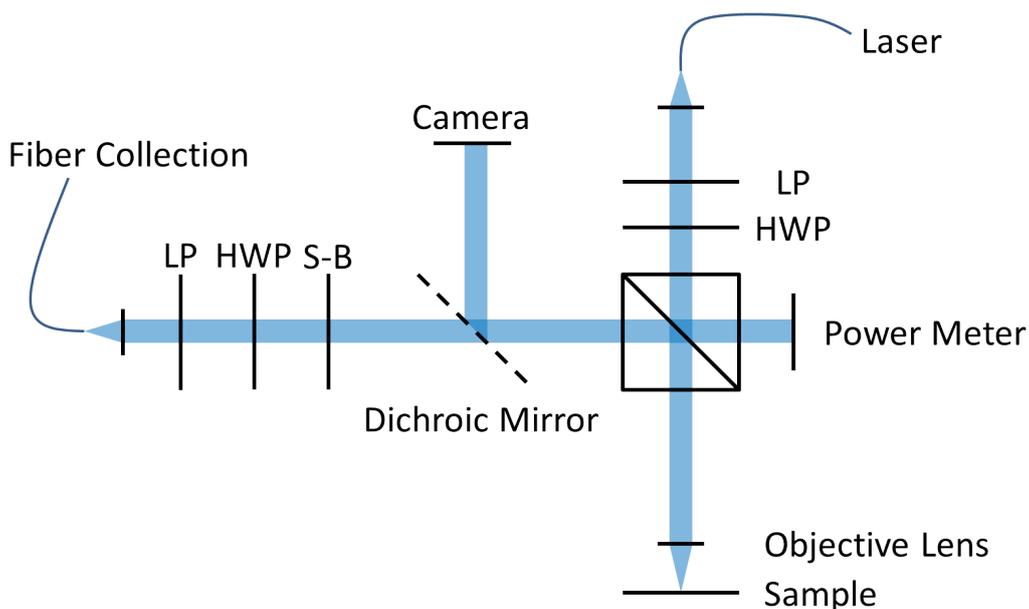
Figure 3-4: Diagram of the confocal microscope setup used for EL, PL and RF measurements. Two fibre-coupled optical paths allow excitation and measurement of the sample via a 50:50 beam splitter. A power meter monitors the laser power incident on the beam splitter. Short wavelength light is reflected by a dichroic mirror to a camera to aid with alignment. Linear polarisers (LP), half-wave plates (HWP) and a Soleil-Babinet (SB) compensator are used in RF measurements to reject laser scatter off the sample.

3.4.2 Non-resonant Excitation of Single QDs

QDs in the devices are excited using either optical or electrical excitation. Emission from optically excited QDs is called photoluminescence (PL), emission from electrically excited QDs is called electroluminescence (EL). In optical excitation, an incident photon creates a free electron in the conduction band and a hole in the valence band; this electron and hole relax into the QD. Electrical excitation is achieved by applying a bias to the $p - i - n$ diode such that electrons and holes tunnel from the $p-$ and $n-$ layers into the QDs.

Confocal microscopy enables measurement of small numbers of QDs using either PL or EL. In PL measurements, two confocal spots are focused onto the sample, one to excite the QDs and one to collect the emission. When measuring PL small numbers of QDs are excited [69, 74, 75]. Optical excitation in this work is performed using either a 632.8 nm HeNe laser or an 808 nm diode laser.

In EL measurements, only the collection spot is required. When measuring EL all QDs which have a bias applied to them will emit, therefore electrical excitation excites a large number of QDs in the sample. Measurements on EL from single QDs have been achieved by limiting the collection area using confocal microscopy [78]. Limiting the number of QDs excited using electrical excitation is a major challenge in the work presented in chapter 4.

3.4.3 Resonance Fluorescence of Single QDs

One specific type of optical excitation is resonance fluorescence (RF). In RF measurements, a QD single transition is excited directly by photon with energy matching the transition energy. As such, only one QD is excited in RF measurements. Measuring RF using a confocal microscopy setup presents several experimental challenges. RF is also useful as an analysis technique.

When using resonant excitation it is important to differentiate between emission from the QD and scattered laser light from the sample. In non-resonant optical excitation the excitation laser is removed using spectral filtering. In resonant excitation the excitation laser is of the same wavelength as the QD emission so this is not an option.

Two techniques are used to differentiate between RF emission and laser scatter. The first is polarisation rejection. In this technique, the excitation and collection paths are orthogonally linearly polarised, such that scattered laser light is rejected while RF emission from the QD is collected. Half-wave plates, quarter-wave plates and Soleil-Babinet compensators are added to the microscopy setup to improve the rejection of the laser while maintaining a high QD signal. The positions of the polarising optics are indicated in Figure 3-4.

The second technique used in resonant excitation is modulation. This allows the laser background to be measured and removed from the final signal. Modulation can be performed by tuning the QD or laser energy out of resonance, or by modulating an above band laser which stabilises the charge state of the QD [86, 133].

RF can be used to take a high resolution spectrum of a single QD transition. In this measurement the excitation laser is tuned through resonance with the QD transition, the RF intensity is measured at different values of detuning. By measuring the detuning dependence of the RF intensity, the inhomogeneous linewidth (broadened by spectral diffusion) and lineshape of the QD transition is measured.

In RF measurements the emission intensity is measured using avalanche photodiodes (APDs). APDs count the number of photons emitted from the QD, however they do not provide any spectral information about the light. This is not important in RF measurements as only one QD is excited and the emission energy is indentical to the excitation laser energy. In other measurements, spectral analysis of the emitted light is required to isolate emission from single QDs.

3.4.4   Spectroscopy

Spectral analysis of QD emission is performed using a grating spectrometer. This instrument separates of light of different energies. This is achieved by spatially separating the light using a diffraction grating, then focusing the light onto a charge-coupled device (CCD) image sensor. The spatial measurement of the CCD is then converted to a spectral measurement using known parameters of the spectrometer and grating. The spectrometer used in this work is a Princeton Instruments Acton

SpectraPro SP750i, the CCD is a Princeton Instruments Pylon CCD. The maximum achievable resolution with this spectrometer is 16 μeV. This technique is used to characterise QDs, allowing measurement of their central energies, emission intensities and linewidths.

The spatially separated light can also be directed through a narrow aperture, exiting the spectrometer. By doing this the spectrometer can be used as a tuneable spectral filter. This is used to isolate emission from a single QD line for further study; removing emission from other sources on the sample such as the wetting layer and other QDs. When used as a filter the spectrometer has a maximum resolution of $\sim$50 μeV.

3.4.5 Interferometry

The coherence of emitted light can be measured directly using interferometry. Two types of interferometer are used in this work: a scanning Fabry-Pérot interferometer and a Michelson interferometer. The Fabry-Pérot interferometer is used to measure EL linewidths which are narrower than the resolution limit of the spectrometer. The Michelson interferometer is used to measure RF coherence in the absence of spectral wandering.

The scanning Fabry-Pérot interferometer is a cavity that has a narrow transmission linewidth. The central frequency of the transmission can be tuned by applying a voltage to a piezoelectric crystal which controls the cavity length. By tuning the central frequency a spectrum of the input light can be produced. The Fabry-Pérot interferometer can achieve a resolution of 0.3 μeV. A Michelson interferometer allows measurement of coherence in the time domain. This is used to determine the coherence time of RF emission from the QD. The RF emission is difficult to measure in the spectral domain because a proportion of the light is coherent scatter, which has the coherence of the laser. In the spectral domain this produces a bright resolution limited line whereas in time domain this produces a flat baseline which is easier to remove.

The Michelson interferometer splits input light into two arms using a beam splitter. The two paths are then interfered with each other. One path has a controllable path length. Fine tuning of the path difference produces interference fringes due to the

phase difference of each path. Coarse tuning of the path difference changes the visibility of the fringes. This change in visibility is used to measure the coherence time of the input light. The interferometer used in this work has a maximum path difference of 30 cm, corresponding to a maximum time difference of 1 ns.

3.5   Time Resolved Single-Photon Counting

Spectroscopy measurements extract useful information for characterising QD transitions. However spectroscopy alone does not allow characterisation of the quantum optical properties of the devices. In order to observe these effects, time-resolved single-photon counting (TRSPC) measurements need to be undertaken. TRSPC can be used to measure the time response of a light source, or to measure the photon statistics of a light source.

In any TRSPC measurement, the arrival time of a single-photon detection event is compared to a reference pulse. This reference pulse can be a laser pulse, or a different single-photon detection event. A histogram of time differences between the two pulses is created.

TRSPC measurements require a method of detecting single-photons, and a method of comparing arrival times with a resolution of a few picoseconds. The measurement hardware used in TRSPC measurements will be briefly discussed. Then the specific TRSPC measurements used in this work are discussed.

3.5.1   Single-Photon Detectors

When performing quantum optical measurements, single-photon detectors are used. There are two types of single-photon detector used in this thesis: avalanche photodiodes (APDs) and superconducting nanowires (SNSPDs).

An APD consists of a photoelectric material operating in a large reverse bias. The large reverse bias is used to apply a gain to the photocurrent created by a single-photon. The result of this is that a single-photon incident on the detector creates a measurable pulse. The response time of the APDs used in this work is roughly 400 ps.

Superconducting nanowire single-photon detectors (SNSPDs) are the second type of time resolved single-photon detectors used in this work. In an SNSPD the photon is absorbed by a superconducting nanowire. The local heating caused by the absorption of the photon raises the temperature above the critical temperature, meaning that some part of the nanowire is no longer superconductive. The increase in resistance this causes produces a voltage pulse which can be measured. The response time of an SNSPD can be as low as 15 ps, with efficiencies of up to 85% [134].

SNSPDs have a much shorter time response than APDs; however SNSPDs need to operate at a temperature below 3K, whereas APDs function at room temperature. As a result the SNSPDs need to be cooled in a separate cryostat. Because of this additional experimental requirement, SNSPDs are only used when APDs are unsuitable, for example if the QD lifetime is shorter than the APD response time. In this work they are used when studying Purcell-enhanced QDs [92] only.

3.5.2 Single-Photon Counting

A single-photon correlator (SPC) is used to correlate the signal and reference. This module is able to measure the relative arrival time of the two voltage pulses with picosecond resolution [135]. The module used in this work is a Becker-Hickl SPC-130. This card uses the reference pulse as a start signal, triggering a rising voltage. The second pulse is used to stop the rising voltage. This voltage is measured, giving a measurement of the time difference between the two pulses. The time difference of each event is added to a histogram, which builds up over many photon detection events to represent some time-dependent parameter of the emission.

3.5.3 Photon correlation measurements

TRSPC is used for three types of measurement in this work; measurements of QD lifetime, QD autocorrelation measurements and QD cross-correlation measurements. In the lifetime measurement, the detection of photons from a single QD is correlated with a reference signal created by the measurement of a femtosecond laser pulse. The QD is excited by the laser pulse; the exciton then recombines, emitting a photon.

The time difference between the excitation pulse and the QD emission is recorded. The excition lifetime can be extracted from the resulting histogram.

In an autocorrelation measurement, a stream of photons is split at a 50:50 beam splitter into two channels. The photon detections in one channel are correlated relative to the other. The output of this measurement is the second-order correlation function $(g^{(2)}(t))$ of the light source. This measurement is often called a Hanbury-Brown and Twiss (HBT) measurement. This measurement is used to measure the statistics of the input photons, characterising a light source as Poissonian, sub-Poissonian or super-Poissonian.

In a QD cross-correlation measurement, single-photons from one QD transition are correlated with single photons from another QD transition. Photons from the two QDs are sent to two separate single-photon detectors. The output of this measurement is also a second-order correlation function. This measurement is used to identify whether two transitions originate from the same QD or from different QDs.

When using SPDs on both measurement channels, the full measurement time response is a convolution of the two detector responses. Therefore if an HBT measurement is performed using two APDs with response times of 400 ps, the full measurement response time will be roughly 700 ps. This often limits measurements on QDs with moderate Purcell factors.

This page intentionally left blank

4 — GENERATION OF COHERENT ELECTRICALLY DRIVEN SINGLE-PHOTONS COUPLED TO A SINGLE MODE WAVEGUIDE

4.1 Introduction

The generation of single-photons as flying qubits is the basis of many quantum optical technologies [5]. Single-photons can be used to enable protected information transfer in quantum key distribution [1], high precision measurements in quantum metrology [2] and quantum computers [4, 5, 21]. Large scale devices can be enabled by embedding single-photon sources in integrated photonic circuits [27, 35, 42].

Quantum dots [QDs] have been shown to be highly coherent, efficient sources of single photons [53]. QDs can be embedded in nano-photonic devices to create integrated single-photon sources [29]. These photonic devices allow the integration of QDs with devices such as waveguides, cavities or beam splitters, enabling manipulation of the photonic environment of the QD. This can be used to efficiently collect emission from the QD [30, 42] or to enhance the emission rate of the QD using the Purcell effect [29, 42, 57, 90]. These devices can be connected together to scale to larger photonic circuits. Integrated photonic circuitry has great potential in quantum information processing due to the high component densities that can be achieved [42]. In addition, integrated photonic devices aren't sensitive to mechanical noise, reduce the experimental complexity and allow efficient propagation of light over long distances [35].

Most experiments on integrated single-photon sources have relied on optical excita-

tion. Optical excitation can excite a small spot on a sample, allowing for the excitation of single QDs with low background emission [69, 74, 75]. Optically excited single QDs have been used to generate indistinguishable single-photons [53, 91] or photon pairs [136, 137] on-demand, generate single photons with a two-photon emission probability of less than 10^{-5} [59] and to investigate quantum interference of single photons from separate sources [138, 139]. However, optical driving of a multiple QDs presents a challenge. A separate optical path is required to excite each QD, creating a large resource requirement.

One solution for driving large numbers of quantum dots is to use electrically driven single-photon sources. Electrical driving allows continuous [58, 78, 140] or triggered [58, 141] generation of single photons from multiple sources without the need to maintain optical alignment on multiple spatially-separated QDs. Electrical driving of these single photon sources allows simultaneous driving of many single-photon sources in the photonic circuit. In addition to acting as a single-photon source, an electrically driven QD can be used to generate entangled photon pairs [142] and indistinguishable entangled photons [143] via the biexciton cascade; entangled photons from these devices can be used to realise a quantum relay [144].

The main challenge in using electrical driving is limiting the number of QDs that photons are collected from. In the past this has been achieved using a μEL setup to collect emission from a small spot on the wafer [140], or by using diode structures to limit the emission area [58, 78] to limit the active region. Electroluminescence of single QDs in μEL setups has been shown to produce single photons [58, 78, 140] and entangled photon pairs [142, 143]. However this method is not suitable for large-scale integrated photonics, instead the number of QDs coupled to the photonic device needs to be controlled.

This chapter discusses a method of generating waveguide-coupled single photons using electroluminescence from single quantum dots. Single QDs are isolated by three techniques; limiting the area of the sample under bias, limiting the area of the sample that couples to the device, and using a material with a low-density of QDs. Using these techniques, the number of QDs coupled to the device is reduced such that the antibunching of emission from a single QD can be measured. A measurement

of the second-order auto-correlation function of the emission confirms antibunching. $g^{(2)}(0) = 0.07$ is measured, corresponding to a signal to background ratio of 27:1. Electrical driving of quantum dots is often considered to be less coherent than other excitation methods due to the indirect driving mechanism [52] and the relatively large currents required [145]. In addition, placing QDs in waveguides has been shown to reduce coherence [51]; due to the increased charge noise that arises from having surfaces very close to the QDs [51] and the increased sensitivity to phononic modes that arises from the nanobeam structure itself [146]. In spite of this, we show that the device generates photons with a coherence time of (270 ± 10) ps, comparable to results that can be achieved using photoluminescence [86, 147] in membrane structures. This result is also comparable to the highest coherence achieved using QD EL in non-membrane structures [140]. This demonstrates that electroluminescence from quantum dots is a viable source of single photons on-chip.

4.2 Device Design

Overview

The devices need to be designed to support the coupling of single QD EL to single-mode waveguides. The most significant difference in design between these devices and normal devices is the addition of a shallow etch (50 nm deep), which breaks the electrical contact to some areas of the device while maintaining optical transmission. The next section discusses the considerations made when designing devices for single-QD EL. Considerations include the choice of wafer, the position of the shallow etches and the coupling efficiency of QDs to the waveguides. The first consideration when designing these devices is using a wafer which suits our needs. The wafer used is a 170 nm thick $p-i-n$ membrane, allowing both electrical driving and fabrication of single mode waveguides. The top and bottom layers of the membrane are $p-$doped (10^{19}cm^{-2}) and $n-$doped (10^{18}cm^{-2}) respectively, creating a vertical $p-i-n$ diode across the device. A voltage is applied to these layers through electrical connections that are deposited elsewhere on the sample. A low density layer of SAQDs ($\sim$10

QDs/μm^2) is grown at the midpoint of the 170 nm membrane.

The full device consists of three nanobeam waveguides, 170 nm high and 280 nm wide; terminated at one end by a Bragg grating outcoupler. Two waveguides have isolation etches to reduce the number of active QDs that will be coupled to them. The third waveguide is left as a control. A large number of these devices were fabricated; with variations in the position of the isolation etch.

A false-colour SEM image of a fabricated device is displayed in Figure 4-1. The iso-
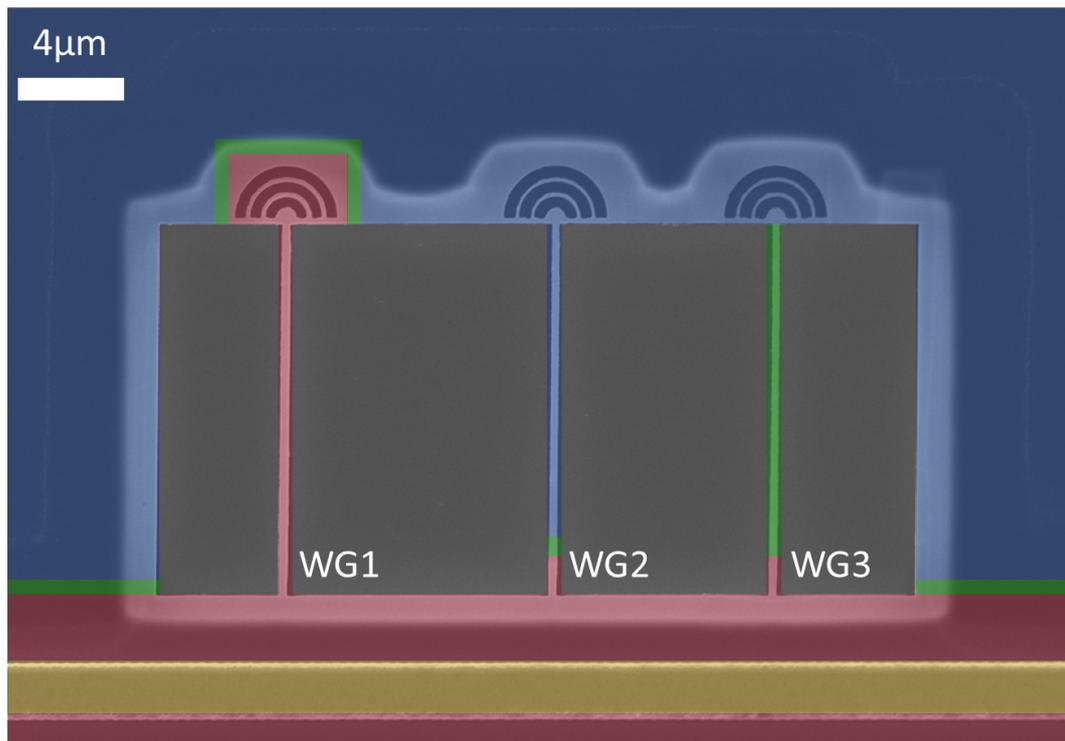

Figure 4-1: False colour SEM image of full set of three waveguides terminated with outcouplers at one end. The area under bias is marked in red; the area unconnected is marked in blue. The etched region that breaks contact to the main diode is marked in green. The metal contact is marked in gold.

lation etch is marked in green on this plot. The area that is connected to the voltage source is marked in red. The area of the device which is isolated from the voltage source is marked in blue. QDs in the red area only will emit EL when a bias is applied to the sample. EL from some of these QDs will couple to the three waveguides.

The left waveguide (WG1) is the control device; it has no isolation etch. This device is used to test whether the isolation etch is successful. This control device also allows us to demonstrate the importance of electrical isolation in reducing background
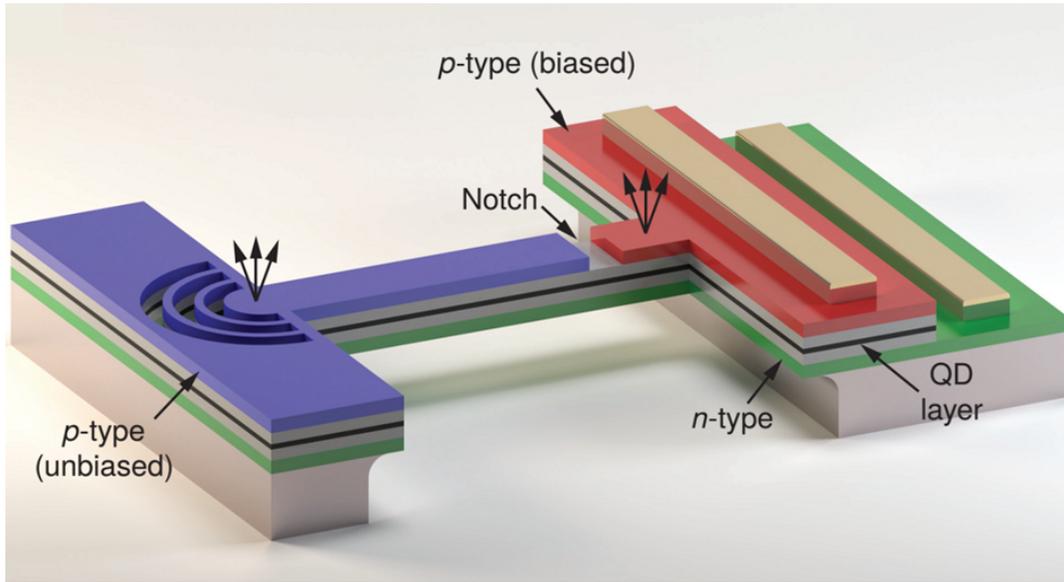
Figure 4-2: Schematic of a single waveguide. Red and blue mark the $p-$doped layer of the biased and unbiased regions of the device respectively. They are separated by a shallow etch, of 1μm width, through the $p-$layer which breaks the electrical contact. The $n-$doped layer of the device is marked in green. The gold bars represent electrical contacts to the $p-$ and $n-$doped layers.

emission in these devices. The centre waveguide (WG2) is the first functional device; it has a 1 μm long, 50 nm deep isolation etch positioned a short distance from the start of the waveguide. The right waveguide (WG3) has a 50nm etch starting at the same position, but continuing along the full waveguide. The starting positions of the two etches are varied between 1 μm and 5 μm on different devices across the sample. The full etch on WG3 is a contingency in case the contact is not completely broken by the 1 μm long etch used on WG2. Removing the p-layer across the full waveguide guarantees that no QDs in the waveguide are active. However the etch changes the waveguide parameters and will have a detrimental effect on the waveguide transmission.

A 3D schematic showing the operation of WG2 is shown in Figure 4-2. Again the active area is marked in red; the isolated area is marked in blue. The isolation etch breaks the electrical contact, but maintains the transmission of light through the waveguide. To reduce reflections off this etched surface a very weak acid is used in the etching process; this gives the etch tapered sides rather than sharp edges.

In the experiment the QDs are driven by applying a voltage to the red area of the

device, emission is collected from the outcoupler. The electrical isolation means that any emission collected from the outcoupler has to originate from QDs at the far end of the waveguide. This allows the measurement of waveguide coupled EL from QDs.

Simulations

In order to observe single-photon EL, it is important that emission from only a few QDs is coupled to each waveguide. This will allow us the spectrally resolve emission from a single QD. In addition, the degree of antibunching will be limited by any background emission in the waveguide. This background emission will come from a large number of QDs which couple weakly to the waveguide, giving a broadband signal which cannot be fully filtered. In order to estimate the number of QDs coupled to a waveguide finite-difference time-domain (FDTD) simulations are performed. These estimate how efficiently light will couple from QDs in different positions to the waveguide.

A simulation of the waveguide mode is shown in Figure 4-3. This simulation shows the electric field density of the optical mode that interfaces between the waveguide and membrane. This field strength determines the coupling efficiency to the waveguide of a QD at the position. This simulation shows that efficient coupling requires the QD to be in the waveguide. The isolation etch breaks the electrical contact 1-5 μm from the start of the waveguide; therefore the area from which QDs will couple efficiently varies between 0.2 μm^2 and 1 μm^2. The QD density is $\sim$10 QDs/μm^2, so between 2 and 10 QDs in each waveguide will couple well. QDs which couple inefficiently will be unsuitable as single-photon sources and need to be filtered out. The simulation shows that the total area from which QDs will be inefficiently coupled (10-50% of maximum E-field) is roughly 2 μm^2 (20 QDs per WG). With 20 QDs coupled to each waveguide, the average spectral separation between QD lines in a device will be 1-2 nm. To isolate single QDs in later experiments, we use a filter of 0.07 nm bandwidth. Therefore we expect it will be possible to isolate almost any single QD line in a device using spectral filtering.

In addition to the region in which light is well coupled to the waveguide, there is a large area from which light couples very weakly ($<$10%) to the waveguide, this
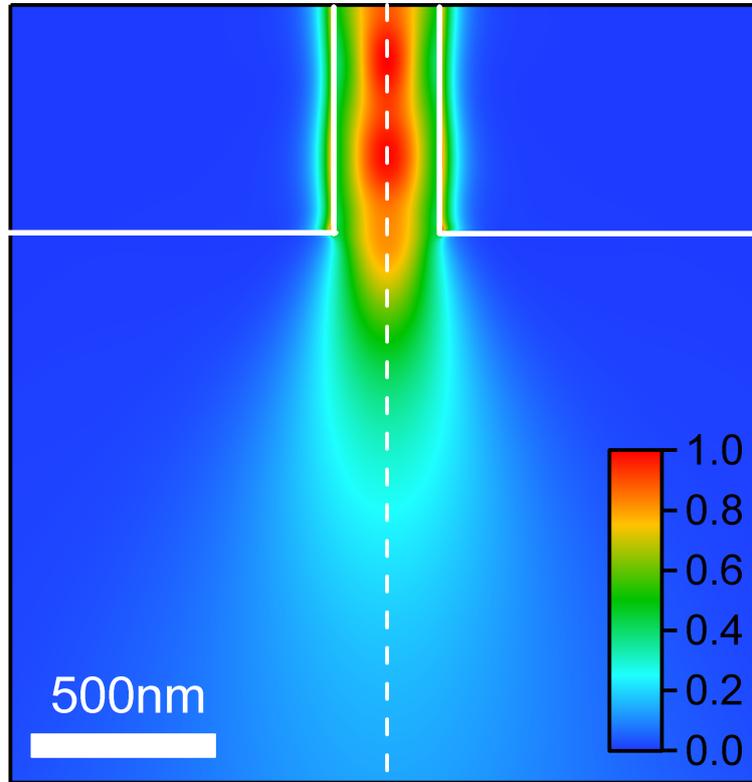
Figure 4-3: Normalised electric field density of the optical mode at the start of the single waveguide in the QD plane obtained by finite-difference time-domain modelling. The etched region is marked by white lines. The field density is used to estimate the coupling efficiency of a QD at that position to the waveguide. The white dashed line indicates the centre of the waveguide.

will contribute a broad background signal which cannot be completely removed using spectral filtering. This simulation cannot be used to estimate the area from which light will couple weakly, as the simulation area itself is too small.

Figure 4-4 displays the coupling efficiency into the waveguide of dipole sources placed at different positions along the waveguide axis. Zero is the position of the waveguide-slab interface. As the waveguide supports transmission in either direction the maximum achievable efficiency is 50%. The simulations indicate that QDs at the within the waveguide will couple with close to maximum efficiency. Figure 4-4 also shows the simulated coupling efficiency out of plane, allowing an approximate comparison of the relative intensity that will be seen from the far end of the waveguide and when using a μEL setup to collect emission out of plane. The simulation indicates that
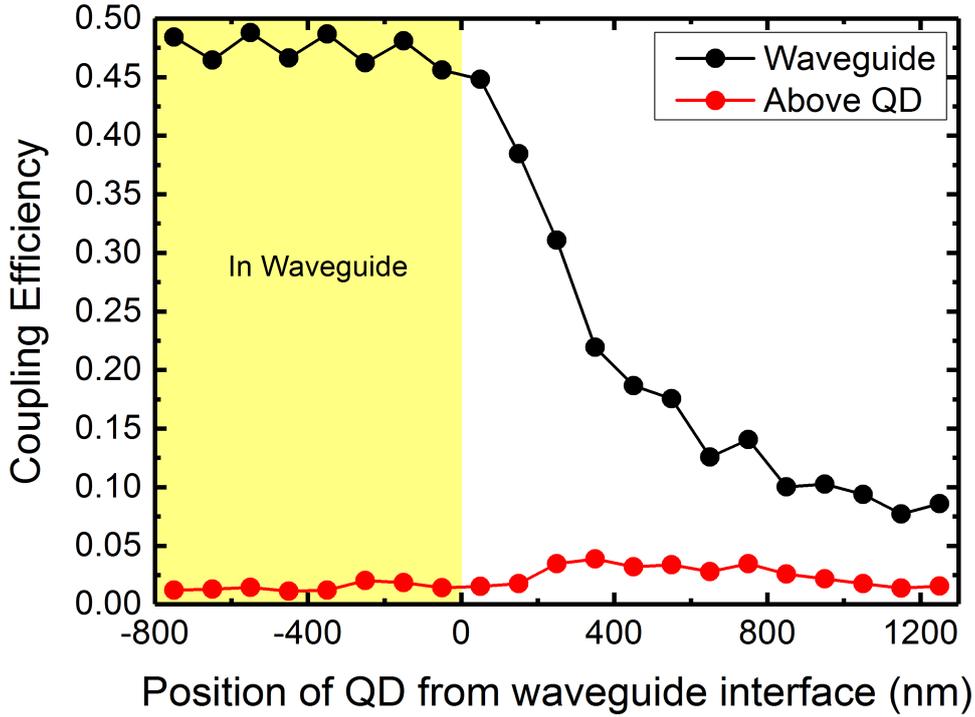
Figure 4-4: Comparison of coupling efficiency to the waveguide and out of plane for dipole sources at various positions along the white dashed line in Figure 4-3. This confirms the behaviour seen previously, coupling efficiency to the waveguide drops off sharply as the dipole is moved further from the waveguide. The measurement above the QD position allows an approximate comparison of the waveguide coupling efficiency to the collection efficiency of a μEL setup.

coupling to the waveguide is significantly more efficient than coupling out of plane. However, the scattering efficiency of the grating coupler and subsequent collection efficiency of the μEL setup is not considered.

4.3 Initial characterisation of an electrically-driven waveguide device

Initial characterisation shows the effectiveness of the isolation etches. For these measurements, voltage is applied to the device such that the QDs emit EL. Usually for a GaAs diode, the EL turn on voltage would be just higher than the band gap energy; 1.52V. In this device however there is some additional resistance from the electrical

contacts to the sample, therefore the EL threshold is at a slightly higher voltage; 2.1V. Figure 4-5 shows a collection map of set of waveguides. This map is obtained by scanning the collection spot of the μEL setup using motorised mirrors and measuring the collected EL intensity using an SPCM. As the output is not filtered, the EL intensity is dominated by emission from the wetting layer. The map area matches the SEM image shown in Figure 4-1.

Emission can be seen from the contacted area at the bottom of the device, and from the three outcouplers. It is clear that emission from the control waveguide (WG1) is significantly brighter than from the other two (WG2, WG3). This indicates that a larger area of this waveguide is emitting EL, implying that the isolation etches have worked. In the control waveguide the entire waveguide, including the outcoupler itself, is under bias; this results in emission from many QDs as well as WL emission from a large area coupling to the waveguide. For the etched waveguide however, only the first 2 μm of the waveguide are under bias, resulting in a much reduced signal. The emission area, and consequently the number of QDs emitting into the waveguide has been limited. The intensity at the outcoupler of WG2 and WG3 is the same, indicating that the 1 μm long isolation etch is effective in breaking the electrical contact and the full waveguide etch is not required. Bright spots are also visible at the interfaces between the slab and the waveguides. The waveguide structure seems to cause increased scatter out of plane. This scatter is significantly brighter on the control waveguide, indicating that this scatter originates from QDs in the waveguides rather than in the bulk area around the start of the waveguide. This scatter is not predicted in the FDTD simulations.

Figure 4-6 shows a comparison of typical EL spectra collected from the outcouplers of etched and control waveguides. This confirms the difference in intensity seen in the PL map. The control waveguide shows a bright wetting layer signal at 860-880 nm and many QD lines at 910-960 nm. In comparison, the etched waveguide shows a dim wetting layer signal and lines from far fewer quantum dots. The single QD lines are no less bright than the lines emitting in the control waveguide. The reduction in the number of QDs coupled to the waveguide means that it is possible to isolate single QD lines in these devices, making these devices suitable for further investigation.
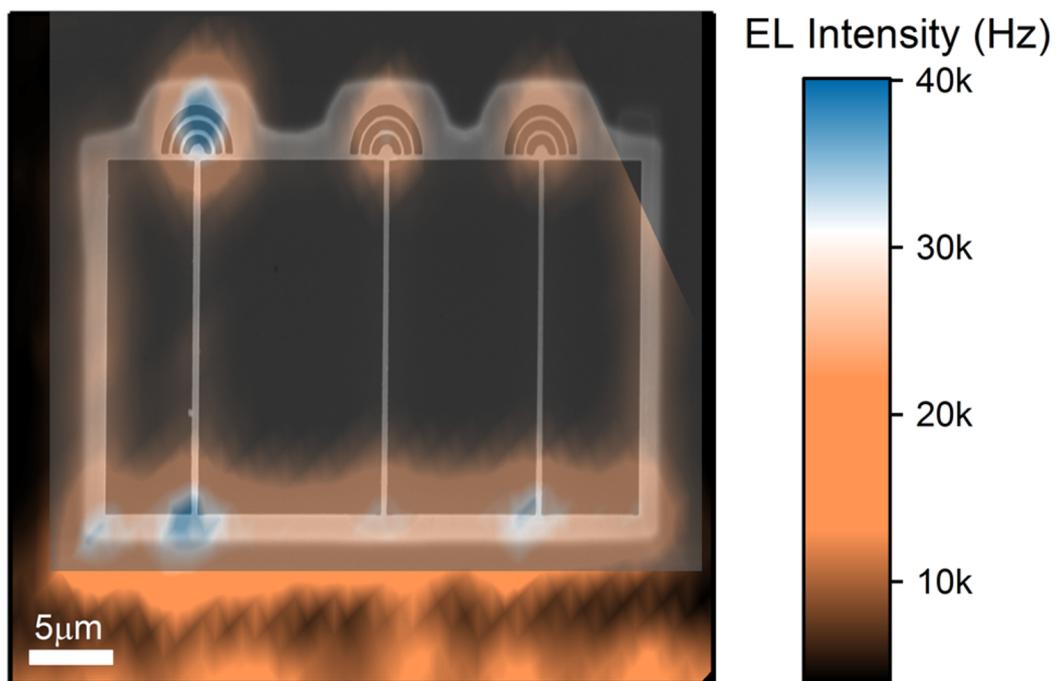
Figure 4-5: Unfiltered EL map of a set of waveguides obtained by scanning the collection spot across the device at constant voltage. An SEM image of the device is overlayed on the map for clarity. The control waveguide is on the left, the other two have isolation etches. Emission can be seen from the contacted area at the bottom of the device and from the outcouplers of the three waveguides.
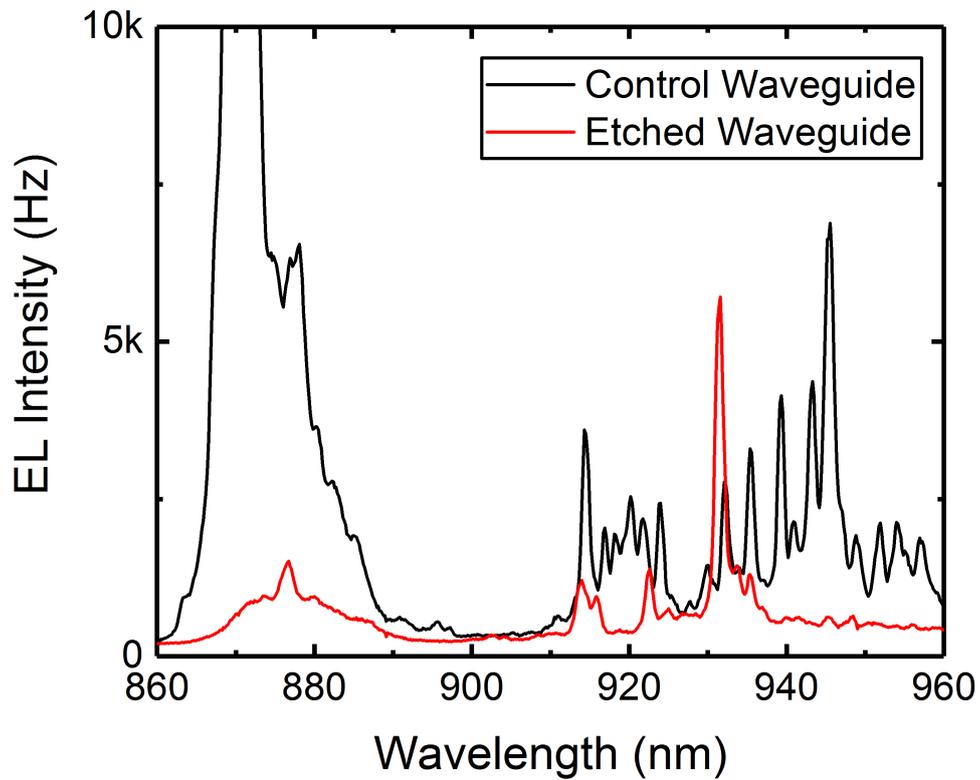
Figure 4-6: Spectrum from the outcouplers of a typical waveguide with an isolation etch (WG2) and the outcoupler of a typical control waveguide (WG1). Fewer QD lines can be seen and the wetting layer emission is dimmer from the etched waveguide. This is due to the electrical isolation, which reduces the area of the waveguide that is under bias.

4.4 Waveguide-coupled emission from a single QD

4.4.1 Characterisation of emission from a single QD

A detailed investigation was performed on a single QD (labelled QD-A from here on) coupled to one waveguide. QD-A is visible from the outcouopler of a waveguide that has an isolation etch (WG2). This QD line was selected because it was relatively bright (saturated count rate: 80 kHz), indicating that it is well coupled to the waveguide and because there is very little emission from other sources at a similar wavelength in this device. In addition, the EL turn on voltage for this line is lower (2.1V) than for most other lines (2.6V), meaning that background emission is further reduced. In the following section, the voltage dependence of emission from this QD is characterised, in comparison to the intensity of emission from the ensemble.

Figure 4-7 compares the emission from the waveguide QD-A at different biases. Figure 4-3a shows a spectrum from the waveguide containing QD-A collected from the outcoupler at 2.1V, the threshold voltage for EL. QD-A is visible at 921.8 nm, weak emission from a small number of other single QDs is also visible. Figure 4-7b shows a spectrum at 2.5 V. At this bias, the brightest emission from QD-A is seen. The total count rate from the line is 80 kHz. The emission is split across multiple data points, so the peak intensity does not represent the total count rate. Emission from other lines is visible, but the ensemble background is still small. At 2.9 V (Figure 4-7c) emission from QD-A is dimmer, this is likely because the change in voltage is changing the charge state of QD-A. More lines are visible in this spectrum, and the broad background is now significant. At 3.3 V (Figure 4-7d) the spectrum is dominated by background emission.

Some of the QD emission is scattered out of plane, this can be measured by collecting emission from above the QD position. Figure 4-8 shows emission collected from above the QD position, at the voltage at which the QD is brightest – 2.5 V. The total count rate from this position is 50 kHz, significantly lower than measured at the outcoupler. Again, the peak intensity does not represent the total intensity because the QD line is spread across multiple pixels on the CCD. The comparative brightness

of the out of plane emission is in conflict with the FDTD simulations, which predicted
that out of plane scattering would be at least ten times weaker than emission into
the waveguide. The difference can be accounted for by the scattering efficiency of the
outcoupler, which is not considered in the simulations. The simulated scattering effi-
ciency of a grating outcoupler is 30%, and collection in the μEL setup is significantly
lower [106].

Figure 4-9 shows a filtered EL collection map. The filtering is performed using a
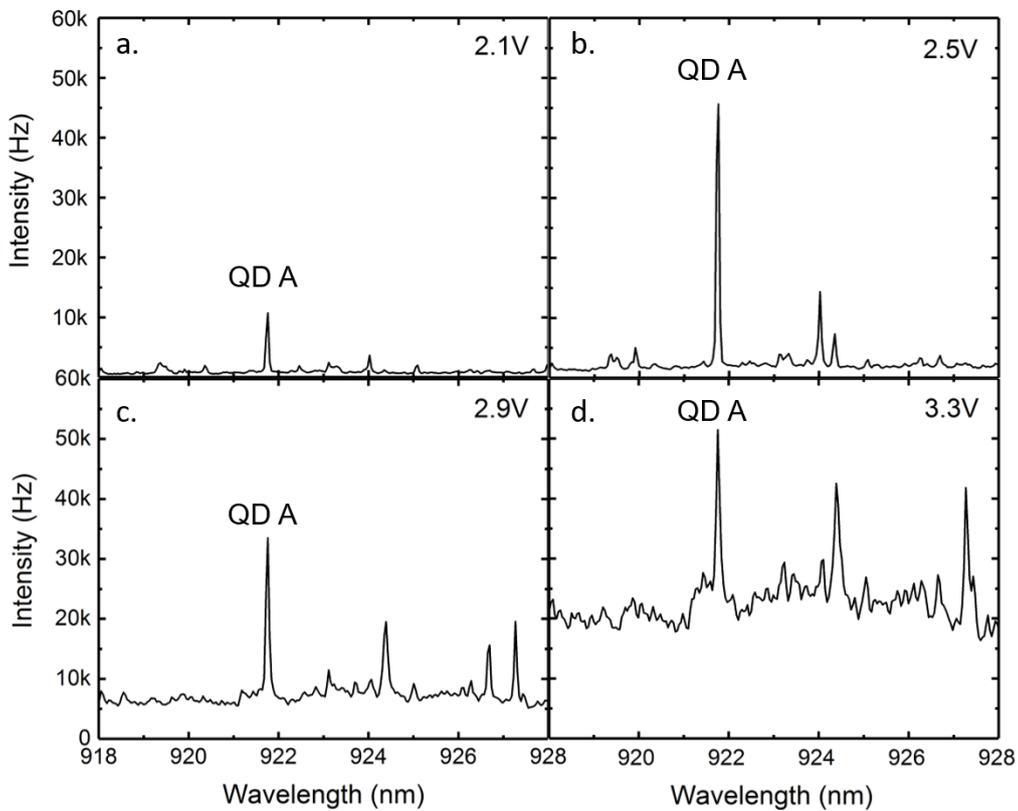

Figure 4-7: EL emission from QD-A, a QD located at the bottom end of a waveg-
uide. The emission is collected from above the outcoupler of the device at (a) 2.1 V,
corresponding to the EL threshold (b) 2.5 V, at which the brightest emission is seen
from QD-A (c) 2.9 V, at which the broad background is visible and (d) 3.3 V, where
the broad background dominates the signal.

spectrometer, the central wavelength of the filter is 921.8 nm and the bandwidth is
0.1 nm. Emission can be seen from both ends of WG1 and WG2. The spectra shown
in Figure 4-7 and Figure 4-8 indicates that the emission seen at both ends of WG2 is
dominated by emission from QD-A. The emission at the lower end of WG2 on the map
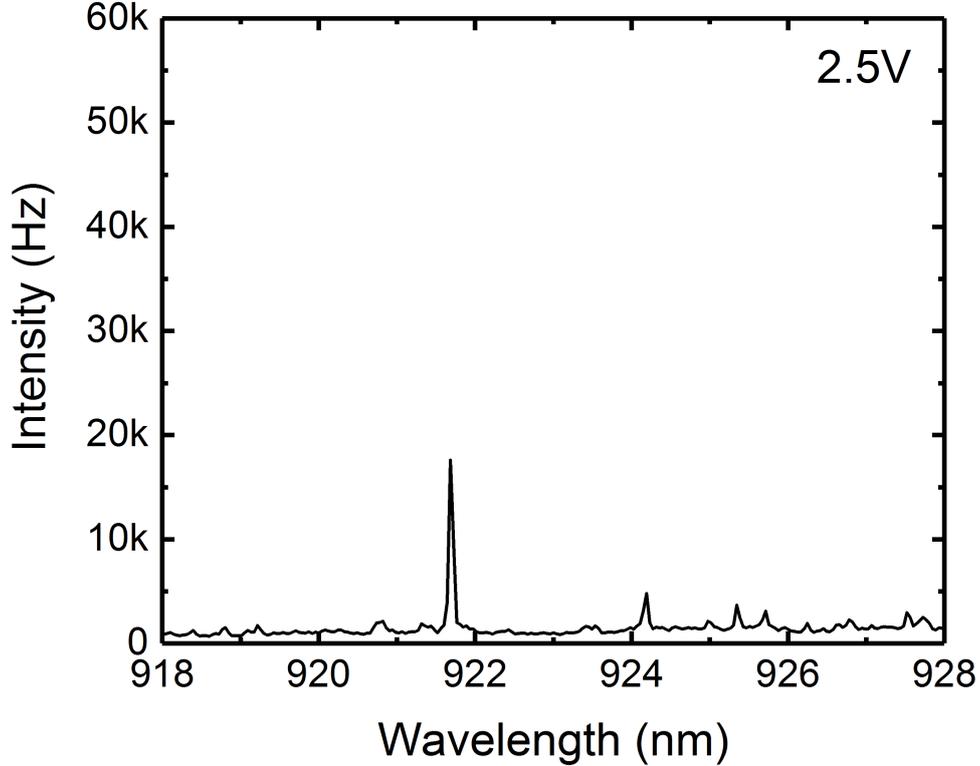
Figure 4-8: Spectrum of QD-A at 921.8 nm collected from above the QD position at 2.5 V, the bias at which QD-A is brightest. The out-of-plane emission of QD-A is comparable in intensity to that collected from the outcoupler, in contrast to the FDTD prediction shown in Figure 4-4.

is EL from QD-A which has scattered out of plane; the location of this bright spot could represent the QD position although the scatter from the waveguide-slab interface makes confirmation of this unreliable. The brightest emission at this wavelength is collected from the outcoupler of WG2; this is EL from QD-A which has coupled to the waveguide. The spectrum in Figure 4-6 shows that emission from WG1 is likely to be from a large number of QDs emitting in that waveguide. Bright emission at this wavelength cannot be seen from WG3, or any other area of the device.

4.4.2 Waveguide-coupled single-photon emission

The quality of the single-photon source is limited by background emission. A quantitative description of the background emission can be obtained by comparing the intensity of the peak to the intensity of the background at various voltages. This
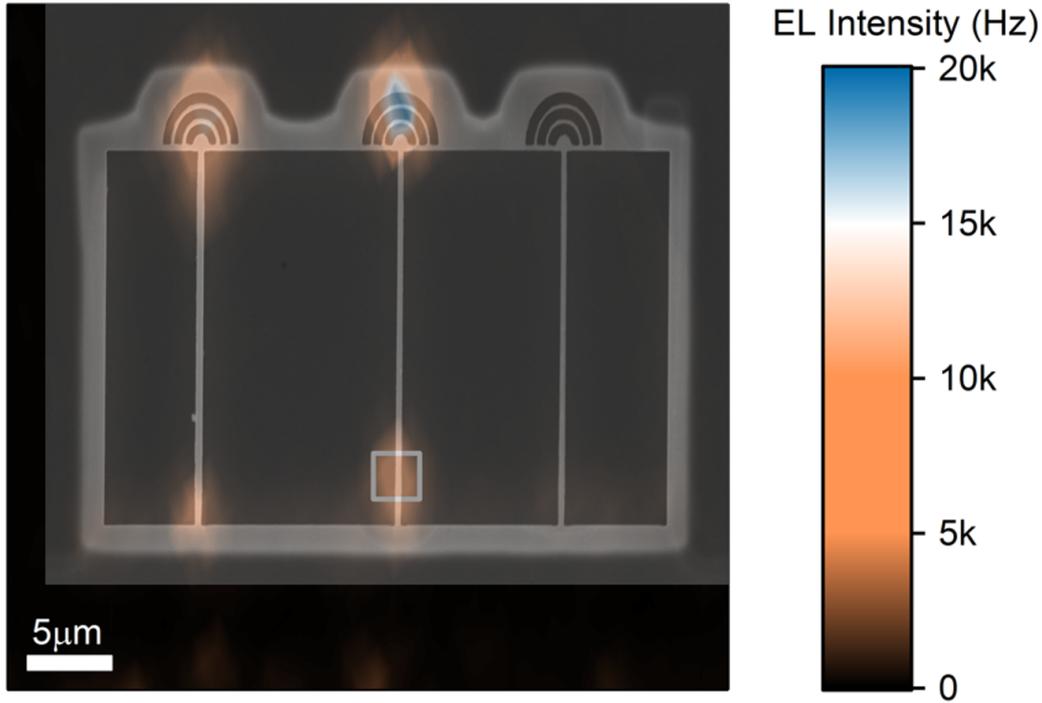
Figure 4-9: Filtered EL map of the device. The filter is centred on QD-A. An SEM image of the device is overlayed on the map. The assumed position of QD-A is indicated by the white box. Emission can be seen from the control waveguide, and from QD-A and the outcoupler of WG2. This measurement confirms QD-A is located in the start of the waveguide.

is done using the spectra in Figure 4-7 and Figure 4-8. The total emission of the peak is compared to the total emission over a range of 0.07 nm. This is used to compare the intensity of the single-photon source to the background intensity that will be collected. 0.07 nm is the bandwidth of the filter used for photon statistics measurements.

Figure 4-10 shows the voltage dependence of the total signal, QD signal, and the background when collecting emission from the outcoupler. The QD emission intensity rises sharply between 2.0 and 2.5 V as the rate of carrier injection is increased. The QD intensity peaks at 2.5 V, and then drops slightly. The drop in intensity is probably due to a change in the charge state of QD-A, caused by an increase in the tunnelling rate of either electrons or holes. The background emission increases gradually as the voltage is increased.

Figure 4-11 shows the signal-to-background ratio (SBR) calculated for QD emission collected from the waveguide and from above the QD position. The highest SBR is

measured when the QD emission is brightest. The SBR drops at higher voltage because the QD intensity is lower and the background intensity is larger. The best SBR is achieved from the outcoupler at a voltage of 2.5V – the voltage at which QD-A is brightest. The SBR peaks at a value of 27:1. From above the QD position the best achievable SBR is 19:1.

The background will increase the chance of two-photon emission in the device. The estimated $g^{(2)}(0)$ of a single-photon source with a background can be calculated using Equation 4.1 [60].

$$g^{(2)}(0) = 1 - \frac{SBR^2}{(SBR+1)^2},$$

(4.1)

Using this equation the estimated $g^{(2)}(0)$ that is achievable from this QD is 0.07 at the outcoupler, and 0.10 at the QD position.

The single-photon nature of the emission is confirmed by a series of Hanbury Brown
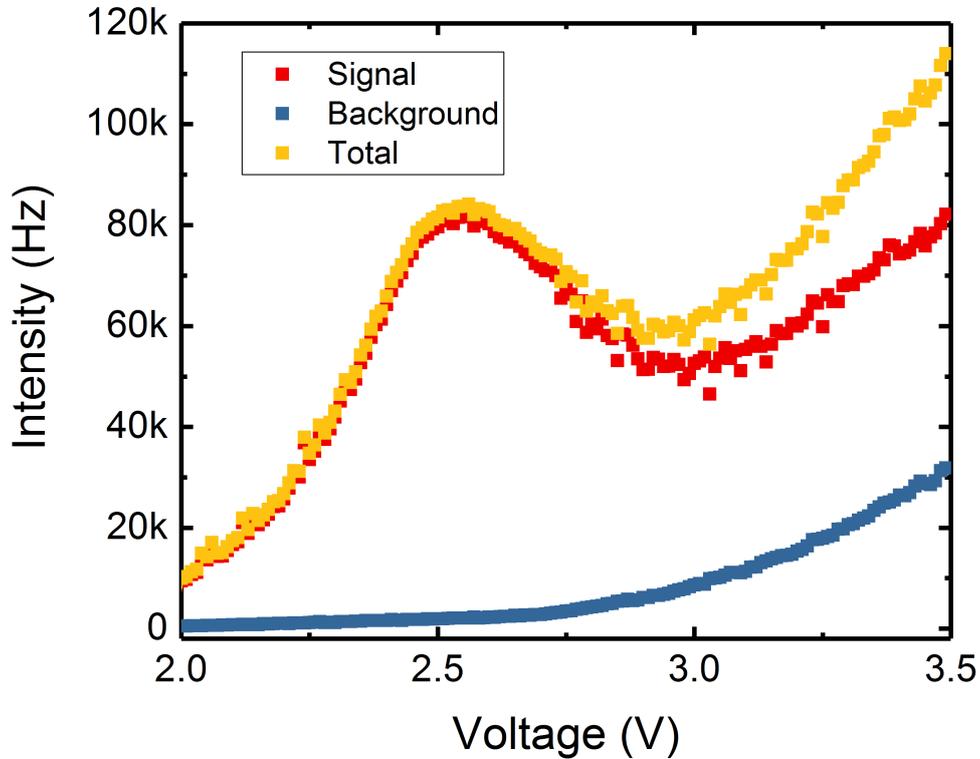
Figure 4-10: QD signal and filtered background emission as a function of voltage. This allows us to identify the optimum operational voltage of the device, at which the signal to background ratio is largest.
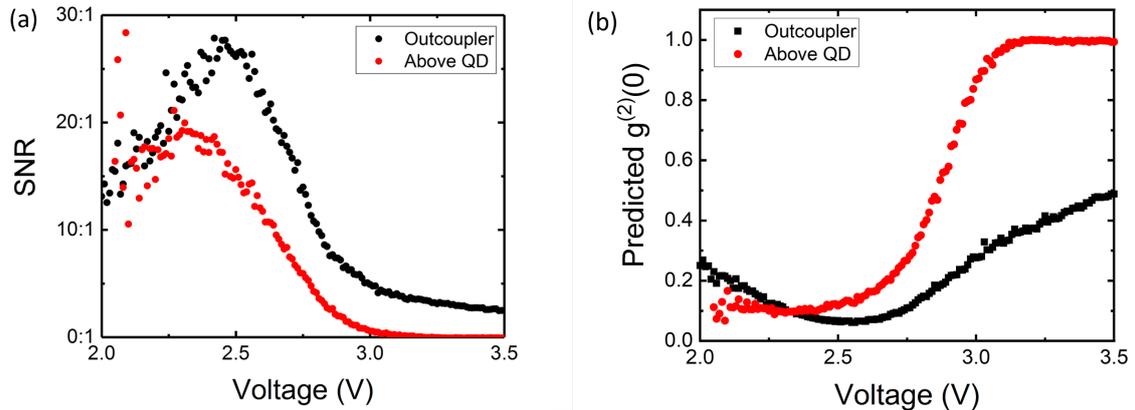
Figure 4-11: (a) Signal-background ratio and (b) corresponding g$^{(2)}$(0), calculated from Equation 4.1, for QD-A as a function of voltage when collecting from the outcoupler and above the QD position. When collecting from the outcoupler the largest SBR is 27:1 at 2.5V, from this SBR a corresponding g$^{(2)}$(0) of 0.065 is expected.

and Twiss (HBT) auto-correlation measurements. The emission from QD-A is filtered through a spectrometer, split at a 50:50 fibre beam splitter and detected by two APDs. Time differences between coincidences on the two detectors are measured. The resulting normalised histograms are displayed in Figure 4-12a and Figure 4-12b. Figure 4-12a shows the second order correlation function for emission from QD-A collected from above the QD position. A value of $g^{(2)}(0) = 0.34$ is measured. The red curve shows a fit to the data; the fit equation is a double-sided exponential curve, convolved with a Gaussian peak (FWHM 870ps). This convolution is required to account for the jitter time of the photon detectors. A lifetime for the QD of $\tau = $ 870ps is obtained from the exponential decay constant. The blue curve shows the double-sided exponential dip without the convolution, this is the true minimum of the antibunching. After accounting for the detector response $g^{(2)}(0) = 0.10$ is obtained. This matches the estimate made from the measured signal-background ratio of 19:1.

Figure 4-12b shows the second order correlation function for emission from QD-A collected from the outcoupler. In this measurement the value $g^{(2)}(0) = 0.07$ is obtained, after accounting for the detector response. This also matches the estimate from the signal-background ratio of 27:1. These measurements both show that the emission is strongly anti-bunched, demonstrating that the device is a source of single photons.

The waveguide improves on the measurement from above the QD in both collection efficiency and SBR.

A cross-correlation measurement is also performed between emission collected from above the QD and from the outcoupler. For this measurement a beam splitter is used to collect from two different positions on the sample into separate fibres; this emission is filtered through two separate spectrometers and sent to two APDs. Time differences between coincidences on the two detectors are measured. The resulting normalised histogram is displayed in Figure 4-12c. Anti-bunching ($g^{(2)}(0) = 0.12$) in this measurement indicates that the emission comes from the same anti-bunched source.
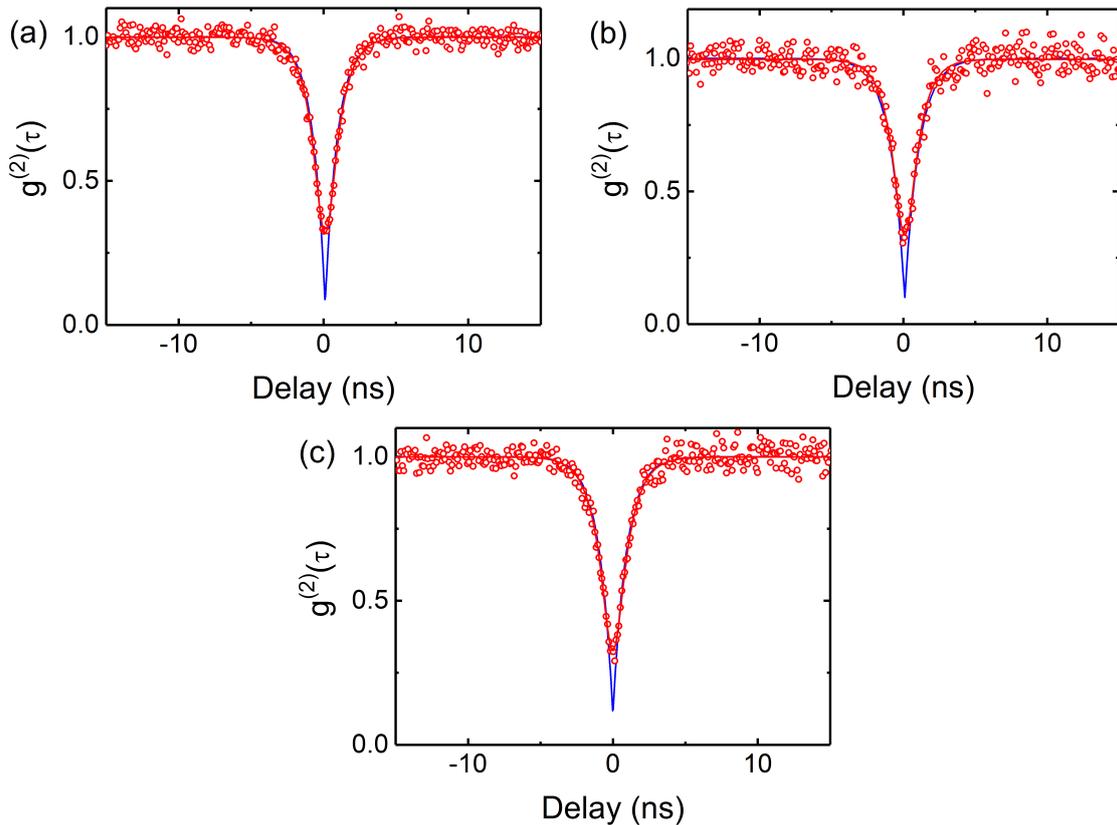

Figure 4-12: Auto-correlation measurements on EL emission (at a bias of 2.5V) collected from (a) the outcoupler, and (b) the QD position. Both measurements show strong antibunching, verifying the single-photon nature of the emission. (c) Cross-correlation between emission from the outcoupler and QD position. This measurement also shows antibunching, verifying that the emission at each end of the waveguide originates from the same single-photon source.

4.4.3 Coherence of single-photon emission

The linewidth of QD-A is smaller than can be resolved using a spectrometer (15 μeV resolution). The linewidth is accurately measured using a scanning Fabry-Pérot interferometer. The Fabry-Pérot interferometer has a resolution of 0.3 μeV. A spectrum of EL from QD-A taken using the Fabry-Pérot interferometer is shown in Figure 4-13. The high resolution spectroscopy shows that the line is actually a doublet, arising presumably from the two fine structure states of a neutral exciton [72]. Here they are labelled X_0^1 and X_0^2. The X_0^1 line is brighter, indicating that it is better coupled to the waveguide. The X_0^1 line has a FWHM of (4.9±0.2) μeV, the X_0^2 line has a FWHM of (5.5±0.3) μeV. The splitting between the lines is 15 μeV. The measured linewidth of the QD is used to calculate the coherence time of the emission using Equation 2.4. The maximum observed coherence time is (270 ± 10)ps.

Figure 4-14 shows the voltage dependence of the coherence time of emission from the two fine structure states. At low biases both lines have a coherence time of 250 ps. As the bias increases the coherence time starts to degrade. This likely cause of this is increased current through the device, which increases charge noise in the environment of the QD. Both lines show the same coherence at low biases, however as the bias is increased the coherence of the emission drops. The X_0^2 line broadens at 2.9 V and the X_0^1 line broadens at 3.1 V. Broadening is expected as the current through the diode, and consequently the charge noise in the device, increases at the bias is increased. Interestingly the X_0^2 line loses coherence at a lower bias, indicating that this dipole is more sensitive to the charge noise arising from the higher current.
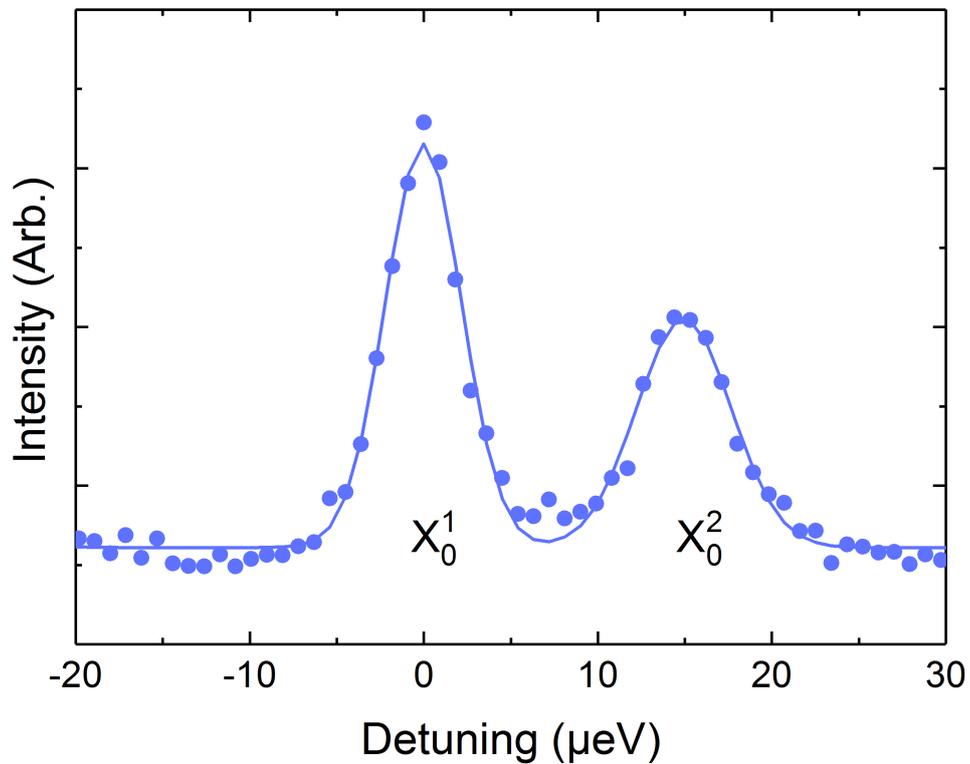
Figure 4-13: High resolution spectrum of the line from QD-A at 2.8V, measured using Fabry-Pérot interferometry. This measurement reveals that the QD line is a doublet, split by 15 μeV due to the fine structure splitting of the QD; the lines are now labelled X_0^1 and X_0^2. The blue line is a fit to two Gaussian peaks.
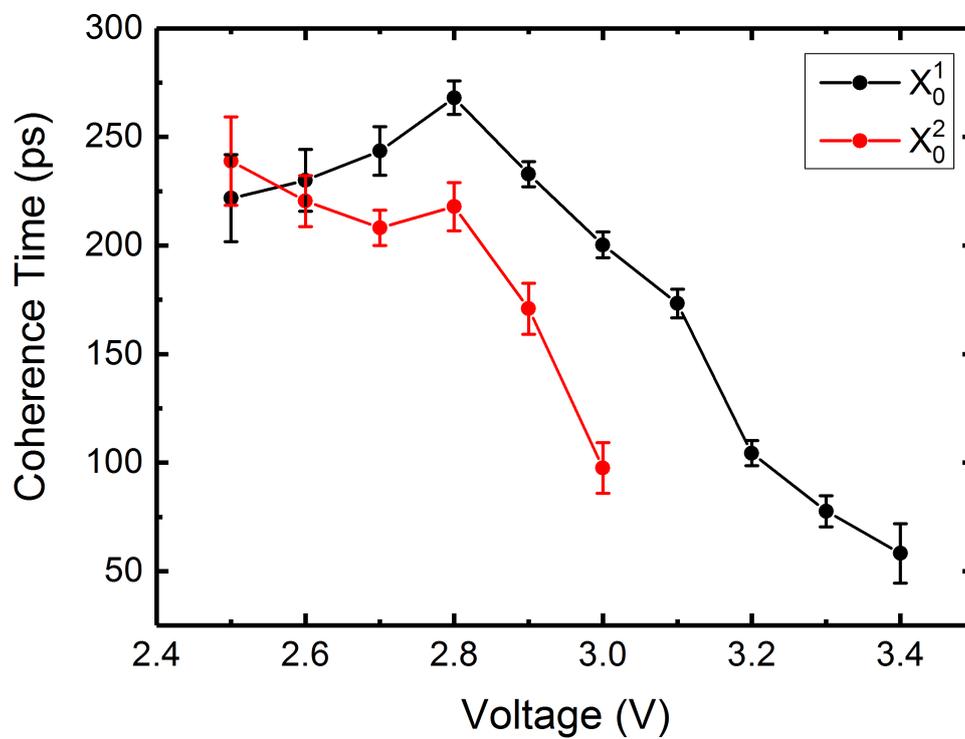
Figure 4-14: Coherence times of the two fine structure states as a function of voltage. Initially both lines show similar coherence times of 200-250 ps. The coherence of the emission drops as the voltage is increased beyond 2.8 V.

4.5 Summary and Outlook

We have demonstrated single-photon electroluminescence from a self-assembled quantum dot coupled to a single-mode nanobeam waveguide. A value of $g^{(2)}(0) = 0.07$ is measured for the second order correlation function of the electroluminescence measured from the outcoupler of the waveguide. The emission is also highly coherent, showing that the method does not inherently reduce the quality of the emitted light. Fabry-Pérot interferometry confirms a coherence time of 250ps for the emission. This coherence time is comparable to the best results measured in thicker structures in EL [140], and photoluminescence in thin membrane structures [86, 147].

The background emission in the waveguide is small due to the small effective collection area of the device. However the maximum signal to background ratio is limited because the open end of the waveguide allows the collection of background emission from a relatively large area. The signal-background ratio could be improved using a device based on a photonic crystal. This could be used to create a mirror on one side of the QD to supress emission from outside the waveguide, giving greater control of the collection area; or to create a cavity, enhancing the emission from the QD.

There is also the potential to improve the electrical control of the source. Resonant injection [145] may reduce charge noise in the device and improve the coherence of the emission. Modulating the voltage could allow the device to be used as a triggered single-photon source [141].

An alternative method is to use indirect electrical excitation. In this method a large diode in the structure is driven electrically, and emission from this device is used to excite the QDs. This achieves resonant driving of multiple quantum emitters. This method has been achieved using LEDs [148] and with micropillar cavities [149].

This device provides the basis for on-chip electrically driven single photon sources which can be easily coupled to other nano-optical components. This development enables photonic circuits with multiple single-photon sources. The shallow etch electrical isolation could also be used to individually tune separate QDs using the Stark effect, enabling devices with multiple QDs in resonance.

5 — ELECTRICAL CONTROL OF A WAVEGUIDE-COUPLED NON-LINEARITY

5.1 Introduction

The efficient generation and manipulation of non-classical states of light is a fundamental requirement of integrated quantum photonic devices. In these devices photons are used as flying qubits. Photons are potentially free from decoherence [22] and can be easily initialised into quantum states of either path or polarisation [24], however photons are limited by their weak interactions with each other [22]. Photon-photon interactions are required for the creation of two-photon logic gates [18], quantum memories [5] or single-photon transistors [25]. Manipulation of these interactions requires low power non-linear optical phenomena, for example the saturation of a single ion [32, 46] or the Hong-Ou-Mandel effect [150]. These interactions enable quantum computing methods such as boson sampling [11, 37].

A two level system can act as both a source of single-photons [14, 29, 30, 53, 56, 57] and as a saturable non-linearity [40, 43], while the waveguide coupling allows coupling of multiple elements together in a compact and scalable architecture [27, 42]. In this scheme photon-photon interactions are mediated by the interaction of each photon with the two level system. Recent work has shown the potential of this approach using InGaAs quantum dots [43, 105, 151], and colour centres in diamond [119, 152]. This nonlinearity can be exploited to create controlled-phase [18–20] or controlled-not [17, 28] logic gates. Exotic states of light, such as photon-photon bound states [38, 41, 117, 153] can be created from the nonlinear interaction. A single-photon nonlinearity is also a powerful optical element that could find uses in optical routing [32]

or single-photon transistors [25]. Crucially, the waveguide architecture allows easy coupling of multiple elements together to create larger photonic networks [42, 76].

Further advances in this direction require local control of the quantum emitters. Electrical control allows static and dynamic tuning, solving problems with charge state instability [26, 154, 155], reducing charge noise [77] and allowing fast switching [79, 141]. Critically, local control of the QD emission energy allows reversible, fast tuning of multiple QDs into resonance, allowing the field to advance beyond single emitter devices. Electrical control is achieved by embedding the QDs in a $p-i-n$ diode; this allows an electric field to be applied to the QDs, allowing control of the charge state [26, 76, 92] by tuning the shape of the tunnelling barriers and control of the QD resonant energy via the quantum confined Stark effect [78–81].

The work in this chapter will demonstrate electrical control of resonant photon scattering from QDs in an integrated waveguide device. The QD behaves as a spectrally tuneable single-photon source and as a switchable and tuneable nonlinear element at the single-photon level. Electrically tuneable resonance fluorescence (RF) is demonstrated from the neutral, negatively and positively charged states of the same QD. In RF measurements the charge state of the QD is controlled and stabilised by an electric field. The performance of the device is improved by the slow-light effect of a photonic crystal (PhC) waveguide [100–102], which increases the radiative decay rate of the QD. In the best case, the QD has a linewidth only 1.4 times larger than the radiative limit. In resonant transmission measurements it is found that the QD has a strong effect on waveguide transmission, reflecting up to 65% of incident photons. Bunching of the transmitted signal and anti-bunching of the reflection signal demonstrates the quantum nonlinear nature of the photon scattering interaction. The RF and nonlinear effect can both be switched electrically on a timescale of 80ns in this device.

5.2   Device Design

The device is deisgned to maximise the visibility of the non-linear effect in transmission, while maximising transmission of the device in the abscence of the QD and

allowing electrical control of the QDs. The device is fabricated on a 170nm $p - i - n$ diode wafer, allowing control of the electric field across the QDs in the z-direction. The limiting factors for the transmission visibility are: the coupling efficiency, the pure dephasing rate, and spectral wandering of the QD. All three of these factors are affected by the radiative decay rate of the QD. The coupling efficiency is improved because the emission rate into the waveguide mode is increased, while non-radiative emission and emission into other modes are not affected. In the model of this system, the effect of pure dephasing and spectral wandering is defined by the ratio of these parameters to the radiative decay rate. Therefore an increase in the decay rate is equivalent to a reduction in these factors.

The radiative decay rate is increased by the Purcell effect. A large Purcell factor could be achieved by placing the QD in a cavity, however this is not ideal for a waveguide-coupled device as the cavity will reflect a large proportion of incoming light and has an extremely narrow operating bandwidth. Instead we use a photonic crystal waveguide; this allows high coupling efficiencies and a Purcell factor due to the slow light effect while having a reasonable operating bandwidth and high transmission.

A schematic of the sample is shown in Figure 5-1. The key feature of the device
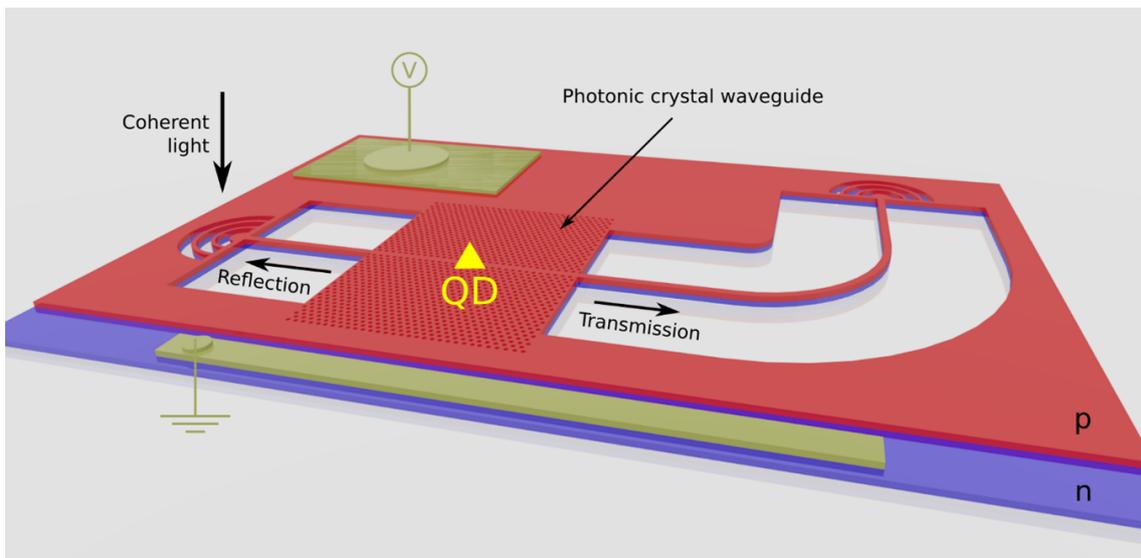

Figure 5-1: Schematic of the transmission experiment. The transmission and reflection of a single QD in a PhC waveguide is measured. The QD energy can be tuned electrically via the quantum confined Stark effect.

is the single-mode slow-light PhC W1 waveguide. This is the section of the device
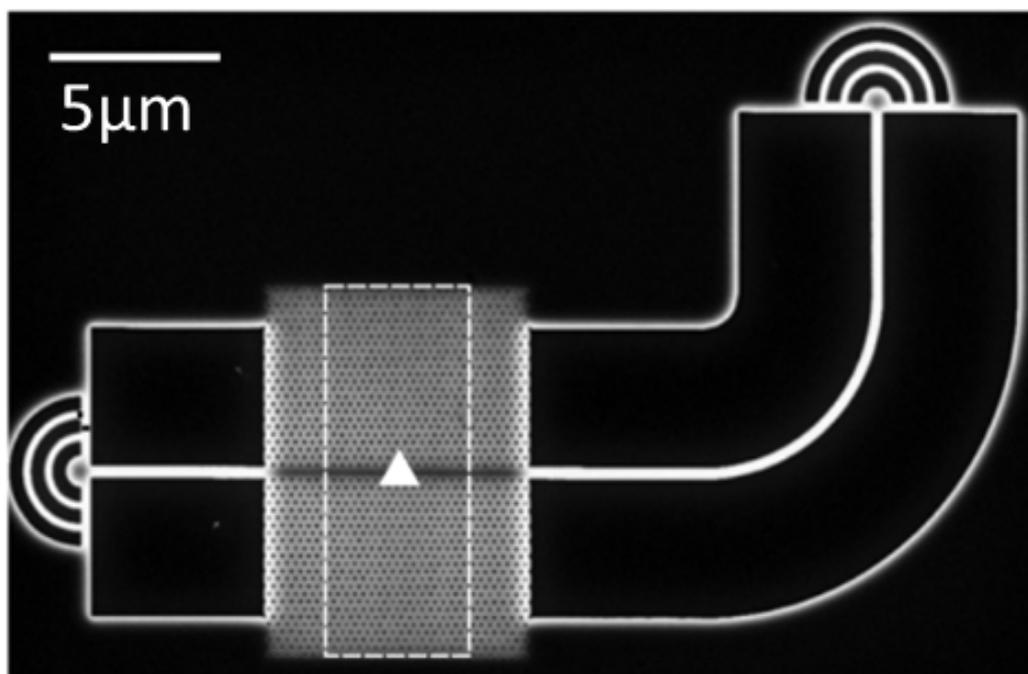
Figure 5-2: SEM image of a full waveguide device. The white dashed box indicates the slow light region of the PhC waveguide. The triangle shows the rough location of the QD studied.

where QDs will be Purcell enhanced by the structure. The PhC waveguide is coupled to two nanobeam waveguides that are individually terminated with Bragg grating outcouplers for vertical in- and out-coupling of light. Intermediate PhC waveguides with a larger hole separation are fabricated on either side of the main PhC waveguide section to gradually change the group index of the PhC waveguide [156], this reduces the intensity of back reflections from the PhC-nanobeam interface. In addition, the PhC-nanobeam interface is designed to minimise reflections [157].

An SEM image of the final device is shown in Figure 5-2. The position of the central slow-light section of the PhC waveguide is marked with a white dashed box; the PhC regions outside this area are the previously mentioned intermediate regions. The location of a suitable QD is marked with a white triangle. There is 90 degree bend in one nanobeam, making the optical excitation and collection polarisations orthogonal. This allows efficient in- and out-coupling to the device while scattered laser light is rejected.

66

5.3 Characterisation of photonic crystal waveguides

In order to have a large Purcell factor in a W1 PhC waveguide, the QD energy needs to be close to the lower band edge of the waveguide. We find the band edges of different devices using high-power above-band photoluminescence; this excites the QD ensemble and produces broadband emission from 890 nm to 940 nm. This is used to measure the transmission of the waveguide over a wide wavelength range.

To account for fabrication uncertainties, a range of devices were produced with
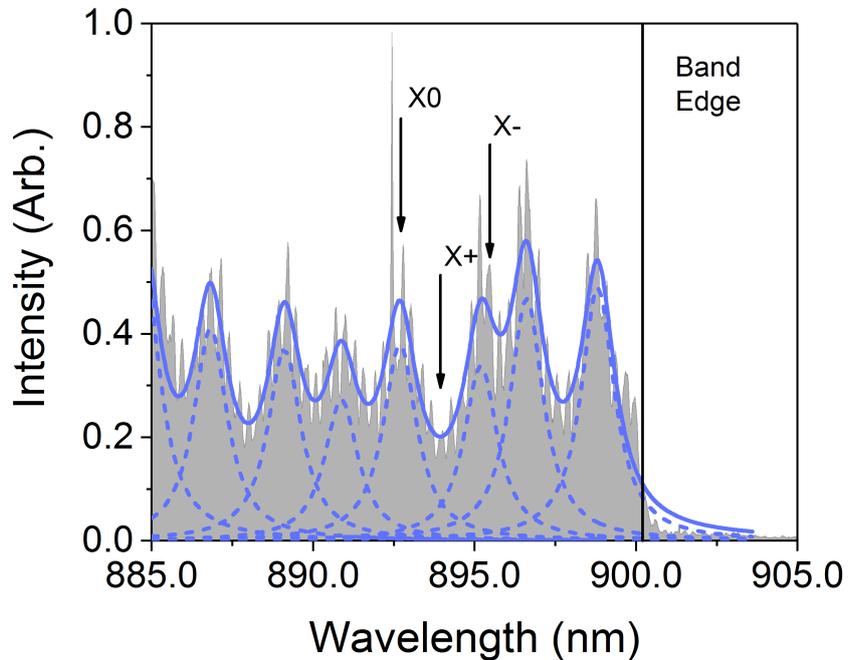

Figure 5-3: High power PL spectrum showing emission from the ensemble of QDs in the PhC waveguide. The band edge of the waveguide is seen at 900 nm, indicated by a solid back line. Peaks are visible from the Fabry-Pérot (F-P) modes in the waveguide. The solid line is a fit of multiple Gaussian peaks to the data. The dashed lines indicate the individual Gaussian peak of each F-P mode. The spectral positions of the three excitons studied in the next section are indicated.

different hole sizes. Changing the hole size shifts the energy of the band edge of the waveguide. In order for a device to contain QDs with a Purcell factor it is required for the band edge to be within the QD ensemble emission range.

The PL spectrum of one device is shown in Figure 5-3. For this measurement, a high power (500μW) 808nm (above-band) laser is incident on one outcoupler of the

67

device. The laser excites many QDs in and around the outcoupler, producing a broad light source. This broad emission passes through the full length of the waveguide, and is scattered by the other outcoupler for collection. Therefor,e this spectrum is a measurement of the wavelength dependent transmission of the waveguide.

The PL spectrum shows that the band edge of this device is at 900 nm, the waveguide doesn't transmit light of longer wavelengths. Similar measurements on other devices with different hole sizes show band edges at 920 nm and 940 nm. Some of the devices have band edges shorter than 890 nm and show no transmission, or band edges longer than 940 nm and show the full QD ensemble emission.

The waveguide transmission is modulated by Fabry-Pérot (F-P) modes. These are standing modes that create fringes of high and low waveguide transmission. The modes arise due to reflections off interfaces within the waveguide. These reflections could come from several sources: the outcouplers, the PhC-nanobeam interface, or the intermediate PhCWG interface. Here we determine from the properties of the modes which interface is most likely to be causing the modes. For this we use Equation 5.1 describing the free spectral range of a F-P cavity.

$$\Delta\nu_{FSR} = \frac{c}{2n_g l},$$
(5.1)

where l is the cavity length and n_g is the refractive index of the material.

Using this equation, the measured mode period (2 nm), and the refractive index of GaAs (3.4) we calculate the length of the cavity forming these F-P mode to be roughly 50 μm. The length of the full device is 30 μm, while the length of the PhC section is 8 μm. From this we conclude that it is most likely that the reflections arise from the outcouplers at each end of the waveguide and that the group index in the PhC region of the structure is higher than the index of bulk GaAs due to the slow light effect. This conclusion is supported by a measurement of the finesse of the cavity. The finesse of a F-P cavity is described by Equation 5.2.

$$F_C = \frac{2\pi}{-ln(R^2)},$$
(5.2)

where F_C is the finesse of the F-P modes and R is the reflectivity of the interfaces. The finesse of the modes is calculated to be 1.6. From Equation 5.2 we calculate the reflectivity of the interfaces to be 23%. FTDT simulations of the PhC-nanobeam interface indicate that the reflectivity of these interfaces is <10%, while nanobeam-coupled outcouplers have been known to have reflectivities as high as 20% [107]. This supports the conclusion that the F-P modes arise from reflections off the ends of the waveguide.

5.4 Results

In order to demonstrate electrical control of a waveguide-coupled non-linearity we perform a detailed study one QD coupled to a PhC waveguide, which exhibits promising properties as a 1D atom. This QD is representative of the results that can be achieved with this device. We fully explore the properties of this device using photoluminescence, resonance fluorescence and resonant transmission measurements. We study three different charge states of this QD.

Quantum dot characterisation

To identify a high quality QD for transmission measurements, we first measure many QDs using photoluminescence. This allows us to identify QDs with low rates of spectral wandering and high coupling efficiency, with energies close to the PhC waveguide band edge. In this measurement, QDs in the PhCWG are excited by an 808 nm laser at a power of 1.3 μW, emission from the QDs is collected from an outcoupler of the device. This emission is measured using a spectrometer.

 Bias dependent photoluminescence from the QD is shown in Figure 5-4. Three lines are visible from the QD at different biases; these are from the positive ($X^+ - 894$ nm), neutral ($X_0 - 893$ nm) and negative ($X^- - 896$ nm) excitons. The three lines are bright relative to lines from other QDs in the device, indicating that the coupling efficiency of this QD is high. In addition, all three charge states have narrow linewidths ($<15\mu$eV), indicating that the variance of spectral wandering in these states is low.
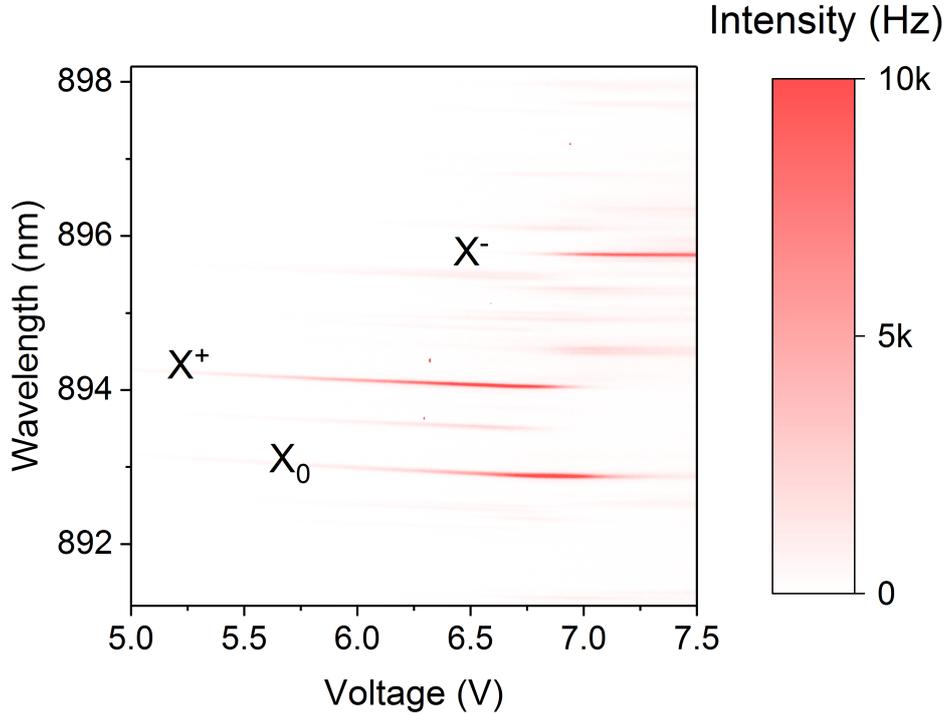
Figure 5-4: Photoluminescence intensity versus wavelength and bias for the QD under study. Three charge states of the same QD can be seen, labelled as the neutral (X_0), positively charged (X^+) and negatively charged (X^-) exciton states.

Finally, these three lines are all close to the device band edge of 900 nm, indicating that they are likely to have a Purcell enhanced decay rate. The position of the charge states relative to the waveguide modes is indicated in Figure 5-3. The active charge state of the QD can be controlled using the bias. The X^+ is active between 5.5 and 6.8 V, the X_0 is active between 6.0 and 7.2 V and the X^- is active at voltages larger than 6.9 V. The voltage ranges of the charge states overlap in this measurement because above band photoluminescence creates many free charge carriers, which can relax into the QD and change the charge state. In later resonant measurements, the voltage ranges of the charge states don't overlap.

The bias also allows fine tuning of the QD energy via the QCSE. The charge states each shift to shorter wavelength as the bias is increased. The tuning range of each state is limited by the voltage range at which it is active. The X^+ has the largest tuning range of 0.25 nm, the X_0 has a range of 0.15 nm and the X^- tuning range is too small to measure on the spectrometer.

We note that this wafer has a large series resistance, arising from low dopant density in the $n-$layer. Therefore the applied voltage does not represent the voltage across the diode. Flat band conditions for the device are observed at 7.5 V, at this bias the diode has 1.5 V across it. Much of the voltage is lost across the resistive $n-$layer. This high voltage requirement does not appear to have any adverse effect on the QD properties. In addition, there is a large current density ($\sim 10\text{mA/mm}^2$) flowing through the sample at the biases used. This also does not appear to affect the QD properties, as the results we measure are comparable to the best results in devices designed to minimise current flow [77]. It is likely that a large part of this current flows through areas of the device far away from the QDs under study and therefore do not affect the device being studied.

Cross-correlation measurements

To prove that these three lines originate from the same QD, cross-correlation HBT measurements are performed. These measurements are possible because of the voltage overlap of the charge states in PL, which allows two charge states to be active at once.

In this measurement the bias is set to a value at which two charge states are active (6.6 V for the X_0 and X^+ states and 7.0 V for the X_0 and X^- states). The PL signal at this bias is split and filtered using two separate spectrometers to isolate emission from the two lines. The output from the spectrometers is then directed onto two SPCMs.

Figure 5-5a and Figure 5-5b show the results from cross-correlation measurements on lines from the QD under study. Both measurements show clear antibunching of the signal, indicating that the two lines originate from the same source.

For comparison, Figure 5-5c shows a control measurement performed on the X_0 state and a line from a different QD. This measurement shows no antibunching because the two lines are from separate QDs.

These cross-correlation measurements also reveal interesting information about the
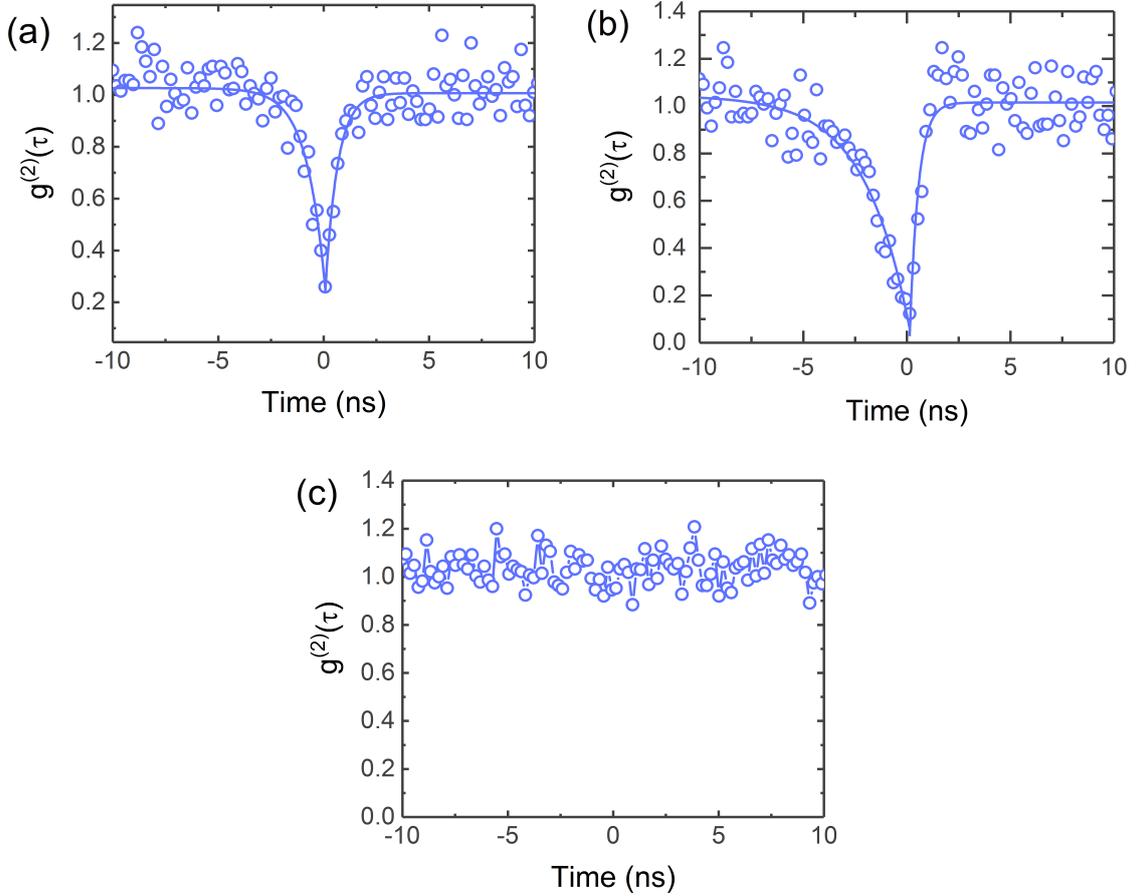
Figure 5-5: Cross-correlation measurement between (a) the X^+ and X_0 charge states, (b) the X^- and X_0 charge states and (c) control measurement on two lines from different QDs. Cross-correlation measurements between lines originating from the same QD display antibunching.

charge dynamics of the QD. In Figure 5-5b, it can be seen that the decay constant for the antibunching is clearly not symmetric, whereas in Figure 5-5a the decay constant is symmetric. This difference is caused by the different switching times of the QD charge states.

The cross-correlation measurement shows the time difference between photons emitted from the different states. Positive time represents a photon from one particular charge states arriving after the other, a negative time difference represents the photons in the opposite order. Therefore the decay constants in these measurements represent the average time for the QD to switch charge state. For example, in Figure 5-5b the positive time constant represents the average time taken for the QD to switch from the X^+ state to the X_0 state and negative time represents the time for

the QD to switch from the X_0 back to the X^+ state.

The cross-correlation measurements are each fitted with two exponential curves to determine the switching times for each exciton transition. The switching time for the four transitions are: $t(X_0 \to X^-) = 0.8$ns, $t(X^- \to X_0) = 0.6$ns, $t(X^+ \to X_0) = 0.55$ns and $t(X_0 \to X^+) = 1.8$ns.

In particular we note that one transition takes significantly longer than the other three. The switching times for the $X_0 \to X^-$, $X^- \to X_0$ and $X^+ \to X_0$ transitions are all <0.8 ns, whereas the switching time for the $X_0 \to X^+$ transition is over twice as long. Tuning of the QD from the X_0 to X^+ state appears to be constrained by the charging mechanism, which requires an electron to tunnel out of the X_0 exciton while the exciton is in the excited state.

Later in this chapter, we observe that resonant measurements on the X_0 and X^- state do not require optical stabilisation, whereas the X^+ state does require this laser. This lack of stabilisation is due to the different charging mechanism of this state, evident here.

5.4.1 Resonance fluorescence on a charge-controlled QD

In preparation for the resonant transmission measurements we extract relevant information about the QD using resonance fluorescence (RF). Using RF we measure the linewidths and the charge plateaus of the different charge states, and measurements of the lifetimes and coherence times of the QD states.

In these measurements the QD is excited from above by a resonant laser at 425 nW.The QD then emits photons into the waveguide and emission is collected from an outcoupler. The excitation laser itself does not couple directly to the waveguide, allowing a high signal-background ratio. Both the laser wavelength and the QD transition energy can be tuned in the following measurements. Background measurements at each point are taken for each point by tuning the QD to another charge state, allowing background emission to be removed from the measured signal.

The three charge states are all visible in RF. Large range bias dependences of the X_0 and X^- are shown in Figure 5-6 and Figure 5-8 respectively. A bias dependence of RF from the X_0 exciton with the laser wavelength constant is shown in Figure 5-7. RF

spectra from the X^- and X^+ excitons with the bias constant are shown in Figure 5-9 and Figure 5-10 respectively. No RF bias dependence is shown for the X^+.

The three lines are active over three different charge plateaus, in contrast to the PL measurement there is very little overlap in these charge plateaus. The X^- is active between 6.9 and 7.8 V, the X_0 between 6.5 and 6.9 V, the X^+ is active between 5.5 and 6.5 V. All three charge states tune to higher energy as the voltage is increased. The X^- tunes 20 pm, the X_0 tunes 50 pm. The tuning range of the X^+ is not measured in RF, but it is determined in later resonant transmission measurements (Figure 5-19) to be 150 pm.

RF allows accurate measurement of the linewidths of the different states, which are too narrow to be measured using the spectrometer. This is done by tuning the laser through the QD transition, and measuring the RF intensity at each wavelength. The linewidth of the X^- is $(5.1 \pm 0.1)\mu$eV and linewidth of the X^+ is $(11.7 \pm 0.4)\mu$eV. The X_0 is a doublet with linewidths of $(4.8 \pm 0.2)\mu$eV and $(3.1 \pm 0.1)\mu$eV. All three lines are best fit by Lorentzian fits, indicating that while the states are broadened by spectral wandering this wandering is in the 'motional narrowing' regime [88].

 The X_0 is clearly identified by the two fine-structure states that are visible in RF. These states have been labelled X_0^1 and X_0^2 in Figure 5-7. These two states have a splitting of 36 μeV. The X_0^1 is both brighter and broader than the X_0^2. It is expected that the orthogonal polarisation of the fine structure states will produce different coupling efficiencies depending on the position of the QD in the PhC waveguide [104]. The difference in linewidth is more unexpected, but is also caused by the orthogonal polarisations of the states [72] and the proximity of GaAs-air interfaces near the QD [51]. Figure 5-7 shows a voltage sweep of the X_0^1 and X_0^2 states and the corresponding background emission. This measurement was taken by fixing the laser wavelength at 892.99 nm and using the bias to tune the charge state through resonance with the laser. This measurement is equivalent to the spectra taken by changing the laser wavelength, as the QD energy is tuned by the bias. However tuning the laser can produce fluctuations in the background laser intensity, whereas tuning using the bias does not. The figure shows the RF signal compared to the background, which has contributions from the reflected laser and from wetting layer EL. The peak of the

signal is at 6.63 V, at this point the SBR is 200:1. Detector dark counts (20 Hz) have been subtracted from both sets of data.

It is worth noting that resonant measurements can be performed on the X_0 and X^- states without the application of a non-resonant laser; in other work a weak above-band laser was required to stabilise the charge state of the QD [133, 158]. In these measurements the QD would become trapped in a charge state that was not resonant with the laser; the non-resonant laser would free the QD from this dark state. In this work the $p-i-n$ diode stabilises the charge state for the X_0 and X^- states [159] so the QD is always in the same charge state. Resonant measurements on the X^+ charge state do require the application of a non-resonant laser, indicating that the diode does not stabilise this charge state.

The X^+ shows a significantly larger linewidth than the other charge states of the QD; the measured linewidth is over double that seen for the other two lines. This larger linewidth is the result of a higher variance in spectral wandering. It is likely that this spectral wandering is caused by additional charge noise arising because of the charge instability in the device.
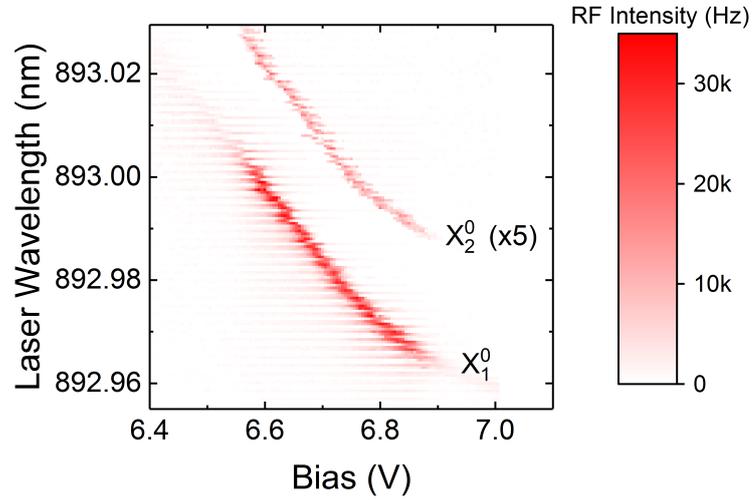
Figure 5-6: RF intensity as a function of laser waveguide and bias for the neutral (X_0^1 and X_0^2) lines. The intensity of the X_0^2 line has been scaled by a factor of 5 for clarity.
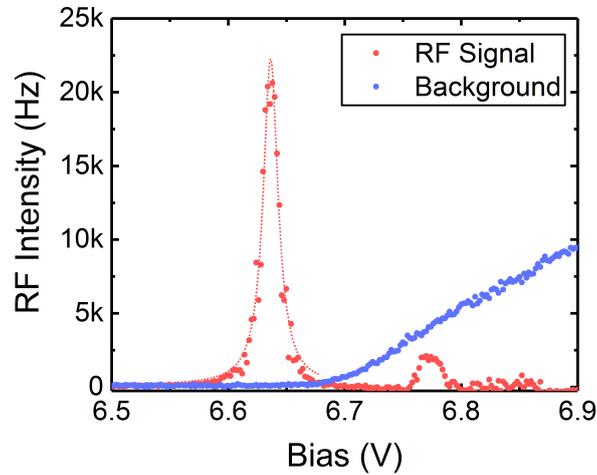

Figure 5-7: Bias dependence of RF from the X_0 state (red) with counts (blue). The laser is held at 892.99 nm. This bias dependence looks very similar to a spectrum, as the QD-laser detuning is changing with bias, which brings the QD states through resonance with the laser. The dotted line is a Lorentzian fit to the X_0^1 line. A signal-background ratio of 200:1 is measured at the peak of the X_0^1 line.
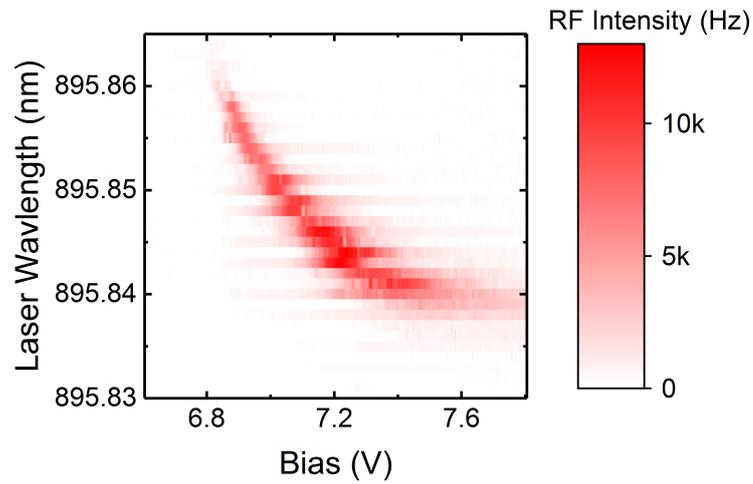
Figure 5-8: RF intensity as a function of laser waveguide and bias for the negatively charged (X^-) line. The QD does not tune past 895.84 nm despite the increase in bias, indicating that the diode is at flat band and the resistance of the device is dropping.
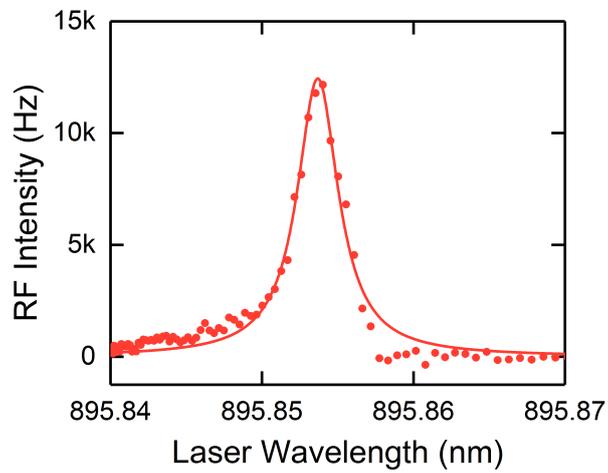

Figure 5-9: Single RF spectrum from the X^- line. The bias is held at 6.95 V and the laser swept through resonance. The solid line is a Lorentzian fit with a linewidth of $(5.1 \pm 0.1)\mu$eV.
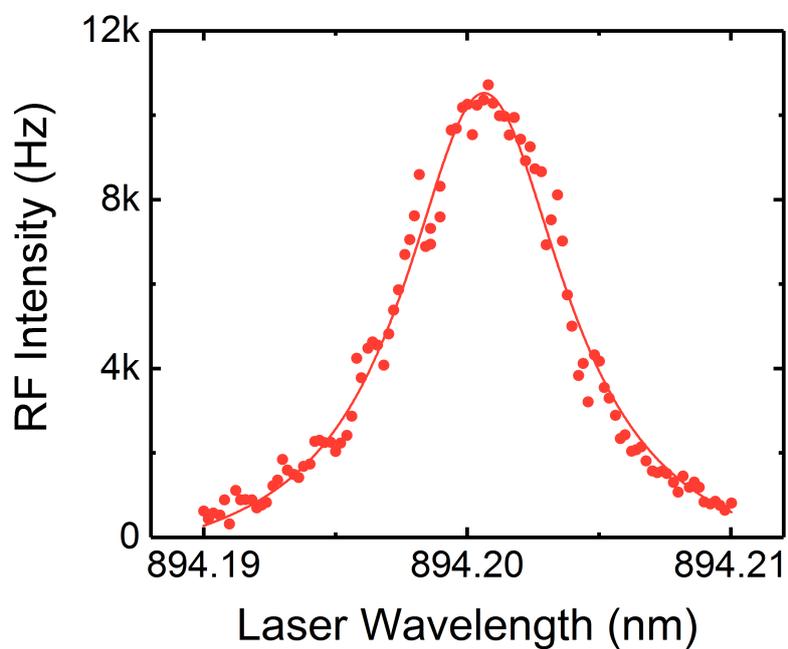
Figure 5-10: Single RF spectrum from the X^+ line. The bias is held at 6.26 V and the laser swept through resonance. The solid line is a Lorentzian fit with a linewidth of $(11.7 \pm 0.4)\mu$eV.

Resonant Lifetime and Coherence Time

RF measurements were used to measure the lifetime and pure dephasing time of the QD states. The lifetimes of the X_0 and X^- lines are measured using pulsed RF. A femtosecond pulse is filtered through a spectrometer, producing a final pulse roughly 40 ps long and 10 pm broad. This pulse is used to excite the QD as in the previous RF measurements. The laser pulse is measured by a photodiode, and QD emission is measured by an SNSPD. The pulses from the photodiode and detector measured by a time-correlated photon counting card [135]. The total system response time is 70 ps. The arrival times of photons from the QD are compared to the times of the laser pulses. Two measurements are taken for each result, one with the QD resonant with the laser (signal), one with the QD detuned (background). This allows laser background to be removed from the lifetime measurement.

The lifetime measurement for the X_0 state is shown in Figure 5-11. There are three components to the measured signal: RF signal from the QD, some residual laser background, and electroluminescence from other QDs. The residual background signal gives a Gaussian pulse at time zero, this is light that hasn't interacted with the system. The EL gives a flat background with no time dependence. The RF emission from the X_0 state gives an exponential decay, with a decay constant equal to the QD lifetime. It is assumed that most of the signal comes from the X_0^1 state as it is far brighter. The X_0^1 is found to have a lifetime of (441 ± 20) ps, indicating that the PhC waveguide is giving this state a modest Purcell factor. The lifetime of the X_0^2 cannot be determined as the two states cannot be separated in this measurement.

The lifetime measurement for the X^- is shown in Figure 5-12. The X^- state has a lifetime of (580 ± 40) ps, which is also Purcell enhanced. The transform limited linewidth of the $X_0^1(X^-)$ state is therefore 1.5 μeV (1.1 μeV). Lifetime measurements are performed on similar X_0 and X^- states of a QD in the nanobeam section of the waveguide to estimate the sponteneous decay rate in the absence of any Purcell effect; the lifetime of the unenhanced X_0 and X^- states are measured to be 750 ps and 1500 ps respectively. We use these measurements to estimate the Purcell factor of the $X_0^1(X^-)$ state to be 2.2(2.6). This measurement is only a rough estimate because we
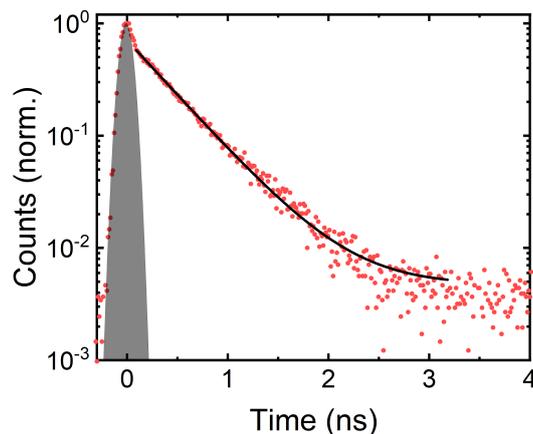
Figure 5-11: Resonant lifetime measurement of the X_0 line. The instrument response is shown in grey. The decay is fit with a single exponential curve with a decay constant of 440ps.
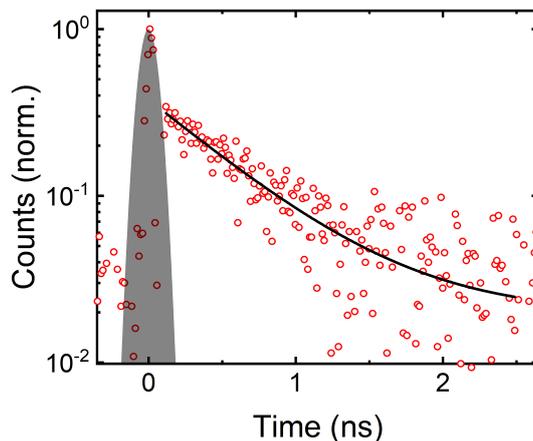

Figure 5-12: Resonant lifetime measurement of the X^- line. The instrument response is shown in grey. The decay is fit with a single exponential curve with a decay constant of 580ps.

only measure the lifetime of one unenhanced QD. Generally a measurement of the QD ensemble lifetime would be performed, however we measured different lifetimes for our QD when exciting resonantly to exciting above band, so a measurement of the ensemble (which requires above band excitation) would not be a good comparison.

After spectral wandering, the largest source of decoherence is pure dephasing. The pure dephasing rate can be probed by performing interferometry on the collected RF photons. Since RF is only emitted when the QD is resonant with the laser, these photons do not have the coherence of the inhomogeneous broadening caused by spectral wandering. These photons show the transform limited properties of the QD, which
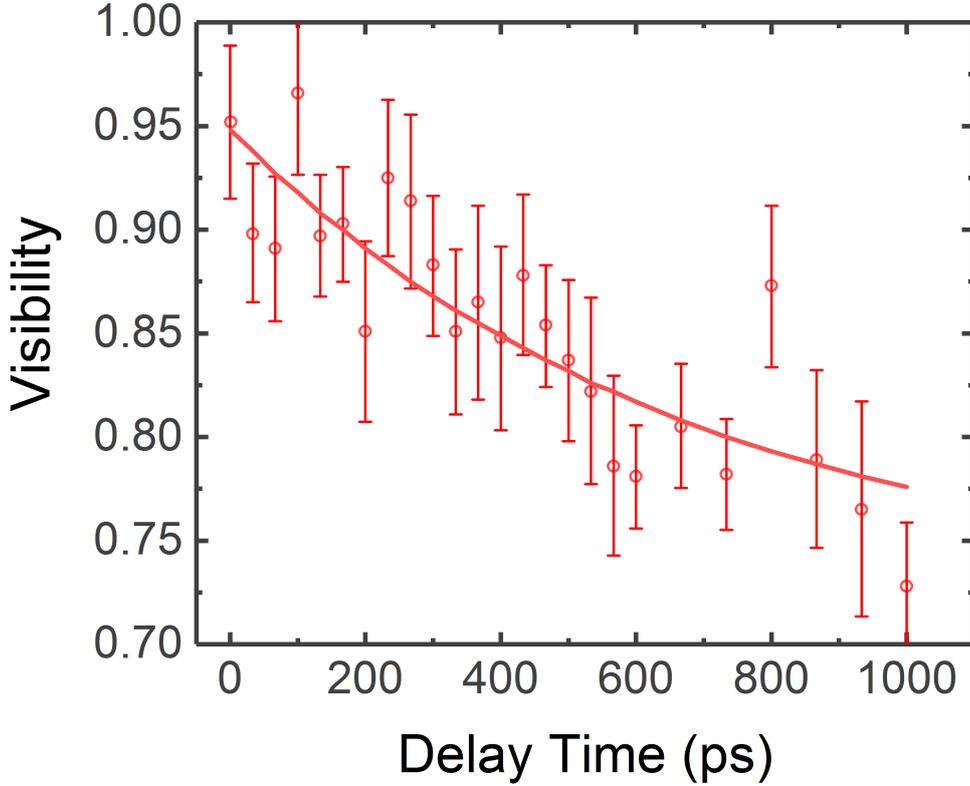
Figure 5-13: $g^{(1)}(t)$ coherence measurement taken using a Michelson interferometer on RF from the X_0 line. The red line is a fit to Equation 5.3.

are determined by the lifetime of the QD and the pure dephasing time only. The coherence time of RF is measured using a Michelson interferometer.

The RF has contributions from RRS and RPL; the relative intensity of the two contributions is described in Equation 2.6. The RRS has the coherence of the excitation laser, which is assumed to be infinite on the scale measured here. The RPL has coherence defined by T_2. We use Equation 2.6 and the coherence of the RPL (Lorentzian distribution) to create a full description of the interference visibility in this measurement, which depends on T_1 and T_2 only. The full equation for visibility is Equation 5.3,

$$V(t) = \left(1 - \frac{T_2}{2T_1}\right) e^{-\frac{t}{T_2}} + \frac{T_2}{2T_1}, \tag{5.3}$$

where t is the time difference in the interferometer, T_1 is the lifetime of the QD and T_2 is the coherence time, as in Equation 2.4.

The results of the Michelson interferometry are shown in Figure 5-13. The coherence consists of an exponential decay from the RPL and a flat contribution from the RRS. From fitting this data we find a coherence time of (670 ± 40) ps for the X_0^1 state. The coherent fraction in this measurement is 0.74 ± 0.05.

From this measurement of the coherence time, the pure dephasing time is calculated using Equation 2.4 to be (2.8 ± 0.7) ns. The pure dephasing time is therefore 5-10 times longer than the measured lifetime, indicating that pure dephasing is unlikely to have a significant effect on the waveguide transmission measurement for this QD. For comparison, the coherence time including the effect of spectral wandering (from the linewidth measurement of 4.8 μeV) is 450 ps.

5.4.2 Resonant transmission and reflection of a QD in a single-mode waveguide

In the following section we present the transmission spectra of the three charge states of QD-A. Initially we study the transmission intensity of single-photons only. The expected result is a reduction in waveguide transmission when each QD state is resonant with the laser. The lowest point of this reduction is dependent on the spectral wandering and coupling efficiency of the QD charge state. In the ideal case the transmission is completely blocked by the interaction with a single QD. In this work, we observe a maximum reduction of 35% in waveguide transmission from a single QD. These measurement is performed by injecting a weak (8 nW) resonant laser into the waveguide and measuring the transmitted intensity. The weak laser inputs 0.06 photons per QD lifetime. This approximates a single-photon input because the probability of the laser injecting two photons within the lifetime of the QD is very low. The QD is modulated using the electric field to observe the effect of the QD. In the following measurements the transmission intensity with the QD on resonance is normalised to the transmission intensity with the QD detuned far from the laser.

All three charge states have a strong effect on waveguide transmission. Transmission spectra at constant bias for the X_0, X^- and X^+ charge states are displayed in Figure 5-14, Figure 5-16 and Figure 5-18 respectively. Large range bias dependences
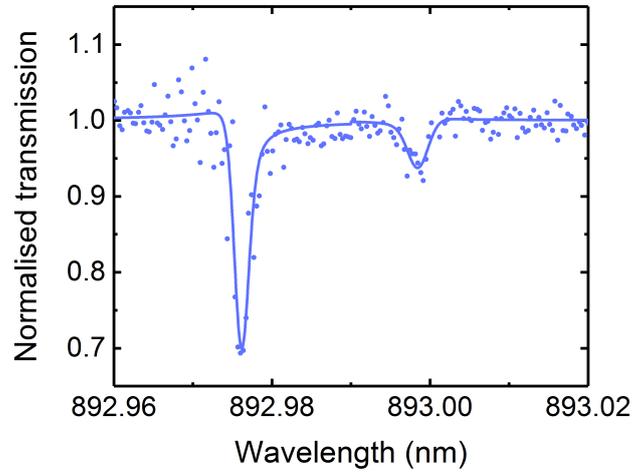
Figure 5-14: Normalised transmission spectrum of the X_0 states at a bias of 6.75 V.
The solid blue line is a theoretical fit to Equation 5.4.
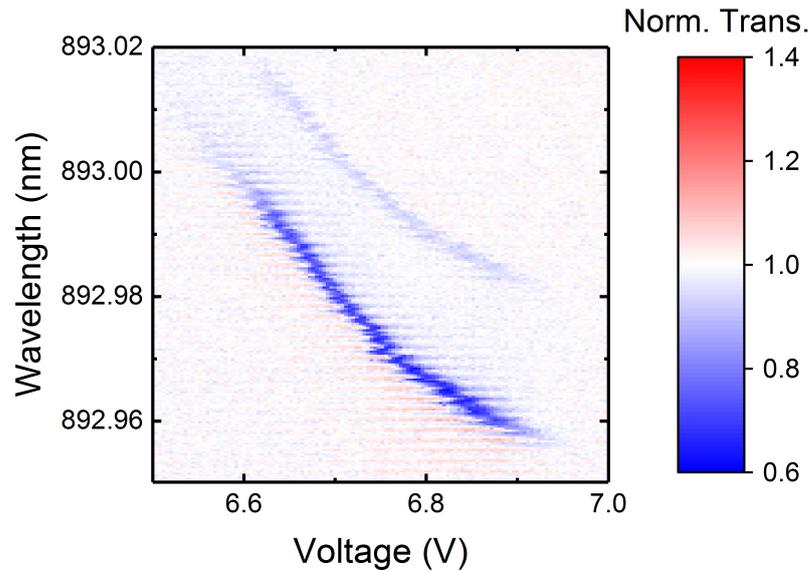
Figure 5-15: Waveguide transmission as a function of laser wavelength and bias look-
ing at the effect of the X_0 states.

of the three states are shown in Figure 5-15(X_0), Figure 5-17(X^-) and Figure 5-19
(X^+). The transmission spectra are fit using the model, allowing explanation of the
different properties of the three states.

The three charge states are active over the same voltage ranges as seen in RF; the
transition energies and tuning ranges of the states are also unchanged. The linewidths
measured in transmission are narrower than those measured in RF for all three states;
this is likely due to the different excitation methods. In transmission measurements

83

the laser is incident on an outcoupler, therefore any fluctuations in temperature or charge environment that the laser causes are spatially separated from the QD. In addition the laser power used to excite the sample is lower in transmission measurements.

A transmission spectrum of the X_0 is shown in Figure 5-14. Two dips in transmission can be seen from the two fine structure states. The higher energy state reduces waveguide transmission by a maximum of 35%, the lower energy state reduces transmission by 5%. This difference is attributed to a lower coupling efficiency, as seen in RF. The FWHM of the two lines at this bias is measured to be $(3.7 \pm 0.2)\mu$eV for the X_0^1 and $(3.3 \pm 0.3)\mu$eV for the X_0^2.

The bias dependence of the transmission of the X_0 is shown in Figure 5-15. The wavelength of the resonance can be tuned over 50 pm using the bias. The transmission minimum from the X_0^1 state is significantly lower than that measured for any of the other states. Therefore more detailed measurements, which are made clearer by a stronger effect, in this chapter will focus on the X_0^1 state.

A transmission spectrum of the X^- is shown in Figure 5-16. This state reduces transmission by up to 18%, the linewidth of this state is $(4.6 \pm 0.5)\mu$eV. The difference in minimum between this state and the X_0^1 is determined to be due to the longer lifetime and larger viariance of spectral wandering; other parameters are found to be similar. Figure 5-17 shows a transmission contour plot of the X^- line. As in RF, the state can be seen to tune over 20 pm and the diode reaches flat band conditions at 895.84 nm.

The transmission of the X^+ is shown in Figure 5-19. As with the RF measurements on this exciton, a weak non-resonant laser is required for this charge state to be active. This exciton is active over a wide range of voltages, and tunes over a 150 pm range. A single spectrum of the X^+ is displayed in Figure 5-19. This state reduces waveguide transmission by up to 15%. The shape of this line is significantly different to that measured for the other two states. We can still extract the QD parameters from fitting, which accounts for this asymmetry. From this we find the linewidth of the X^+ to be $(7.3 \pm 1.8)\mu$eV.

Fitting to this line indicates that difference in transmission is caused by the increased
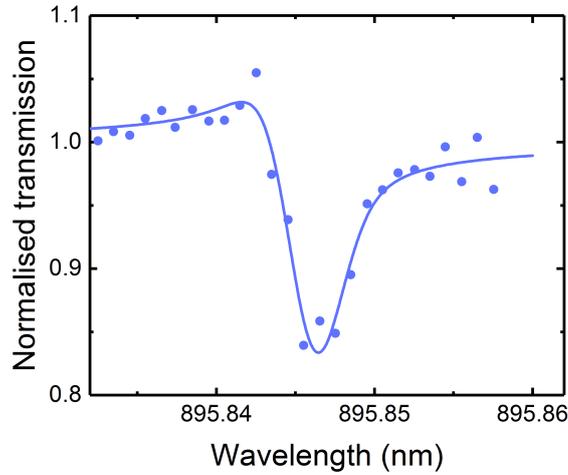
Figure 5-16: Normalised transmission spectrum of the X^- state at a bias of 7.2 V. The solid blue line is a theoretical fit to Equation 5.4.
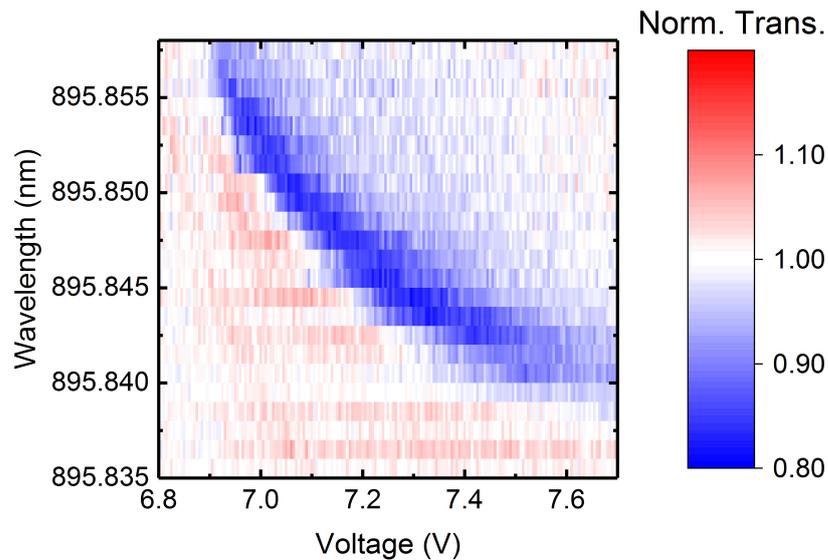

Figure 5-17: Normalised waveguide transmission as a function of laser wavelength and bias showing the X^- line.

rate of spectral wandering for this state. In addition, the dark state probability for this state is significantly higher ($\alpha \simeq 40\%$) than for the other two states ($\alpha < 5\%$). This is another effect of the charge instability of this state, evidenced by the need for a weak repump laser in measurements on this state.

This transition produces an asymmetric line, a characteristic sign of Fano interference. Fano interference in this system arises from the interaction between the resonant QD scatter and the background waveguide transmission. The waveguide transmission
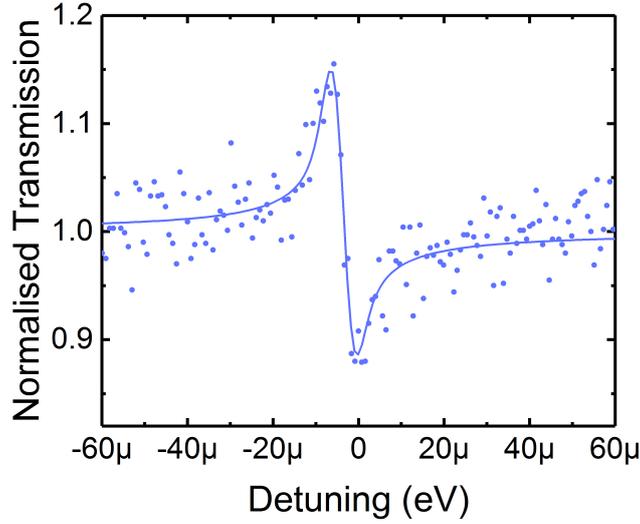
Figure 5-18: Normalised transmission spectrum of the X^+ state. The solid blue line is a theoretical fit to Equation 5.4.
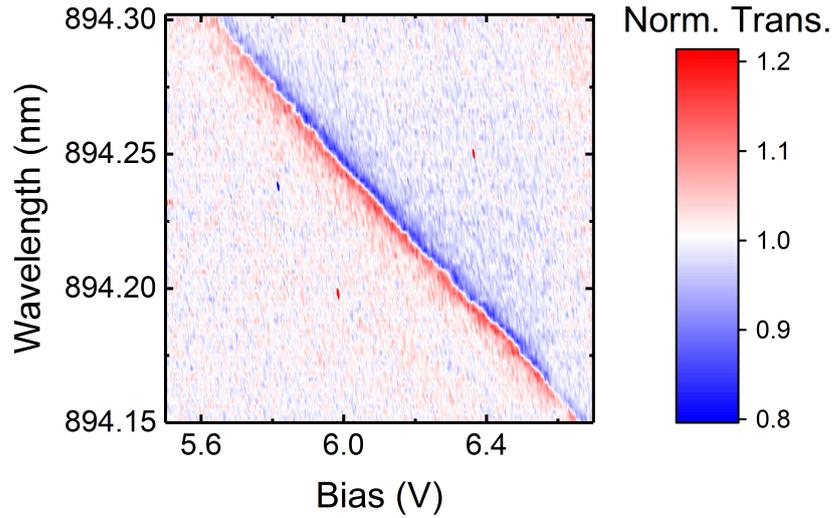
Figure 5-19: Normalised waveguide transmission as a function of laser wavelength and bias showing the X^+ line.

varies with wavelength due to the F-P modes seen in Figure 5-3. It is clear from Figure 5-3 that the background waveguide transmission at the wavelength of the X^+ state is significantly different than for the X_0 and X^+ states. Fano interference in the QD-waveguide system is investigated in more detail in chapter 6. Figure 5-20 shows the bias dependence of the transmission minimum of the X_0^1 state. The charge plateau can be seen between 6.65 and 6.85 V. There is a slight improvement in the visibility as the bias is increased. This appears to be caused by a slight reduction in
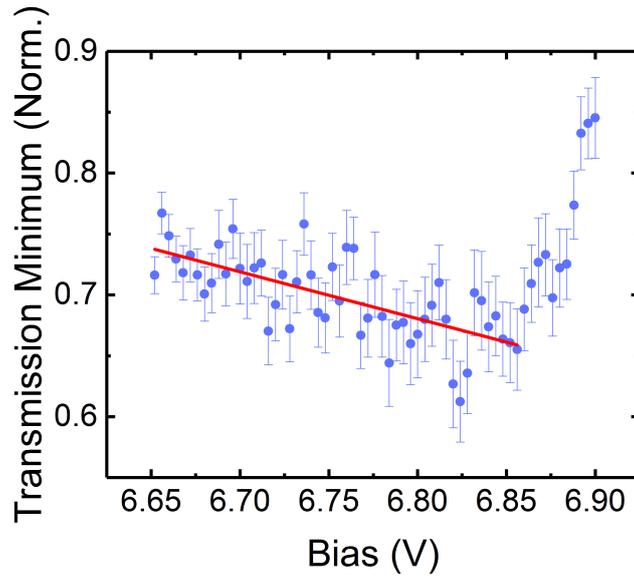
Figure 5-20: Bias dependence of the transmission minimum of the X_0^1 line. The red line is a linear fit over the region 6.65-6.85 V indicating the minimum getting lower as the bias is increased. At 6.85 V the charge state of the QD changes.
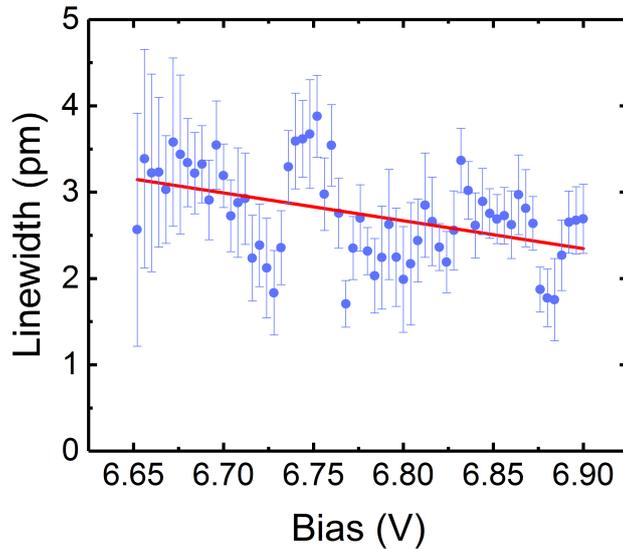
Figure 5-21: Bias dependence of the transmission linewidth of the X_0^1 line. The red line is a linear fit over the region 6.65-6.9 V indicating a reduction in linewidth of the X_0^1 as the bias is increased

the spectral diffusion of the state as the bias is increased. This can be observed in Figure 5-21, which shows the linewidth as a function of voltage. Some oscillation can be seen in the linewidth, however the general trend is downwards - from (3.3 ± 0.2) pm at 6.6 V to (2.4 ± 0.2) pm at 6.9 V.

87

Reflection of a single QD in a waveguide

The scattering of single-photons by the QD causes the reduction in waveguide transmission when the QD is resonant with the input laser. It is important to identify what happens to the light that is not transmitted. Photons that scatter off the QD are reflected and exit the waveguide from the input BGC; we can collect these photons to measure waveguide reflectivity. The increased reflectivity caused by the resonant scattering can also be measured. This reflected signal will consist mainly of single-photons. Antibunching of the reflected photons has not been measured previously in waveguide devices due to the difuculty of the measurement. In the following section we measure the reflected signal and assess whether is it possible to measure antibunching of the reflected photons.

Reflection measurements on this device are limited because it is extremely difficult to separate the signal from scattered laser. The excitation and collection spot need to be aligned onto the same outcoupler; as a result, neither spectral nor spatial filtering can be used to reject the laser scatter. The only filtering that can be used is polarisation. This is achieved by polarising the incoming light at +45 degrees and collecting light at -45 degrees relative to the outcoupler, these crossed-polarisations block light that scatters directly off the sample while allowing light to be injected to and collected from the waveguide. This polarisation rejection is further complicated by the structure of the outcoupler; scatter off this uneven surface doesn't have a smooth Gaussian profile. Therefore, even small movements of the sample surface (e.g. from temperature fluctuations) drastically affect the efficiency of the polarisation rejection. It is possible to study reflection using electrical modulation to identify the effect of the QD. However the laser scatter makes a detailed study of photon statistics (e.g. power dependence) in reflection impossible.

Figure 5-22 shows the bias and wavelength dependence of the reflected signal from the X_0 states. There is a clear resonance at the wavelength of the X_0^1 state measured previously using RF and transmission. In this measurement there is a large amount of laser scatter, it is not possible to maintain the polarisation rejection as the laser

wavelength is tuned. The laser scatter is identified using electrical modulation and is subtracted from the final signal. Interestingly the interference of the signal and the laser scatter creates a similar Fano interference as seen in transmission, although this Fano resonance can be suppressed by better rejecting the laser scatter, as is evident in Figure 5-23.

Figure 5-23 shows a reflection spectrum of the neutral exciton at 892.99 nm, with 10 nW of laser power incident above the objective; the laser scatter is well rejected in this measurement, so no Fano resonance is visible. The spectrum is performed by tuning the exciton energy instead of the laser wavelength; the rejection of laser scatter has a dependence on the laser wavelength. Lines are visible from both FSS, although the X_0^1 state has a much larger reflected intensity. The linewidth of the fit is estimated to be $3.7 \mu eV$. This value is similar to the linewidth measured for the X_0^1 in transmission. A maximum signal-background ratio of 6:1 is obtained for the X_0^1 reflected line, the background in this case is the residual laser scatter.

From this measurement, we determine that an HBT measurement on the reflected signal from this device is possible. If the reflected signal is fully antibunched, then with this signal-background ratio an HBT measured would obtain a $g^{(2)}(0)$ of 0.26.
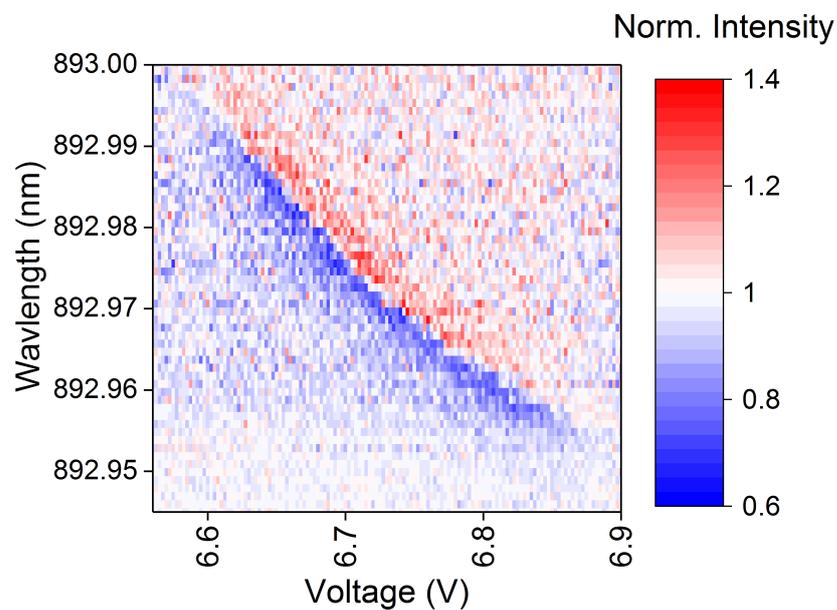
Figure 5-22: Reflection intensity of the X_0^1 state as a function of laser wavelength and bias. The intensity has been normalised to the intensity of laser scatter off the sample.
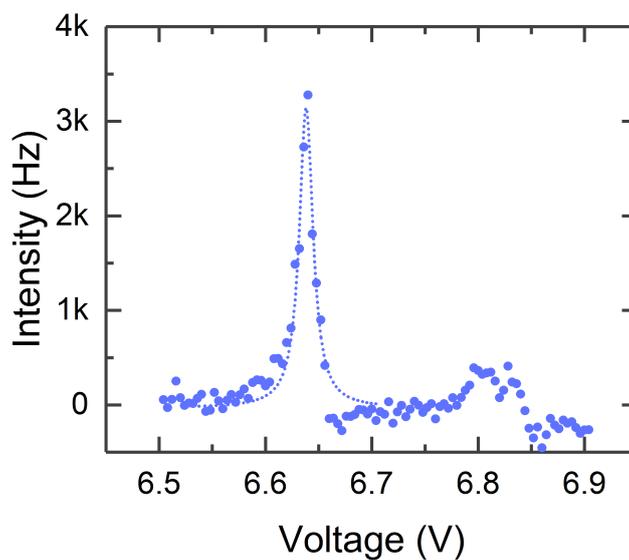

Figure 5-23: Reflection spectrum of the X_0^1 and X_0^2 states as a function of laser wavelength and bias. The blue dotted line is a Lorentzian fit to the X_0^1 state.

5.4.3 Electrical control of waveguide transmission using a single QD

The electrical tuning of the QD allows modulation of both the RF and transmission effect, this is important as it can allow a quantum optical circuit to be reconfigured remotely. An important parameter for modulation is the time response of switching the device on and off. Electrical control should allow for an extremely fast time response as the QD only needs to be tuned out of resonance with the laser, a relatively small disturbance to the system compared to optical switching [43, 133] with changes the charge state of the QD. High frequency control of RF can be used to enable generation of frequency stabilised single-photons [155].

To measure the switching time, the bias applied to the sample is modulated between 6.62 V and 6.55 V at a rate of 20 kHz; this brings the X_0^1 in and out of resonance with the laser. The transmitted photons are detected on an APD and a time-resolved measurement, synchronised to the voltage source, is used to measure the time response of the device. The time resolution of the measurement is 40 ns and the switching time of the voltage source is 30 ns.

 The result of the switching measurement is shown in Figure 5-24. The QD is tuned into resonance at 0 μs, and out of resonance at 50 μs. The switching is extremely fast; the 80:20 time of both tuning in and out of resonance is measured to be 80 ns. A similar switching time is obtained when measuring RF from the QD.

The device can be modulated to 80% of the maximum visibility in a short time, however when tuning into resonance the device doesn't reach 100% visibility immediately. There is a slow voltage response arising because the device tunes the QD near to resonance, but not exactly to the correct energy. This is due to the changing resistance of the diode, which produces some small fluctuation in the applied voltage on timescales of ∼1 μs after switching. These fluctuations do not affect the signal when tuning out of resonance as when out of resonance the signal is not sensitive to small changes in bias. These fluctuations could be mitigated by optimising the diode for a fast voltage response. This would require the active area of the diode to be made smaller, for example by using a micro-diode contacting scheme [79].
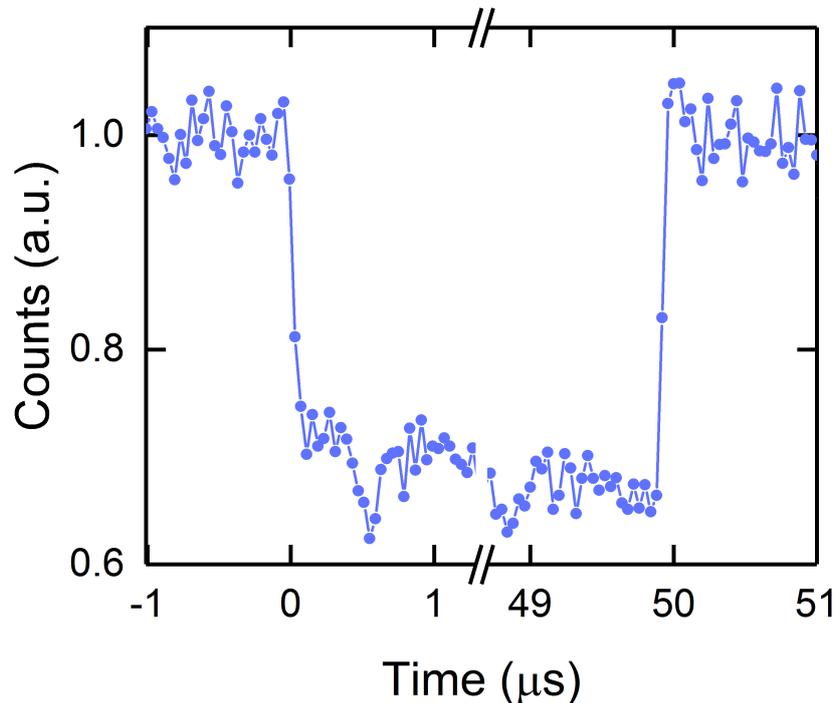
Figure 5-24: Switching of the waveguide transmission of the X_0^1 line. The transmission effect is switched on at 0 μs and off at 50 μs.

The device can be modulated extremely quickly, a switching time of 80 ns means that the device can be modulated at up to 10 MHz. This compares very favourably to other switching methods, such as optical switching (μs timescale [43, 133]). Our measured result may still be limited by the switching time of the voltage source (30 ns) and the resolution of the measurement (40 ns). In addition, the device is not designed for fast switching, GHz modulation frequencies could be achieved using an optimised micro-diode [79].

5.4.4 Non-linear behaviour of a QD in a single-mode waveguide

The nonlinear photon-QD interaction is evident in the power dependence of the transmission effect. The quantum nature of this nonlinearity is confirmed using photon statistics measurements on the transmitted and reflected laser fields. The photon statistics measurements allow the transmission of single-photons to be compared to
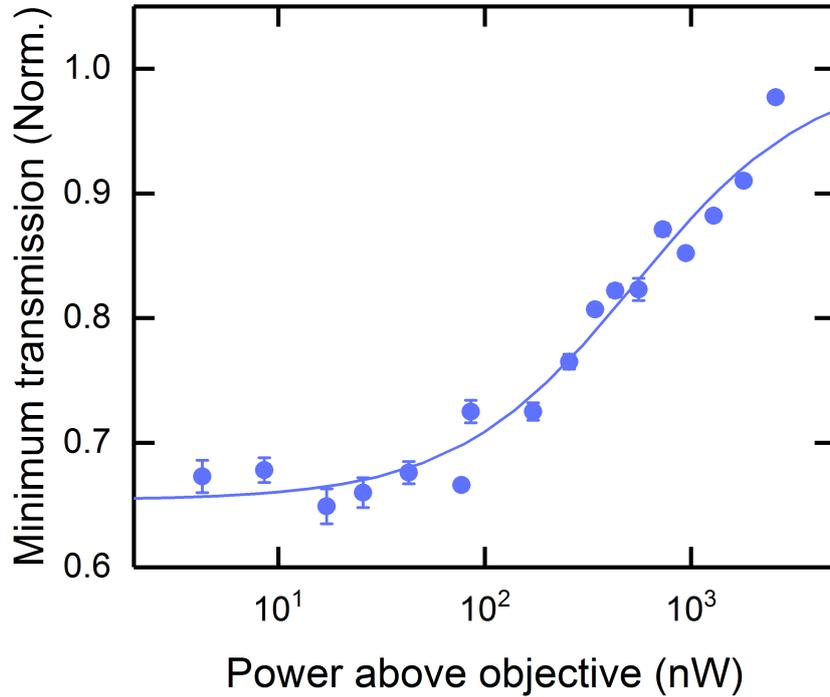
Figure 5-25: Power dependence of the transmission minimum of the X_0^1 line. Solid line is a fit to Equation 5.9, the critical power is found to be 530nW.

the transmission of two-photon states. Figure 5-25 shows the power dependence of the transmission minimum of the X_0^1. For this measurement transmission spectra are recorded at different powers and the minimum is determined by fitting the spectra. The nonlinear behaviour is evident in this measurement, as the waveguide transmission reduces with increasing power as predicted by Equation 5.9. The fit to Equation 5.9 gives a critical power, P_C of 530 nW.

The critical power of 530 nW is far higher than predicted from Equation 5.10. The most likely cause of this is that incident light is very poorly coupled into the waveguide, meaning that most of the incident light does not reach the QD. Using measured values for $\beta = 0.9$, $\Gamma = 2.27\ ns^{-1}$, $\gamma_0 = 0.35\ ns^{-1}$ and $\lambda_0 = 893$ nm the expected critical power for this QD is estimated at ~ 2 nW. Assuming that this is the correct critical power in the waveguide, we calculate that 0.4% of incident light is coupling into the waveguide.

Figure 5-26 and Figure 5-27 show $g^{(2)}(t)$ measurements for transmitted and reflected laser fields respectively with the QD on resonance. The input laser is coherent, there-

fore the input field has $g^{(2)}(0) = 1$. Preferential transmission of two-photons creates bunching in the transmitted field. Single-photons are reflected by the QD, therefore the reflected field is anti-bunched.

A $g^{(2)}(0)$ of 1.15 is measured for the transmitted field; this is limited by the visibility of the transmission dip and depends largely on the QD parameters. A $g^{(2)}(0)$ of 0.4 is measured for the reflected field, displaying clear antibunching at zero time. The minimum of $g^{(2)}(0)$ is limited by the collection of laser scatter which cannot be eliminated (the signal-background ratio is 6:1 in this case).

Figure 5-28 shows the bunching as a function of X_0^1-laser detuning. The detuning is controlled by electrically tuning the QD relative to the fixed laser wavelength. $g^{(2)}(0)$ is maximised at zero detuning. $g^{(2)}(0)$ approaches unity as the detuning is increased, as expected for a coherent laser source. Controlling the detuning allows for switching of the nonlinear effect and control of the strength of the effect.
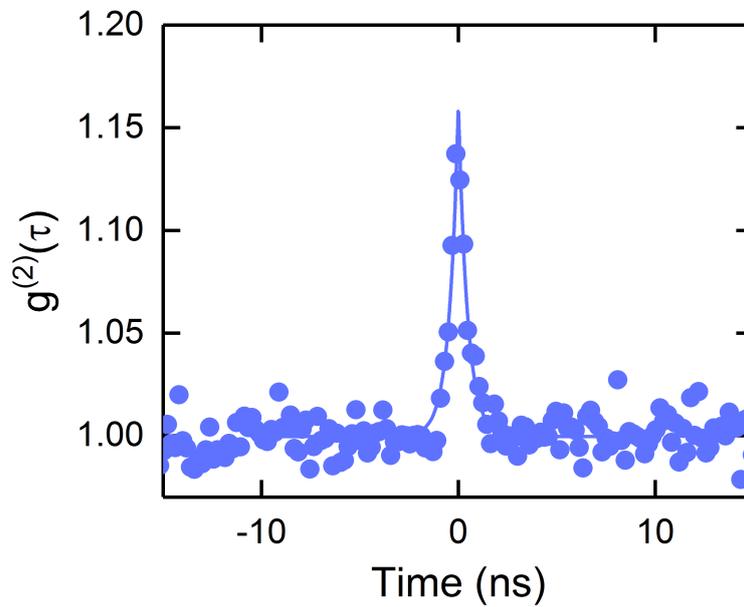
Figure 5-26: Photon statistics of the transmitted light with the input laser on resonance with the X_0^1 line. Bunching of 1.15 is seen at $\tau=0$
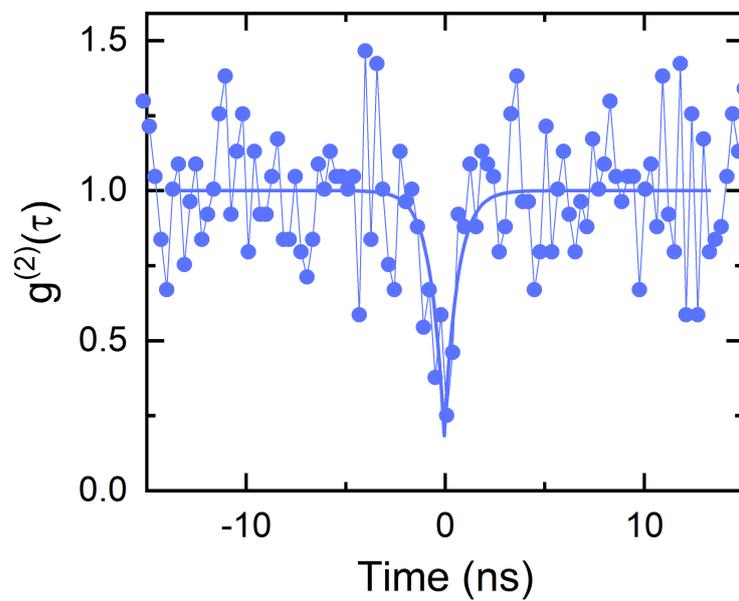
Figure 5-27: Photon statistics of the reflected light with the input laser on resonance with the X_0^1 line. Antibunching is seen at $\tau=0$.
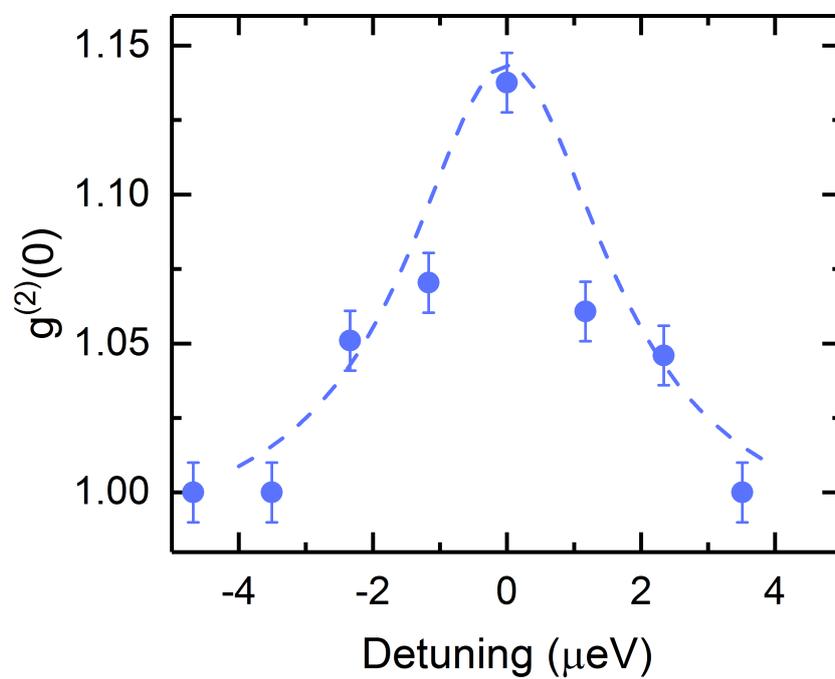
Figure 5-28: $g^{(2)}(0)$ of the transmitted light as a function of X_0^1-laser detuning. The degree of bunching can be controlled.

5.4.5   Observation of a strong waveguide-coupled non-linearity
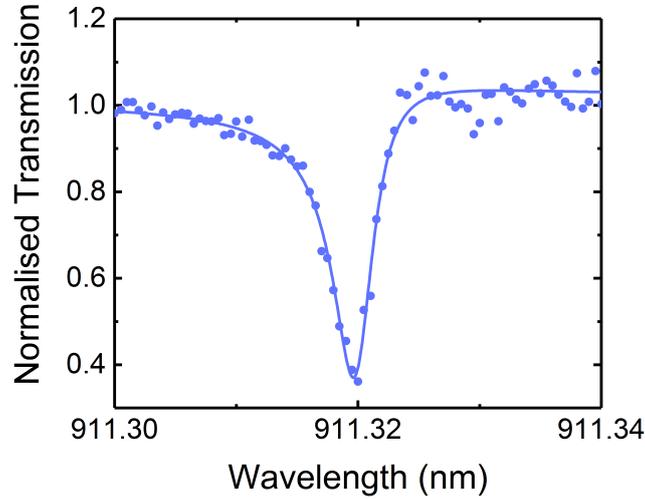
Figure 5-29: Transmission spectrum from QD-B. The solid blue line is a theoretical fit to Equation 5.4.
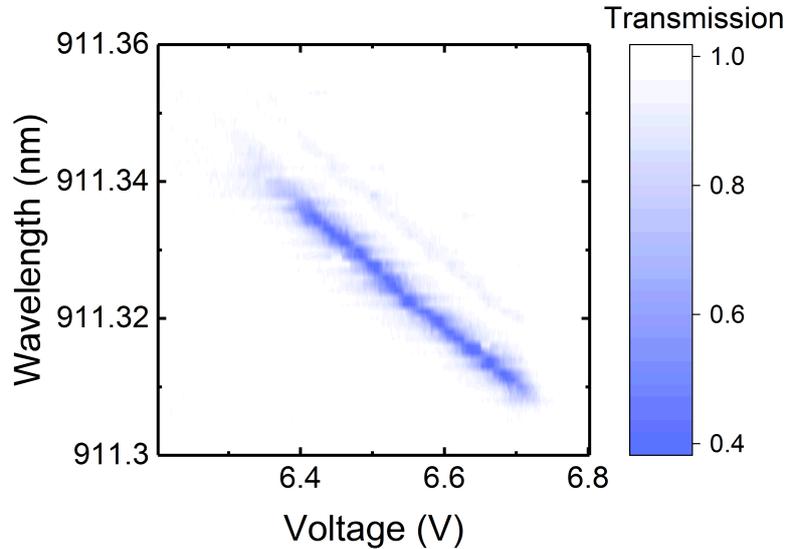
Figure 5-30: Normalised waveguide transmission as a function of laser wavelength and bias showing the X_0 line for QD-B.

After performing these measurements, we are able to improve on the results by locating QDs with better properties. These QDs are labelled QD-B and QD-C from here on. The QD studied in section 5.4 is referred to as QD-A here. The properties of these QDs are investigated further in chapter 6, here we summarise the properties of QD-B to demonstrate the improvement in device performance.

These high-quality QDs were found after a change of the QD characterisation method. Rather than characterising QDs in PL and RF, the transmission of the waveguide is probed directly. The electrical control allows a full waveguide to be tested for high quality QDs in one scan, whereas PL and RF scans only probe a small area of the device. Measuring directly in transmission also means that the QDs with desirable properties are immediately more visible, whereas in PL and RF many complex measurements are required to determine how the viability of a QD for transmission measurements.

Using this method we are able to find QDs closer to the band edge of the waveguide, which have larger Purcell enhancements. These were previously rejected after PL characterisation because the linewidths are broad. Measuring directly in transmission shows that the broad linewidth is caused by a shorter lifetime rather than spectral wandering. Figure 5-29 shows a transmission spectrum from QD-B. This QD state reduces waveguide transmission by up to 65%. Further investigation finds a lifetime of (150 ± 3) ps and a FWHM of (5.6 ± 0.3) μeV for this line, representing a broadened linewidth only 1.4 times larger than the transform limited linewidth. Figure 5-31 and Figure 5-32 show $g^{(2)}(t)$ measurements on QD-B, the maximum $g^{(2)}(0)$ observed for this state is 2.2. This result is a 10x improvement on the result from the X_0^1 state of QD-A.

This result is not only notable for being a significant improvement on previous results using QDs in waveguides, but it is also better than any result for waveguide based devices currently in literature. This demonstrates the potential of waveguide-QED using InAs QDs, as in the last two years the maximum transmission visibility in QD devices has improved from 8% [43] to 75%. This visibility needs to be further improved for the effect to be useful in quantum-optical circuits; to achieve this improvement the rate of spectral wandering needs to be reduced further. This work has shown that other effects that limit the visibility in QD based systems – namely blinking and pure dephasing – do not have a significant effect in this device.

The increased visibility of the transmission effect allows the power dependence of the photon statistics to be measured. The power dependence of the bunching of the transmitted autocorrelation function is shown in Figure 5-33. In this measurement,
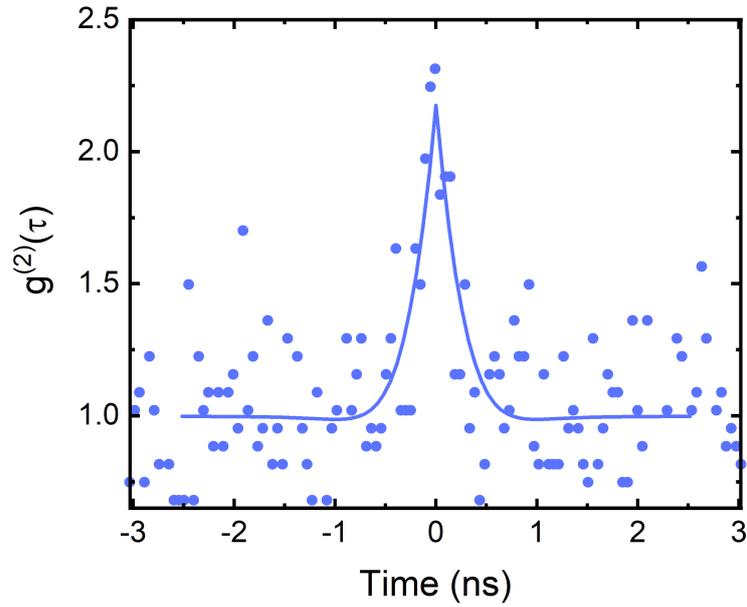
Figure 5-31: Photon statistics of the transmitted light with the laser resonant with the X_0^1 of QD-B. A $g^{(2)}(0)$ of 2.2 is measured.

the autocorrelation function is taken at the transmission minimum for increasing input powers. The peak bunching is reduced as the power is increased. This reduction in bunching in the autocorrelation function occurs at the same power as the increase in transmission minimum.
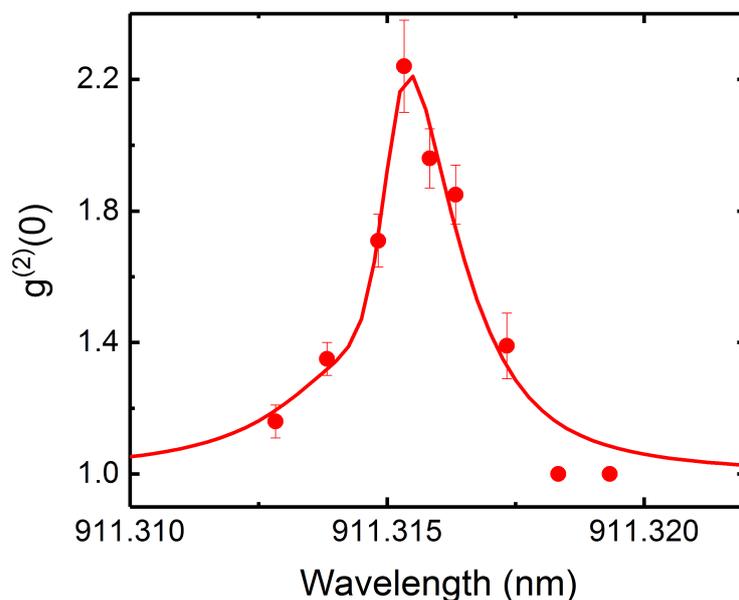
Figure 5-32: $g^{(2)}(0)$ of the transmitted light as a function of QD-laser detuning for QD-B. The solid line is a theoretical estimate of the autocorrelation function using parameters extracted from the transmission spectrum of this QD.
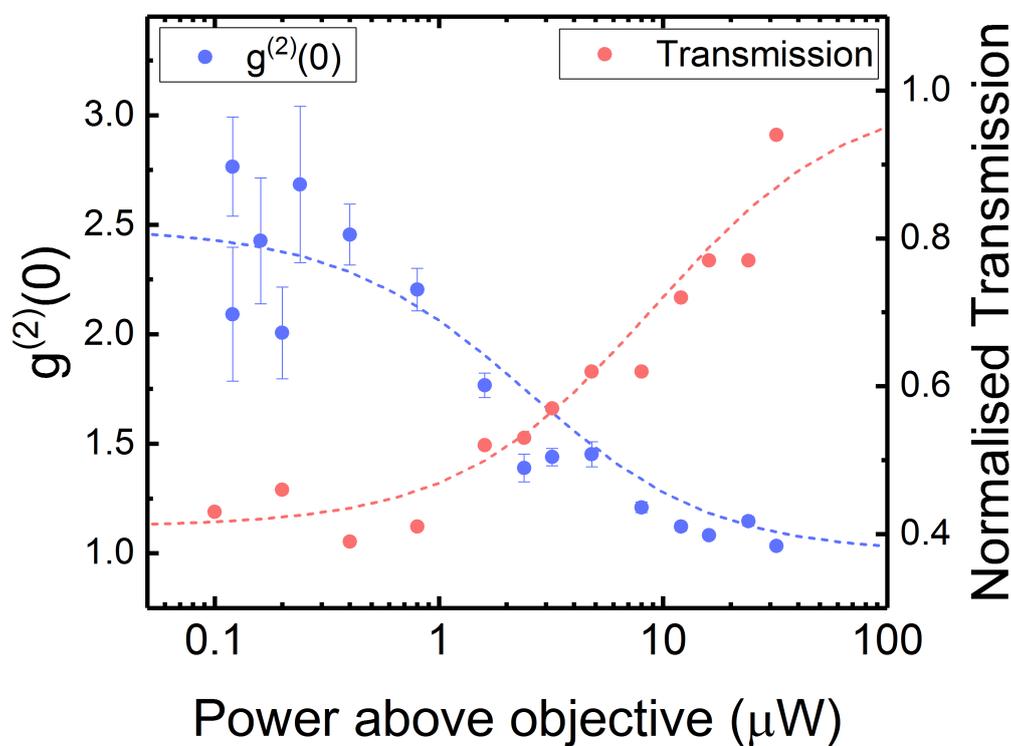
Figure 5-33: Power dependence of the transmission minimum (red) and the corresponding autocorrelation maximum (blue) for QD-A. The red dashed line is a fit to Equation 5.9. The blue dashed line is a guide to the eye.

5.5 Modelling waveguide transmission of a single QD

The system is understood using the input-output formalism outlined in section 2.4. This formalism allows the intensities of single and two-photon transmission and reflection to be calculated. In section 2.4 the behaviour of an ideal TLS is considered. In order to fit the theoretical data in this chapter is it required that we account for the real-world properties of the QD. These additional effects are spectral wandering and dark state probability of the QD. In addition, we model the power dependence of the system.

The theory in this section is based on the work done by Dr. David Hurst, seen in the supplementary information of [165].

Spectral Wandering

Spectral wandering is a random fluctuation in energy of the QD transition over time, it is caused by changes in the charge and spin environment of the QD. The fluctuations create a broadening of the line. All lines measured in this chapter show a Lorentzian broadening from spectral wandering. In order to model the effect of spectral wandering, the transmission function is convoluted with a Lorentzian line, characterised by the FWHM of the wandering. To account for spectral wandering in the autocorrelation function the one and two-photon components are convoluted separately, this is required to account for the wandering of both the autocorrelation function and the transmission intensity.

After convolution with a Lorentzian, the time-averaged transmission and autocorrelation function are given by Equation 5.4 and Equation 5.5.

$$T_{av}(\delta) = \frac{1}{\pi} \int L(x) T_1(\delta + x) dx, \tag{5.4}$$

$$g_{av}^{(2)}(0,\delta) = \frac{1}{\pi} \int L(x) g^{(2)}(0, \delta + x) dx, \tag{5.5}$$

where $T_1(\delta)$ is the waveguide transmission at detuning δ, and $g^{(2)}(0,\delta)$ is the auto-correlation function of the transmitted light at time t=0 and detuning δ. L(x) is the Lorentzian distribution:

$$L(x) = \frac{1}{\pi} \frac{\frac{1}{2}\sigma}{x^2 + (\frac{1}{2}\sigma)^2}, \tag{5.6}$$

where σ is the FWHM of the distribution. Figure 5-34 shows the effect of spectral
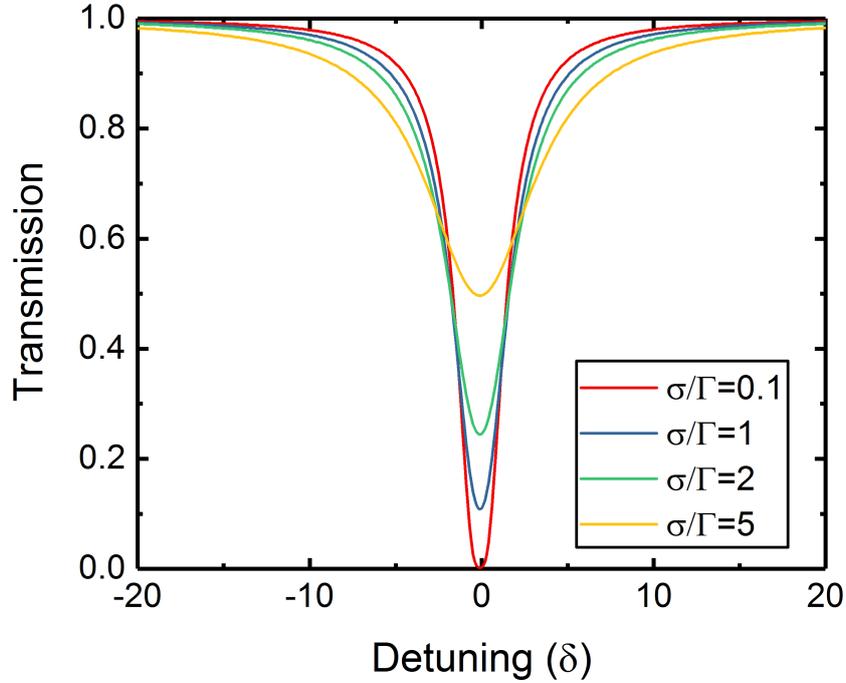
Figure 5-34: Transmission spectra for different rates of spectral wandering, defined relative to the spontaneous decay rate of the QD, Γ. The minimum and width of the transmission dip depends on the ratio of the variance of spectral wandering to decay rate.

wandering on the transmission spectrum of a QD. Spectral wandering reduces the effect of the QD, as the QD is not always resonant with the incoming photon. Increasing the spectral wandering broadens the line, and increases the transmission at $\delta = 0$.

Blinking

It is possible for the QD to switch from the desired state to another charge or spin state. The other states will have different transition energies and can be considered dark states for the purposes of the experiment - they will not interact with the incoming light. This phenomenon is known as 'blinking'. The transmission and auto-correlation function of the system when the QD is in a dark state are both unity. The effect of blinking on transmission and autocorrelation can be modelled as a weighted sum of the bright and dark state interactions

$$T_{blink}(\delta) = (1 - \alpha)T(\delta) + \alpha, \tag{5.7}$$

$$g^{(2)}_{blink}(0, \delta) = (1 - \alpha)g^{(2)}(0, \delta) + \alpha, \tag{5.8}$$

Where α is the fraction of time when the QD is in a dark state.

Power Dependence

The equations described above apply for a low-power coherent input state only, in this case we can assume only one photon is incident within the lifetime of the QD. Increasing the power beyond this level will reduce the effect of the QD on waveguide transmission. The power dependence is accounted for in the S_Z operator [43]. The input power is compared to a critical power. The power dependence of the transmission minimum is given by:

$$T_1(P) = 1 - \frac{T(0)}{1 + \frac{P}{P_C}}, \tag{5.9}$$

Where T(0) is the transmission minimum at low power, and the critical power P_C is related to the number of photons incident with the lifetime of the QD by Equa-

tion 5.10.

$$P_C = \frac{\Gamma h c}{\lambda} \left(\frac{1 + 2\beta\gamma_0/\Gamma}{4\beta^2} \right), \tag{5.10}$$

where γ_0 is the pure dephasing rate of the emitter.

5.6 Conclusion

We have demonstrated electrical control of the strong on-chip non-linearity arising from the interaction between a single QD and a single-mode waveguide. A maximum laser extinction of 75% is seen, and a bunching of up to 2.5 is generated. The operating wavelength of this effect is tuneable by up to 0.15 nm, and is switchable at frequencies up to 10 MHz.

The strength of the non-linearity depends on reducing the effects of dephasing on the QD. A Purcell effect mitigates these effects, particularly spectral wandering. We give the QD a Purcell factor of 6 by operating in the slow light region of a PhC waveguide. However the strength of the effect is still limited by spectral wandering.

Measurements on different charge states of the same QD reveal that the electrical control stabilises two of the available charge states. The charge state which is not stabilised shows increased spectral wandering and a high dark state probability, two unfavourable properties for devices utilising deterministic light-matter interactions. Use of a 'repump' laser to stabilise the charge state does not recover the properties seen in the other two states.

Similar work in this field has demonstrated control of the waveguide transmission by controlling the spin state of the QD [77, 160]. However, this requires a chirally coupled QD, which is not obtainable in a standard PhC waveguide. There is potential to have both a chirally coupled QD, for spin control, and a Purcell factor, for greater visibility, by using specially designed PhC waveguides [111, 112].

The potential of integrated nano-optics is in the ability to connect multiple devices to make quantum networks. The scalability of these devices requires multiple devices containing different QDs to operate at the same wavelength. This is difficult because

lines from different QDs have vastly different wavelengths, while the QD lines themselves are extremely narrow. The electrical control in this sample allows 0.1 nm of tuning, more than 10x the optical linewidth of the QDs. The tuning range can be improved, by incorporating AlGaAs barriers into the diode membrane, which gives a tuning range of 5nm. The wavelengths of different QDs could be made more homogenous by pre-selecting QDs with similar wavelengths and fabricating devices around them using various registration techniques [161–164].

This page intentionally left blank

6 — Using Fano interference to control photon statistics on-chip

6.1 Introduction

The generation of non-classical states of light is a fundamental requirement for quantum optical devices. For instance, a single-photon input is necessary for linear optical quantum computation schemes [22, 27], while N00N states can enable superresolving phase measurements [13, 14]. Two-level systems are a proven resource for generating non-classical light. Quantum dots have been shown to generate single-photon [14, 59] and two-photon states [137], as well as entangled photonic states [41, 43, 136, 137].

A different approach to creating non-classical light is to manipulate a coherent input state such that it becomes either bunched or antibunched. A coherent state can be considered as a weighted sum of different number states. Number state filtering, in which the weight of individual number states is controlled, converts the classical input into a quantum output state.

Number filters based on quantum interference have been shown to produce tuneable photon statistics, with tuning achieved by changing the detuning between the input coherent state and the resonance of the quantum emitter. Number filters have been demonstrated using QDs in several different systems. In strongly-coupled QD-cavity systems [62–65] first- or second-order maniforlds of the Jaynes-Cummings ladder are selectively excited, creating a photon tunnelling and photon blockade effect. In weakly-coupled QD-cavity systems destructive interference between two excitation pathways [66] enables the 'unconventional' photon blockade [66–68], and quantum interference between RF from a QD in a cavity and photons reflected directly by the

cavity can also be used to tune photon statistics [61].

A single QD in a waveguide has been demonstrated to function as a number-state filter, removing single photons from a coherent input to create bunched light [43,151, 165]. However this effect alone only allows the creation of bunched light; it does not enable tuning of the photon statstics and it does not allow the creation of antibunched light. In this work, Fano interference is used to enable antibunching of the transmitted field. Fano interference arises when a discrete localised transition is coupled a background continuum of states [121,124]. Fano interference is widely observed in photonics and has been observed previously in QD-waveguide systems, caused by interference of the QD with standing Fabry-Pérot (F-P) modes in the waveguide [43,110]. Fano interference is characterised by an asymmetric absorption line; caused by constructive and destructive interference of the light scattered by a resonant emitter and a background continuum [121]. Fano interference has been theoretically shown to enable tuneable number-state filtering in waveguide QED [120,166,167].

In this work we demonstrate a quantum optical filter which can generate either bunched or antibunched light from a coherent input in a waveguide device. The device uses a single QD exhibiting Fano interference. A coherent single mode laser is injected into the waveguide and Fano interference is observed in transmission. We show that the transmitted photon statistics of the output state are bunched when resonant with the Fano minimum and antibunched when resonant with the Fano maximum. Electrical control of the QD energy allows tuning of the detuning, enabling local tuning of the photon statistics. Electrical tuning of the emitter energy allows tuning of the photon statistics without any change to the output photon energy. Importantly, this device is waveguide-coupled, allowing the device to be included in a larger photonic circuit. Modelling of the system reveals that the generation of a two-photon bound state is required to observe number state filtering. Furthermore, antibunching in this system is achieved via destructive interference of the two-photon bound states and two-photon product states, which becomes possible due to the Fano resonance.

6.2 Theoretical model of Fano interference in a 1D waveguide system

In this section, we describe the effect of Fano interference on the 1D-atom model. We describe how the transmission spectrum of the model is modified by Fano interference. We introduce the phase parameter, ϕ which characterises the Fano interference of a QD. We do not yet consider the autocorrelation function of the transmitted light. Detailed discussion of the autocorrelation function is undertaken in section 6.5, after the experimental results are presented.

The theory used in this chapter was developed by Dr. Ivan Iorsh, and derivations of the equations can be found in the supplementary information of [168].

Descriptions of the transmission of a 1D atom system in the abscence of Fano
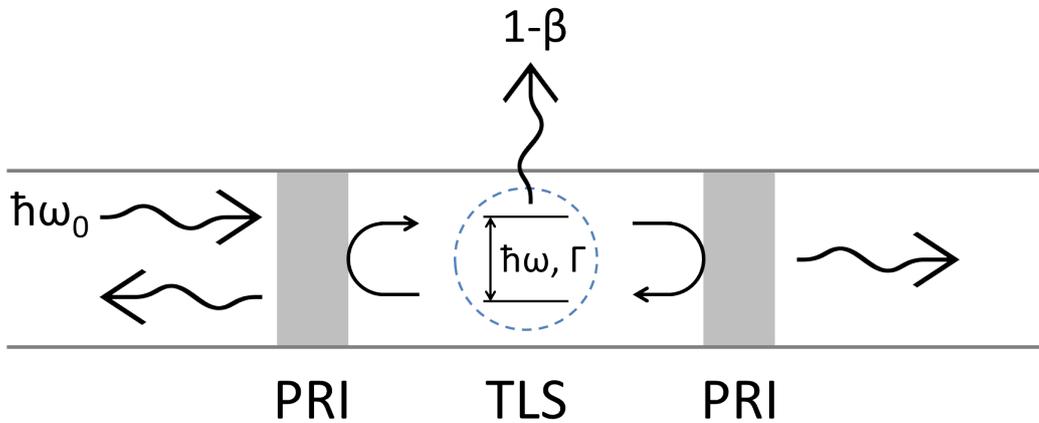
Figure 6-1: System schematic. The system is similar to that presented in Figure 2-6. $\hbar\omega_0$ is the energy of the incoming photons, $\hbar\omega$ is the transition energy of the QD, Γ is the decay rate of the QD and β is the coupling efficiency between the QD and the waveguide. Partially reflective interfaces (PRI) create standing Fabry-Pérot modes in the waveguide; the effect of these modes is described by the scattering matrix $\mathbf{C}$ [120], defined in Figure 6.1.

interference have been introduced in section 2.4, the parameters introduced in section 2.4 are also used here to describe the system. A schematic of the device is shown in Figure 6-1. In this system F-P modes are created by reflections off interfaces in

the waveguide; these F-P modes modulate the waveguide transmission. The effect of this modulation is described by the non-resonant scattering matrix $\mathbf{C}$. The scattering matrix [120] is:

$$\mathbf{C} = \begin{bmatrix} t_0 & ir_0 \\ ir_0 & t_0 \end{bmatrix},$$ (6.1)

where t_0 is the transmission amplitude of the structure in the absence of the QD, and $r_0 = \sqrt{1 - t_0^2}$ is the reflection amplitude of the structure in the absence of the QD. In the absence of F-P modes $t_0 = 1$ and $r_0 = 0$.

Modulation of the background waveguide transmission enables Fano interference between the emitter and the waveguide mode. The strength of Fano interference is represented using a new parameter, ϕ, which takes the form of a phase shift.

$$\phi = tan^{-1}\left(\frac{r_0}{t_0}\right),$$ (6.2)

This parameter depends on the waveguide transmission amplitude at the QD wavelength. QDs with different resonant energies will experience different values of ϕ. For a QD at the peak of a F-P mode, $t_0 = 1$ and consequently $\phi = 0$. For a QD at the minimum of an ideal F-P mode, $t_0 = 0$ and $\phi = 0.5\pi$.

The effect of the modulation on waveguide transmission is modelled using the method presented in Xu et al. [120]. The transmission of the waveguide is then given by Equation 6.3.

$$T_1(\delta) = |t_1(\delta)|^2 = \left|cos(\phi) - \frac{e^{i\phi}\beta}{1 - i\delta}\right|^2,$$ (6.3)

where $\delta = (\omega - \omega_0)/\Gamma$ as in section 2.4. If ϕ is set to 0, Equation 6.3 is identical to Equation 2.10, describing waveguide transmission in the absence of Fano interference. ϕ can be varied between $-\pi/2$ and $\pi/2$ to produce a complete description of the system, however the positive and negative phases produce symmetric results. Therefore in describing the system we only look at the range $0 < \phi < \pi/2$.

Transmission spectra for QDs with different values of ϕ are shown in Figure 6-2,

showing the different lineshapes that the QD can exhibit in transmission. At $\phi = 0$
the effect of Fano interference is minimal and the transmission spectrum shows a
Lorentzian dip. At $\phi = 0.45\pi$, the QD produces an anti-Lorentzian peak. For an
intermediate value ($\phi = 0.3\pi$) an asymmetric lineshape is expected, this is a key
characteristic of Fano interference.

In addition to the effect of Fano interference, the effects of blinking and spectral wan-
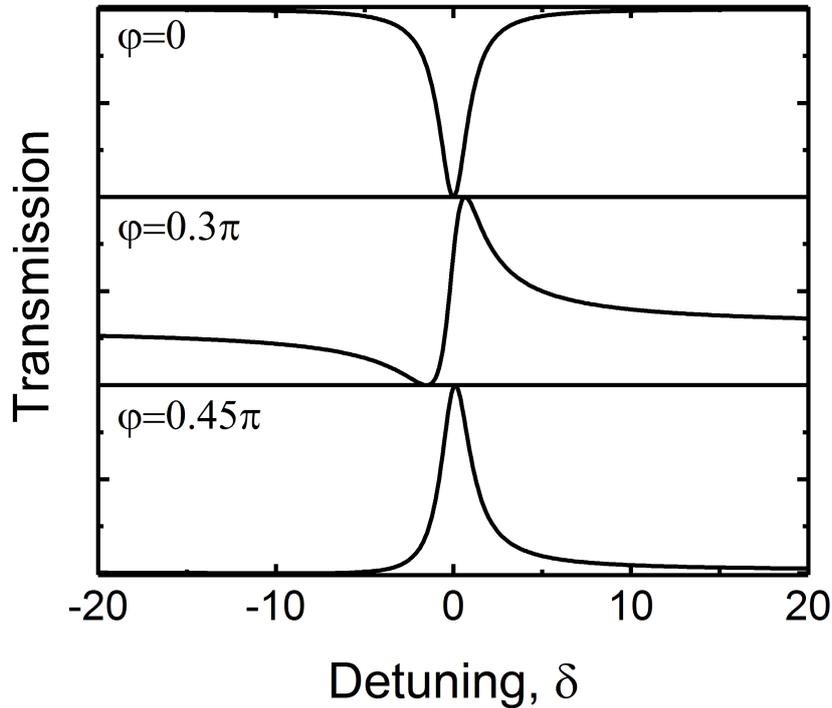
Figure 6-2: Transmission spectra of a QD for different values of ϕ. Different lineshapes
are predicted depending on the detuning of the QD from maximum of the F-P mode.
(a) At $\phi = 0$ the QD causes a Lorentzian dip (b) At $\phi = 0.3\pi$ the QD creates an
asymmetric line characteristic of Fano interference (c) At $\phi = 0.45\pi$ the QD resonance
causes a quasi-Lorentzian peak

dering are accounted for using the methods introduced in section 5.5. The resulting
equation is used to fit the transmission data measured in later sections.

6.3   Device Characterisation

The device used in this work is of the same design as that described in section 5.2.
In these devices, reflections off the outcouplers at either end of the waveguide create

standing F-P modes, enabling Fano interference. In order to observe the effects of Fano interference on waveguide transmission, a QD is required which is detuned from the peak of a F-P mode. An SEM image of a typical device is shown in Figure 6-3. A QD is coupled to a PhC waveguide, enabling a high coupling efficiency to the waveguide and a reduced lifetime via the slow-light effect. This maximises the effect of the QD on waveguide transmission, allowing the detailed photon-statistics measurements performed in this chapter.

The waveguide transmission is characterised using high-power photoluminescence
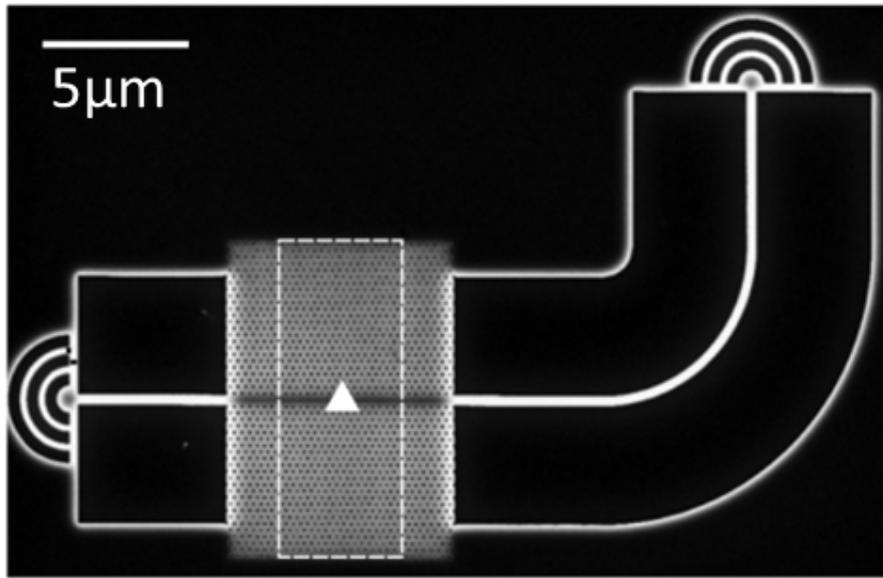
Figure 6-3: SEM image of a full waveguide device. The white dashed box indicates the slow light region of the photonic crystal waveguide. The triangle shows the rough location of the QD studied.

of the ensemble of QDs. The ensemble in one outcoupler of the device is excited and the emission is measured from the other outcoupler. The resulting spectrum is shown in Figure 6-4. The band edge of the waveguide is visible at ∼916 nm, at longer wavelengths the transmission of the waveguide is very low. Oscillations in transmission efficiency are visible for wavelengths shorter than 916 nm, these oscillations arise because of Fabry-Pérot modes in the waveguide.

The spectral position of the QD - 915.05 nm - is marked with an arrow. The QD is very close to the band edge of the device, and experiences a large Purcell enhancement from the slow-light effect of the PhC waveguide. The QD is detuned from the

maximum of the F-P mode. We estimate the waveguide transmission amplitude, t_0 at the QD wavelength by comparing the transmission intensity at 915.05 nm to the maximum transmission intensity of the adjacent Fabry-Pérot mode. This gives a value of $t_0 = 0.55$, this corresponds to a value of $\phi = 0.44\pi$ for the phase parameter. This phase may be overestimated due to the proximity of the band edge. From fitting to transmission spectra for this QD (Figure 6-7), a value of $\phi = 0.3\pi$ is measured. Theoretical modelling (Figure 6-10) predicts that either of these values for ϕ will enable the generation of antibunching in the transmitted field.

The lifetime and linewidth of the QD are measured using RF measurements, this
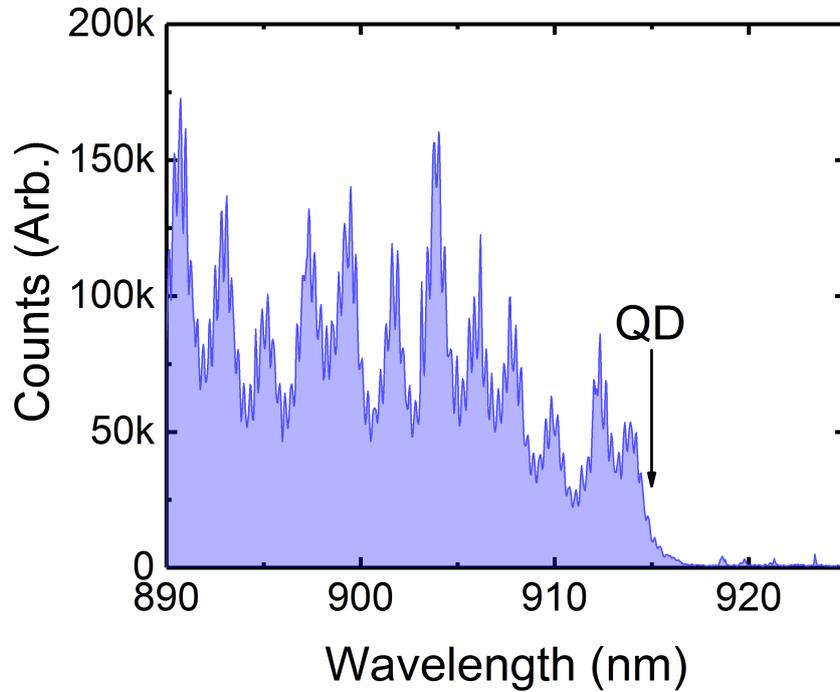
Figure 6-4: High power PL measurement of Device A, showing the F-P modes in the waveguide. The spectral position of the QD is marked with an arrow. The QD is very close to the band edge, so a large Purcell factor is expected. The QD is displaced from the nearest F-P mode peak by ~ 1nm.

reduces the number of free parameters in the model when fitting data later in the chapter. An RF spectrum of the QD is shown in Figure 6-5. The measured linewidth of the RF line is (12.6 ± 0.2) μeV. A lifetime measurement of the QD is shown in Figure 6-6. The lifetime of the exciton is measured to be (150 ± 30) ps, corresponding to a transform limited linewidth of (5.1 ± 1.0) μeV.
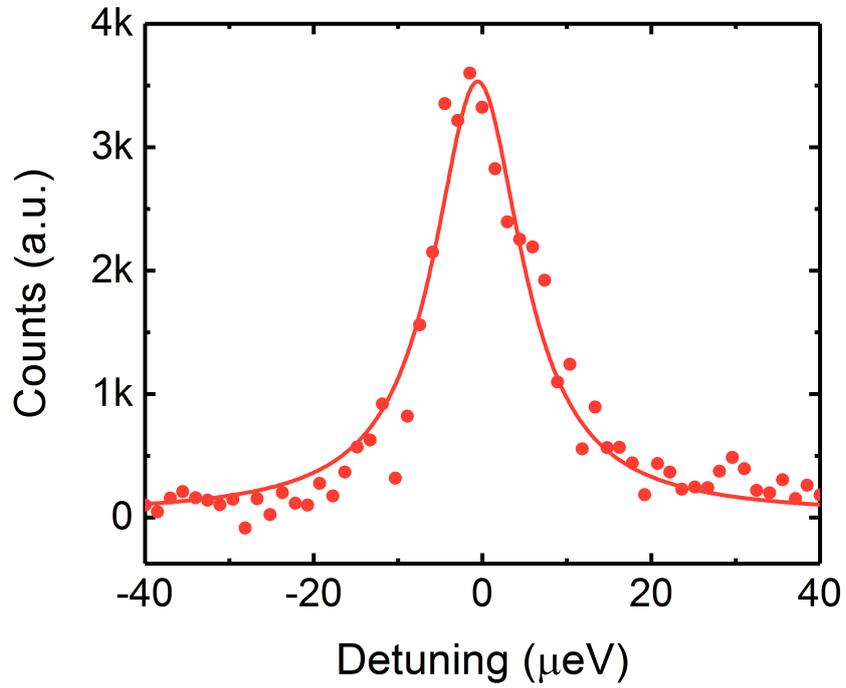
Figure 6-5: RF spectrum of the QD. Solid line is a Lorentzian fit with a FWHM of 12.6 μeV.
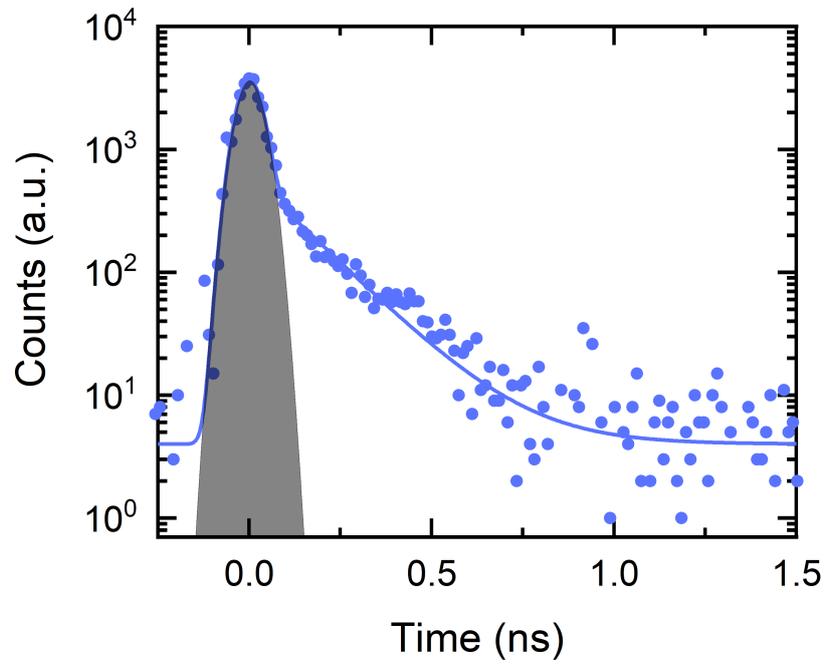
Figure 6-6: Lifetime measurement of the QD. The instrument response of 40 ps is shown in grey. The solid blue line is exponential fit with a decay constant of 150 ps.

6.4   Results

6.4.1   Transmission of a QD exhibiting Fano interference

Next the effect of the QD on waveguide transmission is probed. It is expected from
the estimate of ϕ that this QD will have an asymmetric lineshape in transmission.
In this measurement a weak tuneable continuous laser is injected into the waveguide
and the output power is measured as a function of QD-laser detuning. The input
power of 500nW is chosen such that, on average, less than one photon interacts with
the QD within the lifetime of the exciton.

A transmission spectrum of the device is shown in Figure 6-7. In these measure-
ments, the QD transition energy is fixed and the laser is tuned through resonance
with the QD. The transmission at each point is normalised to the waveguide trans-
mission at that wavelength with the QD far detuned from the laser, as in chapter 5.
The QD shows a strongly asymmetric lineshape with a minimum of 0.4 and a maxi-
mum of 1.8. From fitting the transmission data using Equation 6.3 and the methods
presented in section 5.5, we extract values for the Fano parameter, $\phi = 0.3\pi$, the
coupling efficiency, $\beta = 0.9$ and the blinking probability (fraction of time that the
QD is in a dark state, as described in section 5.5) $\alpha = 0.01$. This fit matches the
data across most of the spectrum, however there is a significant deviation between
915.01nm and 915.04nm. The cause of this discrepancy is unclear.

Voltage tuning of the device is shown in Figure 6-8. The QD is tuned to shorter
wavelength as the bias is increased, and the central position of the line tunes accord-
ingly. The Fano lineshape does not change as the QD is tuned, because the tuning
range of the QD (<0.1 nm) is small in comparison to the period of the F-P modes.
The charge state of the QD changes abruptly at 6.8 V. At this bias the full effect of
the QD, including the Fano interference which is visible at large detuning from the
QD-transition, disappears abruptly.

The transmission measurement confirms the presence of Fano interference in this
device, and the strength of the QD-waveguide interaction. At the transmission mini-
mum, waveguide transmission is reduced by 60%, at the maximum it is increased by
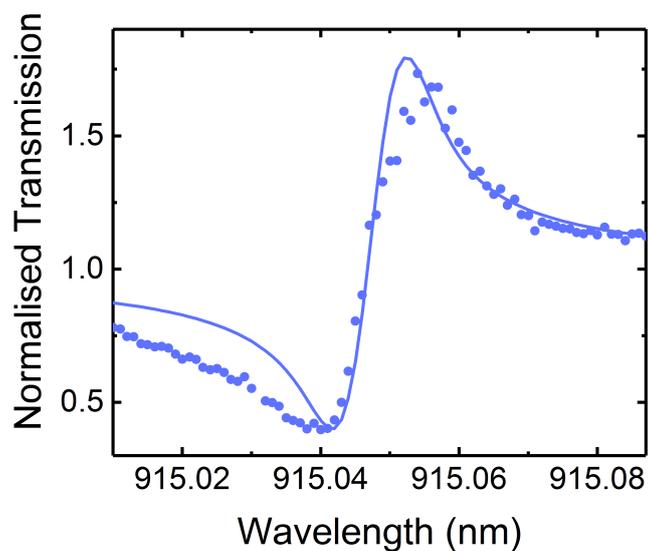
Figure 6-7: Single transmission spectrum with the bias fixed at 6.65 V. The solid blue line is a fit to theory.
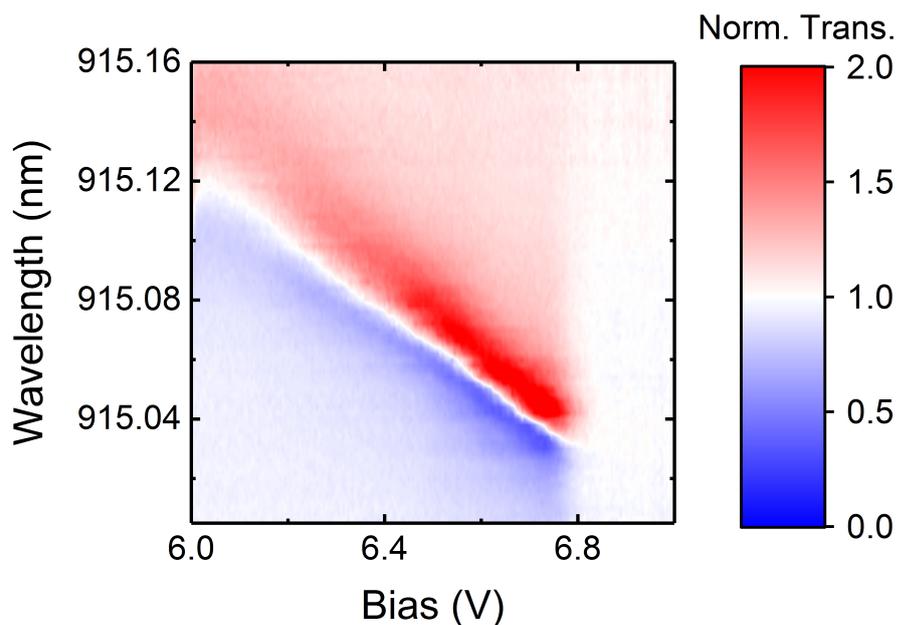
Figure 6-8: Transmission of the device as a function of laser wavelength and bias. The Fano asymmetry is clearly visible across the full charge plateau. The charge state of the QD changes at 6.8V.

80%. ϕ for this QD is calculated to be 0.3π. In Figure 6-11 it is predicted that a QD with this value of ϕ can generate antibunched light due to the effect of the Fano interference.

6.4.2   Tuning the photon statistics of a coherent input

Now we demonstrate the performance of the device as a tuneable quantum optical filter. A weak coherent source is injected to the waveguide, and the autocorrelation function of the transmitted field is measured as a function of QD-laser detuning. In previous measurements [43, 165] bunching is observed at the transmission minimum. It is expected that the Fano interference in this device will allow the generation of either bunched or antibunched light.

The second order autocorrelation function ($g^{(2)}(0)$) of the transmitted field is mea-
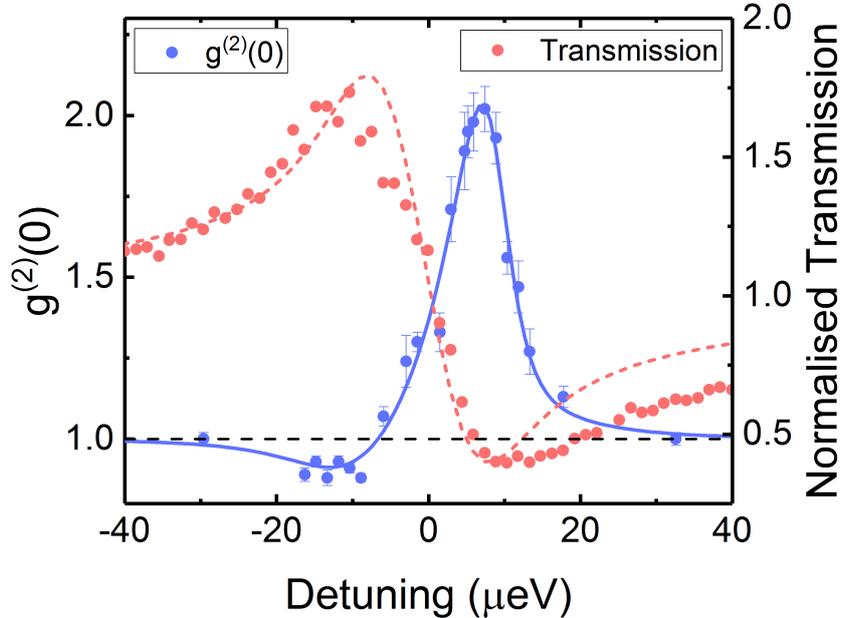
Figure 6-9: Second order autocorrelation function (blue) and waveguide transmission (red) as a function of detuning. The solid blue line is a fit to the model. The dashed red line is a model of the waveguide transmission generated using the same fit parameters.

sured using a Hanbury Brown-Twiss setup. The measurement setup has a convolved instrument response time of 80 ps. The QD-laser detuning is changed in this measurement by tuning the laser wavelength, the bias can also be used to change the QD-laser detuning.

The measured autocorrelation function of the output is shown in Figure 6-9, the transmission spectrum of the QD is shown on the same plot. It can be clearly seen

that the device can generate either bunched or antibunched light, dependent on the QD-laser detuning. At +10 μeV, corresponding to the minimum in transmission, the output is bunched with a maximum value of 2.0. At -10 μeV, corresponding to the maximum in transmission, the output is antibunched with a minimum value of 0.88. The solid blue line on Figure 6-9 is a theoretic fit, the theory of the autocorrelation function is discussed later, in section 6.5. The fit uses Equation 6.4, and accounts for spectral wandering and blinking as in section 5.5. In addition, the effect of the finite detector response time on the measured value of $g^{(2)}(0)$ is calculated. We test the validity of this fit by using the same parameters to produce an estimate of the transmission from Equation 6.3. This estimate is the dashed red line. It can be seen that this estimate is in good agreement with the measured data. Thus, we have demonstrated number state filtering of photon statistics in a waveguide coupled device, using the detuning as a single control parameter.

6.5 Discussion of the generation of antibunching in a QD-waveguide system

In this section, we consider the effect of Fano interference on the autocorrelation function of transmitted light in the 1-D atom model. We discuss the optimum value of ϕ for generating both strong bunching and antibunching in the same device. The contributions of the two-photon plane wave states and two-photon bound states to the transmission are considered. Finally, the theoretical model is compared to real data, and the differences between the two are explained.

The normalised autocorrelation function is given by Equation 6.4.

$$g^{(2)}(0, \delta) = \frac{1}{|t_1(\delta)|^4} \left| t_1(\delta)^2 - \frac{e^{2i\phi}\beta^2}{|t_0|^2(1+\delta^2)} \right|^2,$$

(6.4)

where $t_1(\delta)$ is the transmission intensity calculated in Equation 6.4.

The autocorrelation functions of transmitted light for devices with different values of ϕ are presented in Figure 6-10. For devices where $\phi = 0$ the transmitted light is bunched when the QD and laser are resonant, no antibunching is visible at any
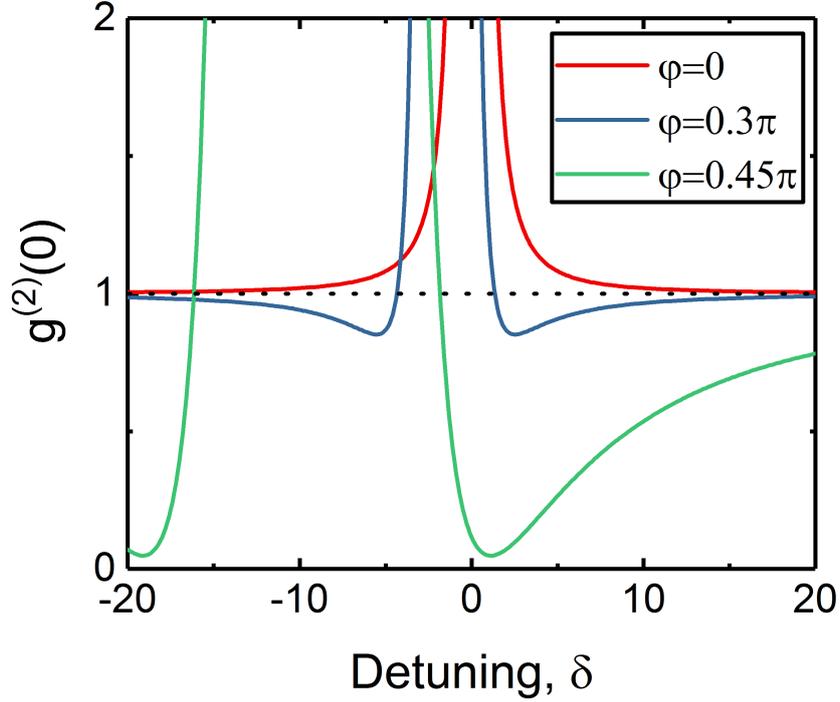
Figure 6-10: Autocorrelation function of the light transmitted through a QD for different values of ϕ. For $\phi = 0$ the output is bunched when resonant with the transmission minimum. For $\phi = 0.3\pi$ the output is still bunched when resonant with the transmission minimum, which has tuned slightly away from the QD resonance, however antibunching is now visible to either side of the bunching. For $\phi = 0.45\pi$ this antibunching is enhanced, allowing tuning of the photon statistics from strongly antibunched at $\delta = 0$ to strongly bunched at $\delta = -10$.

detuning. This is the case presented in chapter 5.

At $\phi = 0.3\pi$, the same bunching is predicted at the transmission minimum, weak antibunching is predicted either side of the minimum. The results presented in Figure 6-9 were for a device with $\phi = 0.3\pi$. In that data, antibunching is only visible to one side of the transmission minimum. The reasons for this are discussed at the end of this section.

At $\phi = 0.45\pi$ strong antibunching is visible at $\delta = 0$ and $\delta = -20$, strong bunching is still predicted at $\delta = -10$. In the ideal case, as ϕ approaches $\pi/2$, the minimum achievable $g^{(2)}(0)$ approaches 0, while the maximum bunching is still very large. Note that $\pi/2$ is not plotted here as that would result in a waveguide transmission of 0, creating infinities in the calculation of $g^{(2)}(0)$. For a device with $0.45\pi < \phi < \pi/2$, Fano

interference would allow the photon statistics can be tuned from strongly bunched to strongly antibunched by changing the detuning of the QD and laser. This is not achievable in this device because the finesse of the Fabry-Pérot modes is too low; this could be increased by increasing the reflectivity at the ends of the waveguides.

Understanding of the photon statistics requires the consideration of two kinds of two-photon states. These are two-photon product (separable) states, and two-photon bound (frequency entangled) states [41,117]. The two-photon product state is considered to interact with the QD as two separate photons. The two-photon bound state is considered to interact with the QD as a single particle. The first term in Equation 6.4 represents the two-photon product state, the second represents the two-photon bound state. It has previously been shown that the two-photon product state is required to observe bunching in a QD-waveguide system [38]. In order to explain the generation of antibunching interference between the two types of state must be considered. In order to do this Equation 6.4 is expanded to form Equation 6.5.

$$g^{(2)}(0,\delta) = 1 + \frac{1}{|t_1(\delta)|^4 \, (\delta + tan(\phi))^4} + \frac{2cos(2\phi)}{|t_1(\delta)|^4(\delta + tan(\phi))^2}, \tag{6.5}$$

Equation 6.5 consists of three terms. The first term is the contribution of the two-photon product state. The second term is the contribution of the two-photon bound state. The third term describes interference between the product states and bound states.

The contributions of the different terms in Equation 6.5 are examined in Figure 6-11 for the three cases of $\phi = 0, \phi = 0.3\pi$ and $\phi = 0.45\pi$. The contribution of the product state is always unity; this is because the product state describes two photons interacting separately with the QD, therefore the two-photon case and the case of two single-photons are identical and there is no effect on the photon statistics. For all three cases, the bound state gives a positive contribution, which goes to infinity at the transmission minimum of the QD resonance. The position of this minimum is tunes away from the zero detuning as the strength of Fano interference is increased.

Note that the bound state always gives a positive contribution to the $g^{(2)}(0)$, enabling the generation of bunching but not antibunching.

The interference term is the term responsible for generating antibunching. This term gives a positive contribution for $\phi < \pi/4$, and a negative contribution for $\pi/4 < \phi < \pi/2$. This negative contribution is required to measure a $g^{(2)}(0) < 1$ The contributions of the bound state term and interference term are both very large when at the transmission minimum of the resonance. The bound state term is larger and narrower than the interference term, resulting in a central bunching peak with antibunching predicted when the QD is detuned to either side of the minimum.

There is a notable difference between the measured autocorrelation function and the theoretical prediction. In Figure 6-10 antibunching is predicted when the QD is detuned to either side of the bunched peak, in experiment antibunching is only observed to one side of the peak - corresponding to the maximum of waveguide transmission. This difference is caused by the effect of spectral wandering, and the detector response time. We use the parameters extracted from fitting the data to estimate device behaviour in the abscence of these effects. These estimates are presented in Figure 6-12. It can be seen that when these effects are not present, the behaviour predicted in Figure 6-10 is recovered, and two regions of antibunching can be seen.
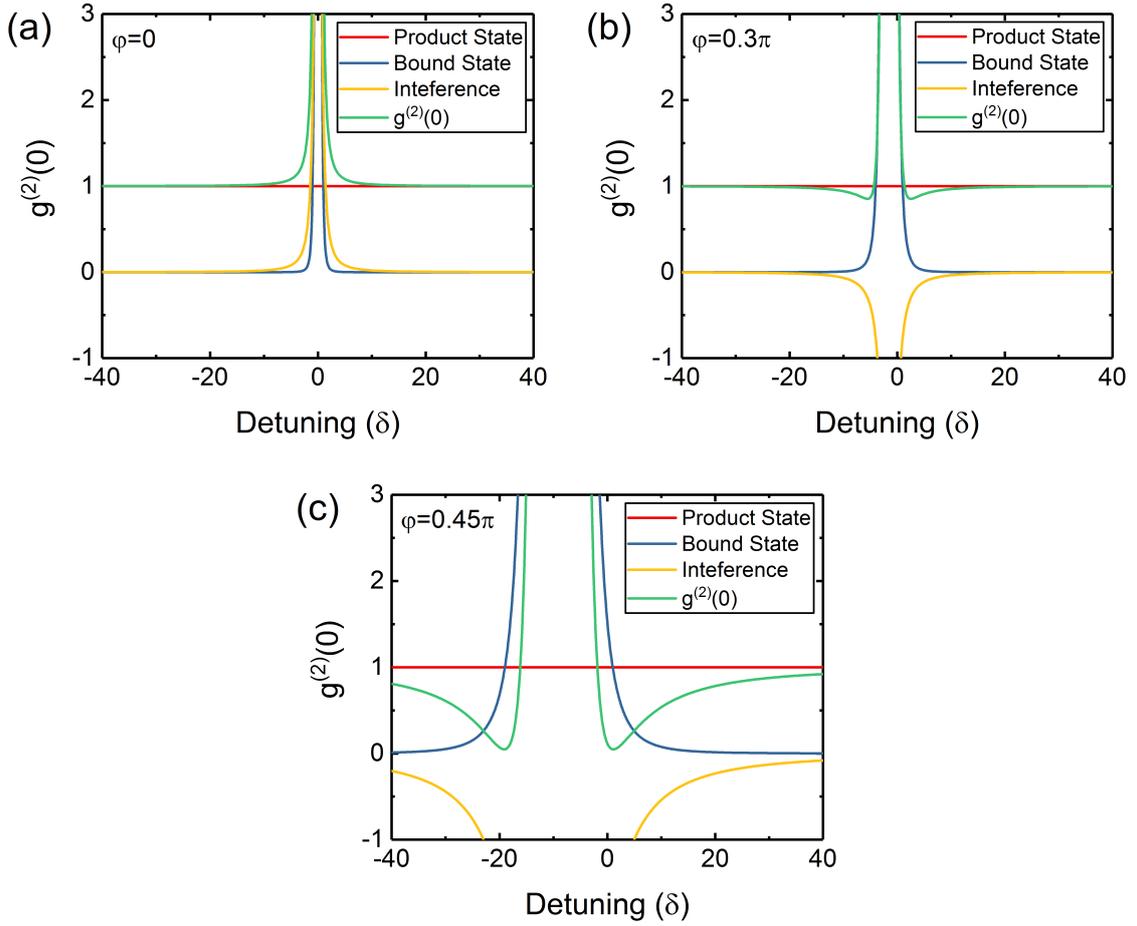
Figure 6-11: Autocorrelation function of the transmitted light for (a) $\phi = 0$, (b) $\phi = 0.3\pi$ and (c) $\phi = 0.45\pi$. Each figure shows the contributions of the different states described in Equation 6.5. The two-photon product state is always 1. The two-photon bound state always gives a positive contribution to $g^{(2)}(0)$. The contribution of interference between the product and bound states gives a different contribution depending on the parameters of Fano interference, enabling the observation of antibunching where ϕ is in the range $\pi/4 < \phi < \pi/2$. The autocorrelation function, $g^{(2)}(0)$, is the sum of the three contributions.
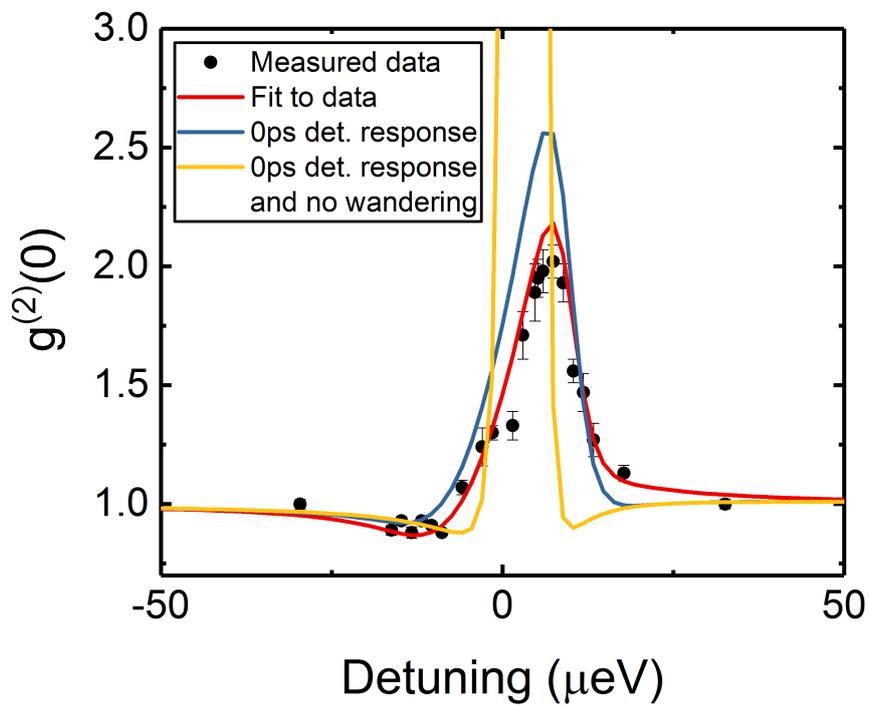
Figure 6-12: Effect of spectral wandering and a finite detector response time on the observed $g^{(2)}(0)$. The red line is the fit to the measured data; the blue line is the $g^{(2)}(0)$ obtained with infinitely fast detectors; and the yellow line is the $g^{(2)}(0)$ obtained in the absence of spectral wandering with infinitely fast detectors

6.6 Conclusion

We have demonstrated an integrated quantum optical filter based on Fano interference in a waveguide coupled system consisting of a single quantum dot in a single-mode nanophotonic waveguide. A coherent input to this system is converted to create either a bunched or antibunched output. We note that the precise measurements of the autocorrelation function are enabled by the large effect of the QD in transmission, optimised in chapter 5. Antibunching in this system is only enabled by the interference between the two-photon product state and the two-photon bound state, and is only accessible due to the Fano interference between the QD and the F-P waveguide modes. This filter is coupled to waveguides, enabling integration of this filter into a larger quantum photonic circuit.

Theory indicates that strong antibunching can be generating by creating a device in which ϕ approaches $\pi/2$; achieving this presents several experimental challenges. Firstly in the waveguide studied here the F-P modes overlap, restricting access to this regime. This is because the reflectivity of the interfaces causing the modes is low. Furthermore, since achieving this value of ϕ requires tuning away from the F-P mode, the Purcell effect on the QD is reduced. This has a detrimental effect on the coupling efficiency of the QD, and on the effect of spectral wandering. This system can be used to electrically modulate photon statistics, allowing local control of the device. Electrical tuning of the QD can be used to tune the photon statistics without changing other properties of the output photons; this is in contrast to modulating the laser energy, as done in other work, which changes the wavelength of output photons.

7 — SUMMARY AND OUTLOOK

This thesis has presented optical measurements of several nanophotonic devices incorporating embedded III-V quantum dots. These devices are able to create and manipulate quantum states of light on-chip. These measurements represent significant progress towards an integrated quantum optical processor. Chapter 1 introduces the context of the work, and the field of quantum optical processing.

Chapter 2 summarises relevant background informationfor the material in this thesis. This includes a brief discussion of photon statistics; an introduction to quantum dots and nanophotonic devices; and descriptions of the 1D atom model and Fano interference.

Chapter 3 describes the methods used to perform the experiments in this thesis. These methods include the fabrication techniques used to create the devices, the computational modelling used to design the devices and the experimental techniques used to test the devices.

7.1 Summary

Chapter 4: Generation of coherent electrically driven single-photons coupled to a single mode waveguide

In Chapter 4 an integrated electrically-driven single-photon source was demonstrated. Spatial selection was used to isolate emission from a single QD into a single-mode nanophotonic waveguide. The single photon nature of the emission was demonstrated with autocorrelation measurements. The coherence of the source was measured using interferometry.

Chapter 5: Electrical control of a waveguide-coupled non-linearity

In Chapter 5 the non-linear behaviour of a single quantum dot coupled to a single-mode waveguide was investigated. The QD acts as an integrated non-linearity, which enables nanophotonic logic gates. The non-linear behaviour of the QD is evident in the power dependence of the device in transmission. The single-photon nature of the non-linearity is evidenced by bunching in the transmitted light. In addition detailed resonance fluorescence and resonant transmission measurements on three different charge states of the same QD are presented.

Chapter 6: Using Fano interference to control photon statistics on-chip

In Chapter 6 an integrated quantum optical filter is demonstrated. The filter modulates a coherent input to produce bunched or antibunched light. The photon statistics of the output field can be controlled by electrically tuning the device. The device consists of a single QD in a single-mode waveguide supporting weak Fabry-Perot cavity modes.

7.2 Outlook

In the following section some possible directions for future investigation are presented. These consist of steps to improve the measured devices, and experiments which develop the research further.

One important direction which applies to all the chapters is the demonstration of devices which integrate multiple quantum dots. This integration has been shown in simple devices [169], and is required in order to scale the quantum photonic devices demonstrated in this work into fully integrated quantum photonic circuits. One important technique for improving scalability in these devices is deterministic fabrication. In this technique single QDs are selected, and devices are deterministically

fabricated [161–164]. Using this technique it would be possible to select two QDs which emit at the same wavelength, and then fabricate a device around them.

7.2.1 Chapter 4: Generation of coherent electrically driven single-photons coupled to a single mode waveguide

This chapter demonstrated single photon emission coupled to a nanophotonic waveguide. The coupling efficiency of the device was limited to 50% because light was allowed to couple to both directions of the waveguide, this coupling efficiency could be improved by creating a mirror on one side of the QD. The brightness of the source could be improved by creating mirrors on both sides of the QD, creating a cavity. This cavity could be implemented in either a nanobeam [152, 170] or photonic crystal [171, 172] waveguide.

In this work, isolation of emission from a single QD was achieved using off-chip spectral filtering. This filtering removes emission from the wetting layer of the device, and emission from other QDs. In order to realise a fully on-chip electrically-driven circuit, this filtration needs to be performed on-chip. Waveguide-coupled cavities [170, 173, 174] have been shown to act as narrow bandwidth spectral filters suitable for this application.

It is important to be able to integrate this source to other nano-photonic devices. One simple component which could have an integrated electrically driven source is a beam splitter. This could be used to perform an HBT measurement on chip [94], or to demonstrate interference between two electrically driven sources on-chip, which would be a major milestone in the development of quantum photonic circuits.

7.2.2 Chapter 5: Electrical control of a waveguide-coupled non-linearity

This chapter demonstrated the potential of the QD-waveguide system as a non-linear element and a light-matter interface. High coupling efficiencies were obtained using well known fabrication methods, and blinking was nearly eliminated due to the charge stabilisation of the electric field. The main process limiting the efficiency of the

interaction was spectral wandering. In order to improve the efficiency of the effect, spectral wandering needs to be reduced. This could be achieved either by reducing charge and spin noise in the device [34], or by increasing the spontaneous decay rate of the emitter via a larger Purcell factor [53].

One interesting property of the 1D atom system is that a frequency-dependent phase shift is induced in the photons [40]. This phase shift switches from $+\pi/2$ to $-\pi/2$ over a frequency range on the order of the linewidth of the emitter. This phase shift could be used to realise controlled-phase quantum logic gates [19]. Measuring the magnitude of this phase shift in the transmitted/reflected photons requires a homodyne measurement on the transmitted/reflected field. This could be performed using an on-chip Mach-Zehnder interferometer.

7.2.3 Chapter 6: Using Fano interference to control photon statistics on-chip

This chapter demonstrated an integrated quantum optical filter, capable of generating either bunched or antibunched emission from a coherent input. Fano interference is of significant interest for applications requiring fast optical switching, and this work demonstrates that this switching capability extends to photon statistics.

An important development for this device would be the ability to generate strongly antibunched (single-photon) emission in addition to strongly bunched light. This would require increasing the value of ϕ that can be achieved in this system. In the system studied, the available range of ϕ is limited by the overlap of the F-P modes. This increase could be achieved by increasing the reflectivity of the reflecting interfaces which create the F-P modes, resulting in an increased Q-factor and narrower modes. Another implementation would be to integrate a nanocavity into the waveguide device [152], this cavity would support a single fundamental mode. Detuning the QD from the cavity resonance would allow access to large values of ϕ.

Bibliography

[1] N. Gisin, G. Ribordy, W. Tittel, and H. Zbinden. 'Quantum cryptography'. Rev. Mod. Phys. **74**, 145–195 (2002). https://link.aps.org/doi/10.1103/RevModPhys.74.145.

[2] J. P. Olson, K. R. Motes, P. M. Birchall, N. M. Studer, M. LaBorde, T. Moulder, P. P. Rohde, and J. P. Dowling. 'Linear optical quantum metrology with single photons: Experimental errors, resource counting, and quantum Cramér-Rao bounds'. Phys. Rev. A **96**, 013810 (2017). https://link.aps.org/doi/10.1103/PhysRevA.96.013810.

[3] V. Giovannetti, S. Lloyd, and L. Maccone. 'Quantum-Enhanced Measurements: Beating the Standard Quantum Limit'. Science **306**, 5700, 1330–1336 (2004). http://science.sciencemag.org/content/306/5700/1330.

[4] T. D. Ladd, F. Jelezko, R. Laflamme, Y. Nakamura, C. Monroe, and J. L. O'Brien. 'Quantum computers'. Nature **464**, 45 (2010). https://doi.org/10.1038/nature08812.

[5] H. J. Kimble. 'The quantum internet'. Nature **453**, 1023 (2008). https://doi.org/10.1038/nature07127.

[6] S. Lloyd. 'Universal Quantum Simulators'. Science **273**, 5278, 1073–1078 (1996). http://science.sciencemag.org/content/273/5278/1073.

[7] A. Barenco, C. H. Bennett, R. Cleve, D. P. DiVincenzo, N. Margolus, P. Shor, T. Sleator, J. A. Smolin, and H. Weinfurter. 'Elementary gates for quantum computation'. Phys. Rev. A **52**, 3457–3467 (1995). https://link.aps.org/doi/10.1103/PhysRevA.52.3457.

[8] P. W. Shor. 'Algorithms for quantum computation: discrete logarithms and factoring'. In 'Proceedings 35th Annual Symposium on Foundations of Computer Science', 124–134 (1994).

[9] D. P. DiVincenzo. 'The Physical Implementation of Quantum Computation'. Fortschritte der Physik **48**, 9-11, 771–783 (2000). https://arxiv.org/abs/quant-ph/0002077.

[10] D. W. Berry, G. Ahokas, R. Cleve, and B. C. Sanders. 'Efficient Quantum Algorithms for Simulating Sparse Hamiltonians'. Communications in Mathematical Physics **270**, 2, 359–371 (2007). https://doi.org/10.1007/s00220-006-0150-x.

[11] A. Neville, C. Harrold, J. Carolan, Y. N. Joglekar, T. Hashimoto, N. Matsuda, J. L. O'Brien, D. P. Tew, and A. Laing. 'Simulating the vibrational quantum dynamics of molecules using photonics'. Nature **557**, 660–667 (2018). https://doi.org/10.1038/s41586-018-0152-9.

[12] D. W. Berry, A. M. Childs, R. Cleve, R. Kothari, and R. D. Somma. 'Simulating Hamiltonian Dynamics with a Truncated Taylor Series'. Phys. Rev. Lett. **114**, 090502 (2015). https://link.aps.org/doi/10.1103/PhysRevLett.114.090502.

[13] A. J. Bennett, J. P. Lee, D. J. P. Ellis, T. Meany, E. Murray, F. F. Floether, J. P. Griffths, I. Farrer, D. A. Ritchie, and A. J. Shields. 'Cavity-enhanced coherent light scattering from a quantum dot'. Science Advances **2**, e1501256 (2016). http://advances.sciencemag.org/content/2/4/e1501256.

[14] M. Müller, H. Vural, C. Schneider, A. Rastelli, O. G. Schmidt, S. Höfling, and P. Michler. 'Quantum-Dot Single-Photon Sources for Entanglement Enhanced Interferometry'. Phys. Rev. Lett. **118**, 257402 (2017). https://link.aps.org/doi/10.1103/PhysRevLett.118.257402.

[15] J. A. Jones. 'Robust Ising gates for practical quantum computation'. Phys. Rev. A **67**, 012317 (2003). https://link.aps.org/doi/10.1103/PhysRevA.67.012317.

[16] A. Tipsmark, R. Dong, A. Laghaout, P. Marek, M. Ježek, and U. L. Andersen. 'Experimental demonstration of a Hadamard gate for coherent state qubits'. Phys. Rev. A **84**, 050301 (2011). https://link.aps.org/doi/10.1103/PhysRevA.84.050301.

[17] K. Nemoto and W. J. Munro. 'Nearly Deterministic Linear Optical Controlled-NOT Gate'. Phys. Rev. Lett. **93**, 250502 (2004). https://link.aps.org/doi/10.1103/PhysRevLett.93.250502.

[18] K. Park, P. Marek, and R. Filip. 'Deterministic nonlinear phase gates induced by a single qubit'. New Journal of Physics **20**, 5, 053022 (2018). https://doi.org/10.1088%2F1367-2630%2Faabb86.

[19] A. Nysteen, D. P. S. McCutcheon, M. Heuck, J. Mørk, and D. R. Englund. 'Limitations of two-level emitters as nonlinearities in two-photon controlled-phase gates'. Phys. Rev. A **95**, 062304 (2017). https://link.aps.org/doi/10.1103/PhysRevA.95.062304.

[20] I. Fushman, D. Englund, A. Faraon, N. Stoltz, P. Petroff, and J. Vučković. 'Controlled Phase Shifts with a Single Quantum Dot'. Science **320**, 5877, 769–772 (2008). http://science.sciencemag.org/content/320/5877/769.

[21] E. Knill, R. Laflamme, and G. J. Milburn. 'A scheme for efficient quantum computation with linear optics'. Nature **409**, 46 (2001). https://doi.org/10.1038/35051009.

[22] P. Kok, W. J. Munro, K. Nemoto, T. C. Ralph, J. P. Dowling, and G. J. Milburn. 'Linear optical quantum computing with photonic qubits'. Rev. Mod. Phys. **79**, 135–174 (2007). https://link.aps.org/doi/10.1103/RevModPhys.79.135.

[23] J. Carolan, C. Harrold, C. Sparrow, E. Martín-López, N. J. Russell, J. W. Silverstone, P. J. Shadbolt, N. Matsuda, M. Oguma, M. Itoh, G. D. Marshall, M. G. Thompson, J. C. F. Matthews, T. Hashimoto, J. L. O'Brien, and A. Laing. 'Universal linear optics'. Science **349**, 6249, 711–716 (2015). http://science.sciencemag.org/content/349/6249/711.

[24] J. L. O'Brien. 'Optical Quantum Computing'. Science **318**, 5856, 1567–1570 (2007). http://science.sciencemag.org/content/318/5856/1567.

[25] D. E. Chang, A. S. Sørensen, E. A. Demler, and M. D. Lukin. 'A single-photon transistor using nanoscale surface plasmons'. Nature Physics **3**, 807 (2007). http://dx.doi.org/10.1038/nphys708.

[26] S. G. Carter, T. M. Sweeney, M. Kim, C. S. Kim, D. Solenov, S. E. Economou, T. L. Reinecke, L. Yang, A. S. Bracker, and D. Gammon. 'Quantum control of a spin qubit coupled to a photonic crystal cavity'. Nature Photonics **7**, 329 (2013). https://doi.org/10.1038/nphoton.2013.41.

[27] J. L. O'Brien, A. Furusawa, and J. Vučković. 'Photonic quantum technologies'. Nature Photonics **3**, 687 (2009). https://doi.org/10.1038/nphoton.2009.229.

[28] M. A. Pooley, D. J. P. Ellis, R. B. Patel, A. J. Bennett, K. H. A. Chan, I. Farrer, D. A. Ritchie, and A. J. Shields. 'Controlled-NOT gate operating with single photons'. Applied Physics Letters **100**, 21, 211103 (2012). https://doi.org/10.1063/1.4719077.

[29] W.-H. Chang, W.-Y. Chen, H.-S. Chang, T.-P. Hsieh, J.-I. Chyi, and T.-M. Hsu. 'Efficient Single-Photon Sources Based on Low-Density Quantum Dots in Photonic-Crystal Nanocavities'. Phys. Rev. Lett. **96**, 117401 (2006). https://link.aps.org/doi/10.1103/PhysRevLett.96.117401.

[30] M. Pelton, C. Santori, J. Vučković, B. Zhang, G. S. Solomon, J. Plant, and Y. Yamamoto. 'Efficient Source of Single Photons: A Single Quantum Dot

in a Micropost Microcavity'. Phys. Rev. Lett. **89**, 233602 (2002). `https://link.aps.org/doi/10.1103/PhysRevLett.89.233602`.

[31] F. Liu, A. J. Brash, J. O'Hara, L. M. P. P. Martins, C. L. Phillips, R. J. Coles, B. Royall, E. Clarke, C. Bentham, N. Prtljaga, I. E. Itskevich, L. R. Wilson, M. S. Skolnick, and A. M. Fox. 'High Purcell factor generation of indistinguishable on-chip single photons'. Nature Nanotechnology **13**, 835–840 (2018). `https://doi.org/10.1038/s41565-018-0188-x`.

[32] I. Shomroni, S. Rosenblum, Y. Lovsky, O. Bechler, G. Guendelman, and B. Dayan. 'All-optical routing of single photons by a one-atom switch controlled by a single photon'. Science **345**, 6199, 903–906 (2014). `http://science.sciencemag.org/content/345/6199/903`.

[33] J. E. Mooij, T. P. Orlando, L. Levitov, L. Tian, C. H. van der Wal, and S. Lloyd. 'Josephson Persistent-Current Qubit'. Science **285**, 5430, 1036–1039 (1999). `http://science.sciencemag.org/content/285/5430/1036`.

[34] A. V. Kuhlmann, J. H. Prechtel, J. Houel, A. Ludwig, D. Reuter, A. D. Wieck, and R. J. Warburton. 'Transform-limited single photons from a single quantum dot'. Nature Communications **6**, 8204 (2015). `https://doi.org/10.1038/ncomms9204`.

[35] S. Tanzilli, A. Martin, F. Kaiser, M. De Micheli, O. Alibart, and D. Ostrowsky. 'On the genesis and evolution of Integrated Quantum Optics'. Laser & Photonics Reviews **6**, 1, 115–143 (2012). `https://onlinelibrary.wiley.com/doi/abs/10.1002/lpor.201100010`.

[36] M. A. Nielsen. 'Optical Quantum Computation Using Cluster States'. Phys. Rev. Lett. **93**, 040503 (2004). `https://link.aps.org/doi/10.1103/PhysRevLett.93.040503`.

[37] Y. He, X. Ding, Z.-E. Su, H.-L. Huang, J. Qin, C. Wang, S. Unsleber, C. Chen, H. Wang, Y.-M. He, X.-L. Wang, W.-J. Zhang, S.-J. Chen, C. Schneider,

M. Kamp, L.-X. You, Z. Wang, S. Höfling, C.-Y. Lu, and J.-W. Pan. 'Time-Bin-Encoded Boson Sampling with a Single-Photon Device'. Phys. Rev. Lett. **118**, 190501 (2017). https://link.aps.org/doi/10.1103/PhysRevLett.118.190501.

[38] H. Zheng, D. J. Gauthier, and H. U. Baranger. 'Waveguide QED: Many-body bound-state effects in coherent and Fock-state scattering from a two-level system'. Phys. Rev. A **82**, 063816 (2010). https://link.aps.org/doi/10.1103/PhysRevA.82.063816.

[39] Ş. E. Kocabaş, E. Rephaeli, and S. Fan. 'Resonance fluorescence in a waveguide geometry'. Phys. Rev. A **85**, 023817 (2012). https://link.aps.org/doi/10.1103/PhysRevA.85.023817.

[40] S. Fan, i. m. c. E. Kocabaş, and J.-T. Shen. 'Input-output formalism for few-photon transport in one-dimensional nanophotonic waveguides coupled to a qubit'. Phys. Rev. A **82**, 063821 (2010). https://link.aps.org/doi/10.1103/PhysRevA.82.063821.

[41] J.-T. Shen and S. Fan. 'Strongly Correlated Two-Photon Transport in a One-Dimensional Waveguide Coupled to a Two-Level System'. Phys. Rev. Lett. **98**, 153003 (2007). https://link.aps.org/doi/10.1103/PhysRevLett.98.153003.

[42] P. Lodahl, S. Mahmoodian, and S. Stobbe. 'Interfacing single photons and single quantum dots with photonic nanostructures'. Rev. Mod. Phys. **87**, 347–400 (2015). https://link.aps.org/doi/10.1103/RevModPhys.87.347.

[43] A. Javadi, I. Söllner, M. Arcari, S. L. Hansen, L. Midolo, S. Mahmoodian, G. Kirsanske, T. Pregnolato, E. H. Lee, J. D. Song, S. Stobbe, and P. Lodahl. 'Single-photon non-linear optics with a quantum dot in a waveguide'. Nature Communications **6**, 8655 (2015). http://dx.doi.org/10.1038/ncomms9655.

[44] T. M. Babinec, B. J. M. Hausmann, M. Khan, Y. Zhang, J. R. Maze, P. R. Hemmer, and M. Loncar. 'A diamond nanowire single-photon source'. Nature Nanotechnology **5**, 195 (2010). http://dx.doi.org/10.1038/nnano.2010.6.

[45] B. P. Lanyon, C. Hempel, D. Nigg, M. Müller, R. Gerritsma, F. Zähringer, P. Schindler, J. T. Barreiro, M. Rambach, G. Kirchmair, M. Hennrich, P. Zoller, R. Blatt, and C. F. Roos. 'Universal Digital Quantum Simulation with Trapped Ions'. Science **334**, 6052, 57–61 (2011). http://science.sciencemag.org/content/334/6052/57.

[46] Q. A. Turchette, C. J. Hood, W. Lange, H. Mabuchi, and H. J. Kimble. 'Measurement of Conditional Phase Shifts for Quantum Logic'. Phys. Rev. Lett. **75**, 4710–4713 (1995). https://link.aps.org/doi/10.1103/PhysRevLett.75.4710.

[47] D. Wang, H. Kelkar, D. Martin-Cano, T. Utikal, S. Götzinger, and V. Sandoghdar. 'Coherent Coupling of a Single Molecule to a Scanning Fabry-Perot Microcavity'. Phys. Rev. X **7**, 021014 (2017). https://link.aps.org/doi/10.1103/PhysRevX.7.021014.

[48] J. Volz, M. Scheucher, C. Junge, and A. Rauschenbeutel. 'Nonlinear π phase shift for single fibre-guided photons interacting with a single resonator-enhanced atom'. Nature Photonics **8**, 965 (2014). https://doi.org/10.1038/nphoton.2014.253.

[49] P. Türschmann, N. Rotenberg, J. Renger, I. Harder, O. Lohse, T. Utikal, S. Götzinger, and V. Sandoghdar. 'Chip-Based All-Optical Control of Single Molecules Coherently Coupled to a Nanoguide'. Nano Letters **17**, 8, 4941–4945 (2017). https://doi.org/10.1021/acs.nanolett.7b02033.

[50] J. D. Thompson, T. G. Tiecke, N. P. de Leon, J. Feist, A. V. Akimov, M. Gullans, A. S. Zibrov, V. Vuletić, and M. D. Lukin. 'Coupling a Single Trapped Atom to a Nanoscale Optical Cavity'. Science **340**, 6137, 1202–1205 (2013). http://science.sciencemag.org/content/340/6137/1202.

[51] J. Liu, K. Konthasinghe, M. Davanço, J. Lawall, V. Anant, V. Verma, R. Mirin, S. W. Nam, J. D. Song, B. Ma, Z. S. Chen, H. Q. Ni, Z. C. Niu, and K. Srinivasan. 'Single Self-Assembled InAs/GaAs Quantum Dots in Photonic Nanostructures: The Role of Nanofabrication'. Phys. Rev. Applied **9**, 064019 (2018). https://link.aps.org/doi/10.1103/PhysRevApplied.9.064019.

[52] H. D. Robinson and B. B. Goldberg. 'Light-induced spectral diffusion in single self-assembled quantum dots'. Phys. Rev. B **61**, R5086–R5089 (2000). https://link.aps.org/doi/10.1103/PhysRevB.61.R5086.

[53] N. Somaschi, V. Giesz, L. De Santis, J. C. Loredo, M. P. Almeida, G. Hornecker, S. L. Portalupi, T. Grange, C. Antón, J. Demory, C. Gómez, I. Sagnes, N. D. Lanzillotti-Kimura, A. Lemaítre, A. Auffeves, A. G. White, L. Lanco, and P. Senellart. 'Near-optimal single-photon sources in the solid state'. Nature Photonics **10**, 340 (2016). http://dx.doi.org/10.1038/nphoton.2016.23.

[54] M. Fox. *Quantum Optics: An Introduction*. Oxford University Press (2006).

[55] H. J. Kimble, M. Dagenais, and L. Mandel. 'Photon Antibunching in Resonance Fluorescence'. Phys. Rev. Lett. **39**, 691–695 (1977). https://link.aps.org/doi/10.1103/PhysRevLett.39.691.

[56] P. Michler, A. Kiraz, C. Becher, W. V. Schoenfeld, P. M. Petroff, L. Zhang, E. Hu, and A. Imamoglu. 'A Quantum Dot Single-Photon Turnstile Device'. Science **290**, 5500, 2282–2285 (2000). http://science.sciencemag.org/content/290/5500/2282.

[57] S. Strauf, N. G. Stoltz, M. T. Rakher, L. A. Coldren, P. M. Petroff, and D. Bouwmeester. 'High-frequency single-photon source with polarization control'. Nature Photonics **1**, 704 (2007). https://doi.org/10.1038/nphoton.2007.227.

[58] Z. Yuan, B. E. Kardynal, R. M. Stevenson, A. J. Shields, C. J. Lobo, K. Cooper, N. S. Beattie, D. A. Ritchie, and M. Pepper. 'Electrically Driven Single-Photon

Source'. Science **295**, 5552, 102–105 (2002). http://science.sciencemag.org/content/295/5552/102.

[59] L. Hanschke, K. A. Fischer, S. Appel, D. Lukin, J. Wierzbowski, S. Sun, R. Trivedi, J. Vučković, J. J. Finley, and K. Müller. 'Quantum dot single-photon sources with ultra-low multi-photon probability'. npj Quantum Information **4**, 43 (2018). https://doi.org/10.1038/s41534-018-0092-0.

[60] R. Brouri, A. Beveratos, J.-P. Poizat, and P. Grangier. 'Photon antibunching in the fluorescence of individual color centers in diamond'. Opt. Lett. **25**, 17, 1294–1296 (2000). http://ol.osa.org/abstract.cfm?URI=ol-25-17-1294.

[61] A. J. Bennett, J. P. Lee, D. J. P. Ellis, I. Farrer, D. A. Ritchie, and A. J. Shields. 'A semiconductor photon-sorter'. Nature Nanotechnology **11**, 857 (2016). http://dx.doi.org/10.1038/nnano.2016.113.

[62] A. Faraon, I. Fushman, D. Englund, N. Stoltz, P. Petroff, and J. Vuckovic. 'Coherent generation of non-classical light on a chip via photon-induced tunnelling and blockade'. Nature Physics **4**, 859 (2008). http://dx.doi.org/10.1038/nphys1078.

[63] A. Reinhard, T. Volz, M. Winger, A. Badolato, K. J. Hennessy, E. L. Hu, and A. Imamoglu. 'Strongly correlated photons on a chip'. Nature Photonics **6**, 93 (2011). http://dx.doi.org/10.1038/nphoton.2011.321.

[64] K. Müller, A. Rundquist, K. A. Fischer, T. Sarmiento, K. G. Lagoudakis, Y. A. Kelaita, C. Sánchez Muñoz, E. del Valle, F. P. Laussy, and J. Vučković. 'Coherent Generation of Nonclassical Light on Chip via Detuned Photon Blockade'. Phys. Rev. Lett. **114**, 233601 (2015). https://link.aps.org/doi/10.1103/PhysRevLett.114.233601.

[65] C. Dory, K. A. Fischer, K. Müller, K. G. Lagoudakis, T. Sarmiento, A. Rundquist, J. L. Zhang, Y. Kelaita, N. V. Sapra, and J. Vučković. 'Tuning the photon statistics of a strongly coupled nanophotonic system'. Phys.

Rev. A **95**, 023804 (2017). https://link.aps.org/doi/10.1103/PhysRevA.95.023804.

[66] H. J. Snijders, J. A. Frey, J. Norman, H. Flayac, V. Savona, A. C. Gossard, J. E. Bowers, M. P. van Exter, D. Bouwmeester, and W. Löffler. 'Observation of the Unconventional Photon Blockade'. Phys. Rev. Lett. **121**, 043601 (2018). https://link.aps.org/doi/10.1103/PhysRevLett.121.043601.

[67] C. Vaneph, A. Morvan, G. Aiello, M. Féchant, M. Aprili, J. Gabelli, and J. Estève. 'Observation of the Unconventional Photon Blockade in the Microwave Domain'. Phys. Rev. Lett. **121**, 043602 (2018). https://link.aps.org/doi/10.1103/PhysRevLett.121.043602.

[68] H. Flayac and V. Savona. 'Unconventional photon blockade'. Phys. Rev. A **96**, 053810 (2017). https://link.aps.org/doi/10.1103/PhysRevA.96.053810.

[69] J. Y. Marzin, J. M. Gérard, A. Izraël, D. Barrier, and G. Bastard. 'Photoluminescence of Single InAs Quantum Dots Obtained by Self-Organized Growth on GaAs'. Phys. Rev. Lett. **73**, 716–719 (1994). https://link.aps.org/doi/10.1103/PhysRevLett.73.716.

[70] L. Goldstein, F. Glas, J. Y. Marzin, M. N. Charasse, and G. Le Roux. 'Growth by molecular beam epitaxy and characterization of InAs/GaAs strained-layer superlattices'. Applied Physics Letters **47**, 10, 1099–1101 (1985). https://doi.org/10.1063/1.96342.

[71] A. P. Alivisatos. 'Semiconductor Clusters, Nanocrystals, and Quantum Dots'. Science **271**, 5251, 933–937 (1996). http://science.sciencemag.org/content/271/5251/933.

[72] M. Bayer, G. Ortner, O. Stern, A. Kuther, A. A. Gorbunov, A. Forchel, P. Hawrylak, S. Fafard, K. Hinzer, T. L. Reinecke, S. N. Walck, J. P. Reithmaier, F. Klopf, and F. Schäfer. 'Fine structure of neutral and charged excitons in self-assembled In(Ga)As/(Al)GaAs quantum dots'. Phys. Rev. B **65**, 195315 (2002). https://link.aps.org/doi/10.1103/PhysRevB.65.195315.

[73] K. Peng, S. Wu, J. Tang, F. Song, C. Qian, S. Sun, S. Xiao, M. Wang, H. Ali, D. A. Williams, and X. Xu. 'Probing the Dark-Exciton States of a Single Quantum Dot Using Photocurrent Spectroscopy in a Magnetic Field'. Phys. Rev. Applied **8**, 064018 (2017). https://link.aps.org/doi/10.1103/PhysRevApplied.8.064018.

[74] A. Kuther, M. Bayer, A. Forchel, A. Gorbunov, V. B. Timofeev, F. Schäfer, and J. P. Reithmaier. 'Zeeman splitting of excitons and biexcitons in single $In_{0.60}Ga_{0.40}As/GaAs$ self-assembled quantum dots'. Phys. Rev. B **58**, R7508–R7511 (1998). https://link.aps.org/doi/10.1103/PhysRevB.58.R7508.

[75] Y. Toda, S. Shinomori, K. Suzuki, and Y. Arakawa. 'Near-field magneto-optical spectroscopy of single self-assembled InAs quantum dots'. Applied Physics Letters **73**, 4, 517–519 (1998). https://doi.org/10.1063/1.121919.

[76] D. Pinotsi, P. Fallahi, J. Miguel-Sanchez, and A. Imamoglu. 'Resonant Spectroscopy on Charge Tunable Quantum Dots in Photonic Crystal Structures'. IEEE Journal of Quantum Electronics **47**, 11, 1371–1374 (2011).

[77] M. C. Löbl, I. Söllner, A. Javadi, T. Pregnolato, R. Schott, L. Midolo, A. V. Kuhlmann, S. Stobbe, A. D. Wieck, P. Lodahl, A. Ludwig, and R. J. Warburton. 'Narrow optical linewidths and spin pumping on charge-tunable close-to-surface self-assembled quantum dots in an ultrathin diode'. Phys. Rev. B **96**, 165440 (2017). https://link.aps.org/doi/10.1103/PhysRevB.96.165440.

[78] I. E. Itskevich, S. I. Rybchenko, I. I. Tartakovskii, S. T. Stoddart, A. Levin, P. C. Main, L. Eaves, M. Henini, and S. Parnell. 'Stark shift in electroluminescence of individual InAs quantum dots'. Applied Physics Letters **76**, 26, 3932–3934 (2000). https://doi.org/10.1063/1.126825.

[79] F. Pagliano, Y. Cho, T. Xia, F. van Otten, R. Johne, and A. Fiore. 'Dynamically controlling the emission of single excitons in photonic crystal cavities'. Nature Communications **5**, 5786 (2014). https://doi.org/10.1038/ncomms6786.

[80] A. Laucht, F. Hofbauer, N. Hauke, J. Angele, S. Stobbe, M. Kaniber, G. Böhm, P. Lodahl, M.-C. Amann, and J. J. Finley. 'Electrical control of spontaneous emission and strong coupling for a single quantum dot'. New Journal of Physics **11**, 2, 023034 (2009). https://doi.org/10.1088%2F1367-2630%2F11%2F2%2F023034.

[81] A. J. Bennett, R. B. Patel, J. Skiba-Szymanska, C. A. Nicoll, I. Farrer, D. A. Ritchie, and A. J. Shields. 'Giant Stark effect in the emission of single semi-conductor quantum dots'. Applied Physics Letters **97**, 3, 031104 (2010). https://doi.org/10.1063/1.3460912.

[82] C. Kammerer, G. Cassabois, C. Voisin, M. Perrin, C. Delalande, P. Roussignol, and J. M. Gérard. 'Interferometric correlation spectroscopy in single quantum dots'. Applied Physics Letters **81**, 15, 2737–2739 (2002). https://doi.org/10.1063/1.1510158.

[83] E. A. Muljarov and R. Zimmermann. 'Dephasing in Quantum Dots: Quadratic Coupling to Acoustic Phonons'. Phys. Rev. Lett. **93**, 237401 (2004). https://link.aps.org/doi/10.1103/PhysRevLett.93.237401.

[84] A. J. Ramsay, A. V. Gopal, E. M. Gauger, A. Nazir, B. W. Lovett, A. M. Fox, and M. S. Skolnick. 'Damping of Exciton Rabi Rotations by Acoustic Phonons in Optically Excited InGaAs/GaAs Quantum Dots'. Phys. Rev. Lett. **104**, 017402 (2010). https://link.aps.org/doi/10.1103/PhysRevLett.104.017402.

[85] A. J. Ramsay, T. M. Godden, S. J. Boyle, E. M. Gauger, A. Nazir, B. W. Lovett, A. M. Fox, and M. S. Skolnick. 'Phonon-Induced Rabi-Frequency Renormalization of Optically Driven Single InGaAs/GaAs Quantum Dots'. Phys. Rev. Lett. **105**, 177402 (2010). https://link.aps.org/doi/10.1103/PhysRevLett.105.177402.

[86] M. N. Makhonin, J. E. Dixon, R. J. Coles, B. Royall, I. J. Luxmoore, E. Clarke, M. Hugues, M. S. Skolnick, and A. M. Fox. 'Waveguide Coupled Resonance

Fluorescence from On-Chip Quantum Emitter'. Nano Letters **14**, 12, 6997–7002 (2014). https://doi.org/10.1021/nl5032937.

[87] I. Favero, A. Berthelot, G. Cassabois, C. Voisin, C. Delalande, P. Roussignol, R. Ferreira, and J. M. Gérard. 'Temperature dependence of the zero-phonon linewidth in quantum dots: An effect of the fluctuating environment'. Phys. Rev. B **75**, 073308 (2007). https://link.aps.org/doi/10.1103/PhysRevB.75.073308.

[88] A. Berthelot, I. Favero, G. Cassabois, C. Voisin, C. Delalande, P. Roussignol, R. Ferreira, and J. M. Gérard. 'Unconventional motional narrowing in the optical spectrum of a semiconductor quantum dot'. Nature Physics **2**, 759 (2006). https://doi.org/10.1038/nphys433.

[89] H. S. Nguyen, G. Sallen, C. Voisin, P. Roussignol, C. Diederichs, and G. Cassabois. 'Ultra-coherent single photon source'. Applied Physics Letters **99**, 26, 261904 (2011). https://doi.org/10.1063/1.3672034.

[90] A. Schwagmann, S. Kalliakos, I. Farrer, J. P. Griffiths, G. A. C. Jones, D. A. Ritchie, and A. J. Shields. 'On-chip single photon emission from an integrated semiconductor quantum dot into a photonic crystal waveguide'. Applied Physics Letters **99**, 26, 261108 (2011). https://doi.org/10.1063/1.3672214.

[91] S. Kalliakos, Y. Brody, A. Schwagmann, A. J. Bennett, M. B. Ward, D. J. P. Ellis, J. Skiba-Szymanska, I. Farrer, J. P. Griffiths, G. A. C. Jones, D. A. Ritchie, and A. J. Shields. 'In-plane emission of indistinguishable photons generated by an integrated quantum emitter'. Applied Physics Letters **104**, 22, 221109 (2014). https://doi.org/10.1063/1.4881887.

[92] D. Pinotsi, J. M. Sanchez, P. Fallahi, A. Badolato, and A. Imamoglu. 'Charge controlled self-assembled quantum dots coupled to photonic crystal nanocavities'. Photonics and Nanostructures - Fundamentals and Applications **10**, 3, 256 – 262 (2012). http://www.sciencedirect.com/science/article/pii/S1569441011000460.

141

[93] N. Prtljaga, C. Bentham, J. O'Hara, B. Royall, E. Clarke, L. R. Wilson, M. S. Skolnick, and A. M. Fox. 'On-chip interference of single photons from an embedded quantum dot and an external laser'. Applied Physics Letters **108**, 25, 251101 (2016). https://doi.org/10.1063/1.4954220.

[94] N. Prtljaga, R. J. Coles, J. O'Hara, B. Royall, E. Clarke, A. M. Fox, and M. S. Skolnick. 'Monolithic integration of a quantum emitter with a compact on-chip beam-splitter'. Applied Physics Letters **104**, 23, 231107 (2014). https://doi.org/10.1063/1.4883374.

[95] J. Wang, A. Santamato, P. Jiang, D. Bonneau, E. Engin, J. W. Silverstone, M. Lermer, J. Beetz, M. Kamp, S. Höfling, M. G. Tanner, C. M. Natarajan, R. H. Hadfield, S. N. Dorenbos, V. Zwiller, J. L. O'Brien, and M. G. Thompson. 'Gallium arsenide (GaAs) quantum photonic waveguide circuits'. Optics Communications **327**, 49 – 55 (2014). Special Issue on Nonlinear Quantum Photonics, http://www.sciencedirect.com/science/article/pii/S0030401814001874.

[96] L. Midolo, S. L. Hansen, W. Zhang, C. Papon, R. Schott, A. Ludwig, A. D. Wieck, P. Lodahl, and S. Stobbe. 'Electro-optic routing of photons from a single quantum dot in photonic integrated circuits'. Opt. Express **25**, 26, 33514–33526 (2017). http://www.opticsexpress.org/abstract.cfm?URI=oe-25-26-33514.

[97] M. Schwartz, E. Schmidt, U. Rengstl, F. Hornung, S. Hepp, S. L. Portalupi, K. Ilin, M. Jetter, M. Siegel, and P. Michler. 'Fully On-Chip Single-Photon Hanbury-Brown and Twiss Experiment on a Monolithic Semiconductor–Superconductor Platform'. Nano Letters **18**, 11, 6892–6897 (2018). https://doi.org/10.1021/acs.nanolett.8b02794.

[98] S. Kocaman, M. S. Aras, N. C. Panoiu, M. Lu, and C. W. Wong. 'On-chip optical filters with designable characteristics based on an interferometer with embedded silicon photonic structures'. Opt. Lett. **37**, 4, 665–667 (2012). http://ol.osa.org/abstract.cfm?URI=ol-37-4-665.

[99] J. C. Chen, H. A. Haus, , P. R. Villeneuve, and J. D. Joannopoulos. 'Optical filters from photonic band gap air bridges'. Journal of Lightwave Technology **14**, 11, 2575–2580 (1996).

[100] V. S. C. Manga Rao and S. Hughes. 'Single quantum-dot Purcell factor and β factor in a photonic crystal waveguide'. Phys. Rev. B **75**, 205437 (2007). https://link.aps.org/doi/10.1103/PhysRevB.75.205437.

[101] S. Hughes. 'Enhanced single-photon emission from quantum dots in photonic crystal waveguides and nanocavities'. Opt. Lett. **29**, 22, 2659–2661 (2004). http://ol.osa.org/abstract.cfm?URI=ol-29-22-2659.

[102] T. F. Krauss. 'Slow light in photonic crystal waveguides'. Journal of Physics D: Applied Physics **40**, 9, 2666–2670 (2007). https://doi.org/10.1088%2F0022-3727%2F40%2F9%2Fs07.

[103] T. Lund-Hansen, S. Stobbe, B. Julsgaard, H. Thyrrestrup, T. Sünner, M. Kamp, A. Forchel, and P. Lodahl. 'Experimental Realization of Highly Efficient Broadband Coupling of Single Quantum Dots to a Photonic Crystal Waveguide'. Phys. Rev. Lett. **101**, 113903 (2008). https://link.aps.org/doi/10.1103/PhysRevLett.101.113903.

[104] M. Arcari, I. Söllner, A. Javadi, S. Lindskov Hansen, S. Mahmoodian, J. Liu, H. Thyrrestrup, E. H. Lee, J. D. Song, S. Stobbe, and P. Lodahl. 'Near-Unity Coupling Efficiency of a Quantum Emitter to a Photonic Crystal Waveguide'. Phys. Rev. Lett. **113**, 093603 (2014). https://link.aps.org/doi/10.1103/PhysRevLett.113.093603.

[105] A. Faraon, I. Fushman, D. Englund, N. Stoltz, P. Petroff, and J. Vučković. 'Dipole induced transparency in waveguide coupled photonic crystal cavities'. Opt. Express **16**, 16, 12154–12162 (2008). http://www.opticsexpress.org/abstract.cfm?URI=oe-16-16-12154.

[106] X. Zhou, I. Kulkova, T. Lund-Hansen, S. L. Hansen, P. Lodahl, and L. Midolo. 'High-efficiency shallow-etched grating on GaAs membranes for quan-

tum photonic applications'. Applied Physics Letters **113**, 25, 251103 (2018). https://doi.org/10.1063/1.5055622.

[107] R. J. Coles, D. M. Price, J. E. Dixon, B. Royall, E. Clarke, P. Kok, M. S. Skolnick, A. M. Fox, and M. N. Makhonin. 'Chirality of nanophotonic waveguide with embedded quantum emitter for unidirectional spin transfer'. Nature Communications **7**, 11183 (2016). https://doi.org/10.1038/ncomms11183.

[108] P. Androvitsaneas, A. B. Young, C. Schneider, S. Maier, M. Kamp, S. Höfling, S. Knauer, E. Harbord, C. Y. Hu, J. G. Rarity, and R. Oulton. 'Charged quantum dot micropillar system for deterministic light-matter interactions'. Phys. Rev. B **93**, 241409 (2016). https://link.aps.org/doi/10.1103/PhysRevB.93.241409.

[109] P. Androvitsaneas, A. B. Young, J. M. Lennon, C. Schneider, S. Maier, J. J. Hinchliff, G. S. Atkinson, E. Harbord, M. Kamp, S. Höfling, J. G. Rarity, and R. Oulton. 'Efficient Quantum Photonic Phase Shift in a Low Q-Factor Regime'. ACS Photonics **6**, 2, 429–435 (2019). https://doi.org/10.1021/acsphotonics.8b01380.

[110] D. L. Hurst, D. M. Price, C. Bentham, M. N. Makhonin, B. Royall, E. Clarke, P. Kok, L. R. Wilson, M. S. Skolnick, and A. M. Fox. 'Nonreciprocal Transmission and Reflection of a Chirally Coupled Quantum Dot'. Nano Letters **18**, 9, 5475–5481 (2018). https://doi.org/10.1021/acs.nanolett.8b01869.

[111] S. Mahmoodian, K. Prindal-Nielsen, I. Söllner, S. Stobbe, and P. Lodahl. 'Engineering chiral light-matter interaction in photonic crystal waveguides with slow light'. Opt. Mater. Express **7**, 1, 43–51 (2017). http://www.osapublishing.org/ome/abstract.cfm?URI=ome-7-1-43.

[112] B. Lang, R. Oulton, and D. M. Beggs. 'Optimised photonic crystal waveguide for chiral light–matter interactions'. Journal of Optics **19**, 4, 045001 (2017). https://doi.org/10.1088%2F2040-8986%2Faa5f5f.

[113] R. J. Coles, D. M. Price, B. Royall, E. Clarke, M. S. Skolnick, A. M. Fox, and M. N. Makhonin. 'Path-dependent initialization of a single quantum dot exciton spin in a nanophotonic waveguide'. Phys. Rev. B **95**, 121401 (2017). https://link.aps.org/doi/10.1103/PhysRevB.95.121401.

[114] E. M. Purcell, H. C. Torrey, and R. V. Pound. 'Resonance Absorption by Nuclear Magnetic Moments in a Solid'. Phys. Rev. **69**, 37–38 (1946). https://link.aps.org/doi/10.1103/PhysRev.69.37.

[115] D. Englund, D. Fattal, E. Waks, G. Solomon, B. Zhang, T. Nakaoka, Y. Arakawa, Y. Yamamoto, and J. Vučković. 'Controlling the Spontaneous Emission Rate of Single Quantum Dots in a Two-Dimensional Photonic Crystal'. Phys. Rev. Lett. **95**, 013904 (2005). https://link.aps.org/doi/10.1103/PhysRevLett.95.013904.

[116] D. Kleppner. 'Inhibited Spontaneous Emission'. Phys. Rev. Lett. **47**, 233–236 (1981). https://link.aps.org/doi/10.1103/PhysRevLett.47.233.

[117] J.-T. Shen and S. Fan. 'Strongly correlated multiparticle transport in one dimension through a quantum impurity'. Phys. Rev. A **76**, 062709 (2007). https://link.aps.org/doi/10.1103/PhysRevA.76.062709.

[118] L. Banchi, E. Compagno, V. Korepin, and S. Bose. 'Quantum gates between distant qubits via spin-independent scattering'. Quantum **1**, 36 (2017). https://doi.org/10.22331/q-2017-11-30-36.

[119] M. K. Bhaskar, D. D. Sukachev, A. Sipahigil, R. E. Evans, M. J. Burek, C. T. Nguyen, L. J. Rogers, P. Siyushev, M. H. Metsch, H. Park, F. Jelezko, M. Lončar, and M. D. Lukin. 'Quantum Nonlinear Optics with a Germanium-Vacancy Color Center in a Nanoscale Diamond Waveguide'. Phys. Rev. Lett. **118**, 223603 (2017). https://link.aps.org/doi/10.1103/PhysRevLett.118.223603.

[120] S. Xu and S. Fan. 'Fano interference in two-photon transport'. Phys. Rev. A **94**, 043826 (2016). https://link.aps.org/doi/10.1103/PhysRevA.94.043826.

[121] M. F. Limonov, M. V. Rybin, A. N. Poddubny, and Y. S. Kivshar. 'Fano resonances in photonics'. Nature Photonics **11**, 543 (2017). `http://dx.doi.org/10.1038/nphoton.2017.142`.

[122] U. Fano. 'Effects of Configuration Interaction on Intensities and Phase Shifts'. Phys. Rev. **124**, 1866–1878 (1961). `https://link.aps.org/doi/10.1103/PhysRev.124.1866`.

[123] K. A. Fischer, K. Müller, A. Rundquist, T. Sarmiento, A. Y. Piggott, Y. Kelaita, C. Dory, K. G. Lagoudakis, and J. Vučković. 'Self-homodyne measurement of a dynamic Mollow triplet in the solid state'. Nature Photonics **10**, 163 (2016). `https://doi.org/10.1038/nphoton.2015.276`.

[124] M. Kroner, A. O. Govorov, S. Remi, B. Biedermann, S. Seidl, A. Badolato, P. M. Petroff, W. Zhang, R. Barbour, B. D. Gerardot, R. J. Warburton, and K. Karrai. 'The nonlinear Fano effect'. Nature **451**, 1022 (2008). `https://doi.org/10.1038/nature06728`.

[125] I. N. Stranski and L. Krastanow. 'Zur Theorie der orientierten Ausscheidung von Ionenkristallen aufeinander'. Abhandlungen der Mathematisch-Naturwissenschaftlichen Klasse IIb., Akademie der Wissenschaften Wien **146**, 797–810 (1938).

[126] S. Fafard, Z. R. Wasilewski, C. N. Allen, D. Picard, M. Spanner, J. P. McCaffrey, and P. G. Piva. 'Manipulating the energy levels of semiconductor quantum dots'. Phys. Rev. B **59**, 15368–15373 (1999). `https://link.aps.org/doi/10.1103/PhysRevB.59.15368`.

[127] S. Hasegawa. *Reflection High-Energy Electron Diffraction*, 1–14. American Cancer Society (2012). `https://onlinelibrary.wiley.com/doi/abs/10.1002/0471266965.com139`.

[128] S. Franchi, G. Trevisi, L. Seravalli, and P. Frigeri. 'Quantum dot nanostructures and molecular beam epitaxy'. Progress in Crystal Growth and Characteriza-

tion of Materials **47**, 2, 166 – 195 (2003). `http://www.sciencedirect.com/science/article/pii/S0960897405000021`.

[129] Z. Wasilewski, S. Fafard, and J. McCaffrey. 'Size and shape engineering of vertically stacked self-assembled quantum dots'. Journal of Crystal Growth **201-202**, 1131 – 1135 (1999). `http://www.sciencedirect.com/science/article/pii/S0022024898015395`.

[130] H. Sasakura, S. Kayamori, S. Adachi, and S. Muto. 'Effect of indium-flush method on the control of photoluminescence energy of highly uniform self-assembled InAs quantum dots by slow molecular beam epitaxy growth'. Journal of Applied Physics **102**, 1, 013515 (2007). `https://doi.org/10.1063/1.2752598`.

[131] L. S. Inc. 'Lumerical FDTD Solutions' (2019). `http://www.lumerical.com/tcad-products/fdtd/`.

[132] E. Dekel, D. Gershoni, E. Ehrenfreund, D. Spektor, J. M. Garcia, and P. M. Petroff. 'Multiexciton Spectroscopy of a Single Self-Assembled Quantum Dot'. Phys. Rev. Lett. **80**, 4991–4994 (1998). `https://link.aps.org/doi/10.1103/PhysRevLett.80.4991`.

[133] H. S. Nguyen, G. Sallen, C. Voisin, P. Roussignol, C. Diederichs, and G. Cassabois. 'Optically Gated Resonant Emission of Single Quantum Dots'. Phys. Rev. Lett. **108**, 057401 (2012). `https://link.aps.org/doi/10.1103/PhysRevLett.108.057401`.

[134] S. Quantum. 'Single Quantum Eos datasheet' (2019). `https://singlequantum.com/products/single-quantum-eos/`.

[135] B. . H. GmbH. 'The bh TCSPC Handbook' (2019). `http://bio4.fizyka.amu.edu.pl/Soft/SPC-handbook-4ed-30a.pdf`.

[136] T. Heindel, A. Thoma, M. von Helversen, M. Schmidt, A. Schlehahn, M. Gschrey, P. Schnauber, J.-H. Schulze, A. Strittmatter, J. Beyer, S. Rodt,

A. Carmele, A. Knorr, and S. Reitzenstein. 'A bright triggered twin-photon source in the solid state'. Nature Communications **8**, 14870 (2017). `http://dx.doi.org/10.1038/ncomms14870`.

[137] R. J. Young, R. M. Stevenson, P. Atkinson, K. Cooper, D. A. Ritchie, and A. J. Shields. 'Improved fidelity of triggered entangled photons from single quantum dots'. New Journal of Physics **8**, 2, 29 (2006). `http://stacks.iop.org/1367-2630/8/i=2/a=029`.

[138] M. Reindl, K. D. Jöns, D. Huber, C. Schimpf, Y. Huo, V. Zwiller, A. Rastelli, and R. Trotta. 'Phonon-Assisted Two-Photon Interference from Remote Quantum Emitters'. Nano Letters **17**, 7, 4090–4095 (2017). `https://doi.org/10.1021/acs.nanolett.7b00777`.

[139] R. B. Patel, A. J. Bennett, I. Farrer, C. A. Nicoll, D. A. Ritchie, and A. J. Shields. 'Two-photon interference of the emission from electrically tunable remote quantum dots'. Nature Photonics **4**, 632 (2010). `https://doi.org/10.1038/nphoton.2010.161`.

[140] R. B. Patel, A. J. Bennett, K. Cooper, P. Atkinson, C. A. Nicoll, D. A. Ritchie, and A. J. Shields. 'Postselective Two-Photon Interference from a Continuous Nonclassical Stream of Photons Emitted by a Quantum Dot'. Phys. Rev. Lett. **100**, 207405 (2008). `https://link.aps.org/doi/10.1103/PhysRevLett.100.207405`.

[141] Y. Cao, A. J. Bennett, D. J. P. Ellis, I. Farrer, D. A. Ritchie, and A. J. Shields. 'Ultrafast electrical control of a resonantly driven single photon source'. Applied Physics Letters **105**, 5, 051112 (2014). `https://doi.org/10.1063/1.4892013`.

[142] C. L. Salter, R. M. Stevenson, I. Farrer, C. A. Nicoll, D. A. Ritchie, and A. J. Shields. 'An entangled-light-emitting diode'. Nature **465**, 594 (2010). `https://doi.org/10.1038/nature09078`.

[143] R. M. Stevenson, C. L. Salter, J. Nilsson, A. J. Bennett, M. B. Ward, I. Farrer, D. A. Ritchie, and A. J. Shields. 'Indistinguishable Entangled Photons

Generated by a Light-Emitting Diode'. Phys. Rev. Lett. **108**, 040503 (2012). https://link.aps.org/doi/10.1103/PhysRevLett.108.040503.

[144] C. Varnava, R. M. Stevenson, J. Nilsson, J. Skiba-Szymanska, B. Dzurňák, M. Lucamarini, R. V. Penty, I. Farrer, D. A. Ritchie, and A. J. Shields. 'An entangled-LED-driven quantum relay over 1km'. Npj Quantum Information **2**, 16006 (2016). https://doi.org/10.1038/npjqi.2016.6.

[145] M. J. Conterio, N. Sköld, D. J. P. Ellis, I. Farrer, D. A. Ritchie, and A. J. Shields. 'A quantum dot single photon source driven by resonant electrical injection'. Applied Physics Letters **103**, 16, 162108 (2013). https://doi.org/10.1063/1.4825208.

[146] P. Tighineanu, C. L. Dreeßen, C. Flindt, P. Lodahl, and A. S. Sørensen. 'Phonon Decoherence of Quantum Dots in Photonic Structures: Broadening of the Zero-Phonon Line and the Role of Dimensionality'. Phys. Rev. Lett. **120**, 257401 (2018). https://link.aps.org/doi/10.1103/PhysRevLett.120.257401.

[147] S. Kalliakos, Y. Brody, A. J. Bennett, D. J. P. Ellis, J. Skiba-Szymanska, I. Farrer, J. P. Griffiths, D. A. Ritchie, and A. J. Shields. 'Enhanced indistinguishability of in-plane single photons by resonance fluorescence on an integrated quantum dot'. Applied Physics Letters **109**, 15, 151112 (2016). https://doi.org/10.1063/1.4964888.

[148] J. P. Lee, E. Murray, A. J. Bennett, D. J. P. Ellis, C. Dangel, I. Farrer, P. Spencer, D. A. Ritchie, and A. J. Shields. 'Electrically driven and electrically tunable quantum light sources'. Applied Physics Letters **110**, 7, 071102 (2017). https://doi.org/10.1063/1.4976197.

[149] S. Kreinberg, T. Grbešić, M. Strauß, A. Carmele, M. Emmerling, C. Schneider, S. Höfling, X. Porte, and S. Reitzenstein. 'Quantum-optical spectroscopy of a two-level system using an electrically driven micropillar laser as a resonant excitation source'. Light: Science and Applications **7**, 31 (2018). https://www.nature.com/articles/s41377-018-0045-6.

[150] C. K. Hong, Z. Y. Ou, and L. Mandel. 'Measurement of subpicosecond time intervals between two photons by interference'. Phys. Rev. Lett. **59**, 2044–2046 (1987). https://link.aps.org/doi/10.1103/PhysRevLett.59.2044.

[151] H. Thyrrestrup, G. Kiršanskė, H. Le Jeannic, T. Pregnolato, L. Zhai, L. Raahauge, L. Midolo, N. Rotenberg, A. Javadi, R. Schott, A. D. Wieck, A. Ludwig, M. C. Löbl, I. Söllner, R. J. Warburton, and P. Lodahl. 'Quantum Optics with Near-Lifetime-Limited Quantum-Dot Transitions in a Nanophotonic Waveguide'. Nano Letters **18**, 3, 1801–1806 (2018). https://doi.org/10.1021/acs.nanolett.7b05016.

[152] A. Sipahigil, R. E. Evans, D. D. Sukachev, M. J. Burek, J. Borregaard, M. K. Bhaskar, C. T. Nguyen, J. L. Pacheco, H. A. Atikian, C. Meuwly, R. M. Camacho, F. Jelezko, E. Bielejec, H. Park, M. Lončar, and M. D. Lukin. 'An integrated diamond nanophotonics platform for quantum-optical networks'. Science **354**, 6314, 847–850 (2016). http://science.sciencemag.org/content/354/6314/847.

[153] D. E. Chang, V. Gritsev, G. Morigi, V. Vuletić, M. D. Lukin, and E. A. Demler. 'Crystallization of strongly interacting photons in a nonlinear optical fibre'. Nature Physics **4**, 884 (2008). https://doi.org/10.1038/nphys1074.

[154] A. Högele, S. Seidl, M. Kroner, K. Karrai, R. J. Warburton, B. D. Gerardot, and P. M. Petroff. 'Voltage-Controlled Optics of a Quantum Dot'. Phys. Rev. Lett. **93**, 217401 (2004). https://link.aps.org/doi/10.1103/PhysRevLett.93.217401.

[155] J. H. Prechtel, A. V. Kuhlmann, J. Houel, L. Greuter, A. Ludwig, D. Reuter, A. D. Wieck, and R. J. Warburton. 'Frequency-Stabilized Source of Single Photons from a Solid-State Qubit'. Phys. Rev. X **3**, 041006 (2013). https://link.aps.org/doi/10.1103/PhysRevX.3.041006.

[156] J. P. Hugonin, P. Lalanne, T. P. White, and T. F. Krauss. 'Coupling into slow-mode photonic crystal waveguides'. Opt. Lett. **32**, 18, 2638–2640 (2007). http://ol.osa.org/abstract.cfm?URI=ol-32-18-2638.

[157] Y. A. Vlasov and S. J. McNab. 'Coupling into the slow light mode in slab-type photonic crystal waveguides'. Opt. Lett. **31**, 1, 50–52 (2006). `http://ol.osa.org/abstract.cfm?URI=ol-31-1-50`.

[158] H. S. Nguyen, G. Sallen, M. Abbarchi, R. Ferreira, C. Voisin, P. Roussignol, G. Cassabois, and C. Diederichs. 'Photoneutralization and slow capture of carriers in quantum dots probed by resonant excitation spectroscopy'. Phys. Rev. B **87**, 115305 (2013). `https://link.aps.org/doi/10.1103/PhysRevB.87.115305`.

[159] A. Reigue, A. Lemaître, C. Gomez Carbonell, C. Ulysse, K. Merghem, S. Guilet, R. Hostein, and V. Voliotis. 'Resonance fluorescence revival in a voltage-controlled semiconductor quantum dot'. Applied Physics Letters **112**, 7, 073103 (2018). `https://doi.org/10.1063/1.5010757`.

[160] R. J. Warburton. 'Single spins in self-assembled quantum dots'. Nature Materials **12**, 483 (2013). `https://doi.org/10.1038/nmat3585`.

[161] M. Gschrey, R. Schmidt, J.-H. Schulze, A. Strittmatter, S. Rodt, and S. Reitzenstein. 'Resolution and alignment accuracy of low-temperature in situ electron beam lithography for nanophotonic device fabrication'. Journal of Vacuum Science & Technology B **33**, 2, 021603 (2015). `https://doi.org/10.1116/1.4914914`.

[162] J. Liu, M. I. Davanço, L. Sapienza, K. Konthasinghe, J. V. De Miranda Cardoso, J. D. Song, A. Badolato, and K. Srinivasan. 'Cryogenic photoluminescence imaging system for nanoscale positioning of single quantum emitters'. Review of Scientific Instruments **88**, 2, 023116 (2017). `https://doi.org/10.1063/1.4976578`.

[163] T. Kojima, K. Kojima, T. Asano, and S. Noda. 'Accurate alignment of a photonic crystal nanocavity with an embedded quantum dot based on optical microscopic photoluminescence imaging'. Applied Physics Letters **102**, 1, 011110 (2013). `https://doi.org/10.1063/1.4773882`.

[164] K. H. Lee, A. M. Green, R. A. Taylor, D. N. Sharp, J. Scrimgeour, O. M. Roche, J. H. Na, A. F. Jarjour, A. J. Turberfield, F. S. F. Brossard, D. A. Williams, and G. A. D. Briggs. 'Registration of single quantum dots using cryogenic laser photolithography'. Applied Physics Letters **88**, 19, 193106 (2006). `https://doi.org/10.1063/1.2202193`.

[165] D. Hallett, A. P. Foster, D. L. Hurst, B. Royall, P. Kok, E. Clarke, I. E. Itskevich, A. M. Fox, M. S. Skolnick, and L. R. Wilson. 'Electrical control of nonlinear quantum optics in a nano-photonic waveguide'. Optica **5**, 5, 644–650 (2018). `http://www.osapublishing.org/optica/abstract.cfm?URI=optica-5-5-644`.

[166] A. Ridolfo, O. Di Stefano, N. Fina, R. Saija, and S. Savasta. 'Quantum Plasmonics with Quantum Dot-Metal Nanoparticle Molecules: Influence of the Fano Effect on Photon Statistics'. Phys. Rev. Lett. **105**, 263601 (2010). `https://link.aps.org/doi/10.1103/PhysRevLett.105.263601`.

[167] J.-T. Shen and S. Fan. 'Coherent Single Photon Transport in a One-Dimensional Waveguide Coupled with Superconducting Quantum Bits'. Phys. Rev. Lett. **95**, 213001 (2005). `https://link.aps.org/doi/10.1103/PhysRevLett.95.213001`.

[168] A. P. Foster, D. Hallett, I. V. Iorsh, S. J. Sheldon, M. R. Godsland, B. Royall, E. Clarke, I. A. Shelykh, A. M. Fox, M. S. Skolnick, I. E. Itskevich, and L. R. Wilson. 'Tunable Photon Statistics Exploiting the Fano Effect in a Waveguide'. Phys. Rev. Lett. **122**, 173603 (2019). `https://link.aps.org/doi/10.1103/PhysRevLett.122.173603`.

[169] J.-H. Kim, S. Aghaeimeibodi, C. J. K. Richardson, R. P. Leavitt, and E. Waks. 'Super-Radiant Emission from Quantum Dots in a Nanophotonic Waveguide'. Nano Letters **18**, 8, 4734–4740 (2018). PMID: 29966093, `https://doi.org/10.1021/acs.nanolett.8b01133`.

[170] J. S. Foresi, P. R. Villeneuve, J. Ferrera, E. R. Thoen, G. Steinmeyer, S. Fan, J. D. Joannopoulos, L. C. Kimerling, H. I. Smith, and E. P. Ippen. 'Photonic-

bandgap microcavities in optical waveguides'. Nature **390**, 143–145 (1997). https://doi.org/10.1038/36514.

[171] B.-S. Song, S. Noda, T. Asano, and Y. Akahane. 'Ultra-high-Q photonic double-heterostructure nanocavity'. Nature Materials **4**, 207–210 (2005). https://doi.org/10.1038/36514.

[172] D. O'Brien, M. Settle, T. Karle, A. Michaeli, M. Salib, and T. Krauss. 'Coupled photonic crystal heterostructure nanocavities'. Opt. Express **15**, 3, 1228–1233 (2007). http://www.opticsexpress.org/abstract.cfm?URI=oe-15-3-1228.

[173] Q. Quan, P. B. Deotare, and M. Loncar. 'Photonic crystal nanobeam cavity strongly coupled to the feeding waveguide'. Applied Physics Letters **96**, 20, 203102 (2010). https://doi.org/10.1063/1.3429125.

[174] Q. Quan and M. Loncar. 'Deterministic design of wavelength scale, ultra-high Q photonic crystal nanobeam cavities'. Opt. Express **19**, 19, 18529–18542 (2011). http://www.opticsexpress.org/abstract.cfm?URI=oe-19-19-18529.